Numerical and Experimental Investigation of a Novel Waveguide Design for use in High Power Laser Diode Devices.

by

John A. Patchell

A thesis submitted for the degree of
Doctor of Philosophy
in the University of Dublin

Department of Pure and Applied Physics
Trinity College Dublin
University of Dublin

October 2001

Declaration

This thesis has not been submitted as an exercise for a degree in this or any other university. The work described in this thesis is entirely my own, with exception of assistance recognised in the acknowledgements and the collaborative work noted in the publications. I agree that Trinity College may lend or copy this thesis on request.

John Anthony Patchell 

Numerical and Experimental Investigation of a Novel Waveguide Design for use in High Power Laser Diode Devices

By *John A. Patchell* *October 2001*

Summary

Because of their efficiency, small size and reliability high power laser diodes are used for numerous tasks, such as the pumping of solid state lasers, second harmonic generation and the pumping of rare earth fibre amplifiers. The next generation of optical networks will most likely use Raman amplifiers for optical regeneration instead of Erbium doped fibre amplifiers. Up to now the widespread use of Raman has been limited by the availability high power pump modules.

In this thesis we examine a new type of waveguide design for use in high power laser diodes, a unique feature of this design is that the last mode before cut-off is predominantly confined to the low index region of the waveguide structure. As this is quite a counter intuitive result, structures based on this design concept, are for shorthand purposes referred to as Lo-guides. The subject matter in this thesis is concerned with the investigation of waveguide structures which could potentially facilitate the production of higher power single spatial mode laser diodes.

Chapters 3 and 4 are primarily concerned with validating the Lo-guide concept. This involved implementing designs based on this concept in both optically and electrically pumped laser structures. Quantum well active regions were positioned in these structures so as to achieve single spatial mode operation. A number of standard measurements were then preformed on these structures to ensure they were indeed lasing. The main result of this exercise, was the observation of lasing in the predicted highest order modes of these structures.

Chapters 5 and 6 consider the implementation of the Lo-guide design concept in the lateral direction as originally envisaged. A dedicated beam propagation model was written to calculate the lateral mode profiles in these devices. The results of measurements on the devices fabricated to specifications obtained from the numerical simulations are then presented. Overall the results presented obtained demonstrated good agreement with those generated by the beam propagation model. One of the more interesting results of this analysis was the fact that the emission patterns from these devices was shown to be dependent on the bias current applied. In conclusion working prototype structures based on the Lo-guide concept have been demonstrated, however much work remains to be done in order to perfect the operation of these devices.

Acknowledgements.

During my time in the opto-electronics group in TCD, I have received friendship, support and encouragement from all whom I've worked with. I would like this opportunity to say, thanks!

First of all I would like to say thank you to my supervisor, Professor John Hegarty for accepting me into his group. Thus providing me resources and equipment which allowed this thesis to be completed. I would also like to thank Dr. James O'Gorman for giving initial direction to my work, and for was always being willing to share his vast knowledge of semiconductor physics. To Fred Logue for his guidance and supervision during my first year in lab, without who's assistance I might not be "writing up" quite yet. Thanks are also due to Dr. John Donegan for proof reading this thesis.

Also due acknowledgement, are the staff of the MNRC in Cork and at the University of Sheffield, in particular Brian Corbett and John Roberts, who provided the samples investigated in this thesis.

That this point, I would like to thank the members of the opto-electronics group both past and present. The transition from graduate to post-graduate student was a painless one thanks to the friendship shown to me by those in this group, namely Adrian, Brendan, Christophe, DTF, Dave McDonald, Declan, Fergal, Louise, Mick, Pascal, Shane, Tara. A special thanks to my contemporaries, Alan Cian and Andrea who provided encouragement, support and a will to continue. Everyone else who provided a helping hand, Richard, Karl, Gary, Paddy, Eamonn. Finally to Canice who's sense of humour made the last year underground bearable.

Thanks also to the technical staff of the Physics Department, Tom Bruke, John Kelly and David Grouse.

I would also like to thank those people closest to me for their support and kindness. Especially to Eimear for listening to my endless complainants about life, academic and otherwise. Finally I would like to thank my family, for their love and support. I owe them a debt of gratitude.

Publications.

J. A. Patchell, F.P. Logue, J. O'Gorman, J. Hegarty, B. A. Usievich and V. A. Sychugov. Demonstration of high-brightness-mode propagation in a compound waveguide structure. *Appl. Phys. Lett.*, 75(2): 169-171, July 1999.

F.P. Logue, J.A. Patchell, J. O'Gorman, V.A. Sychugov, B. A. Usievich, J. Hegarty. Novel wave-guide design for high brightness optoelectronic applications. *Optical and Quantum Electronics*, 2000, vol. 32, no. 10, pp. 1175

F.P. Logue, J.A. Patchell, J. O'Gorman, V.A. Sychugov, B. A. Usievich, J. Hegarty. Transverse waveguide design for high-brightness laser diodes. *Proc. SPIE* Vol 3944 pp 387-393. 2001.

Table of Contents

Chapter 1

Introduction

1.1 General Introduction and Background.

At present, almost all long distance data transfer occurs over optical networks. Such networks would not be possible without the ability to efficiently generate light with very well defined characteristics and transmit it effectively over long distances. The first optical networks consisted of just three photonic components, laser diodes to transmit the data, optical fibres to transport the signals and photodiodes to receive the data. As the losses in optical fibres were gradually reduced it became possible to send information over longer and longer distances. However despite all the advances to date in laser diode and optical fibre design, the transmission of optical signals across intercontinental distances still requires the use of optical amplifiers. At present the most common optical amplifier in use in optical networks is the Erbium Doped Fibre Amplifier (EDFA). Although in the next generation of optical networks Raman amplifiers may prove more useful, since they provide optical amplification over a larger spectral range than EDFAs and gain amplification is distributed over the length of the fibre. According to a report by "Canadian Imperial Bank of Commerce World Markets Inc.", the market for Raman amplifiers is predicted to increase from 3.3million in 1999 to 750million in 2004. Up until recently the widespread use of these amplifiers has been limited by the availability of suitable high power pump lasers [1]. The advent of Dense Wavelength Division Multiplexing (DWDM), in which several single longitudinal mode lasers with closely spaced wavelengths transmit data over a single fibre, has opened up a number of interesting possibilities for optical networking, such as all optical switching. The introduction of such technologies will require improvements to existing waveguiding devices and the invention of new ones. Furthermore, future optical networks will require far more

optical amplifiers, in order to overcome the losses associated with multiplexing, demultiplexing and optical switching functions. The physical layer of an optical network, can essentially be thought of as consisting of a number of active and passive components almost all of which incorporate some type of waveguide. The waveguiding components in these networks can usually be classed as either planar waveguides, which are incorporated into semiconductor laser diodes; ridge waveguide structures, which are used in photonic integrated circuits; or circular waveguide structures such as optical fibres. In order to minimize the number of amplifiers in an optical network it is essential to maximize the coupling efficiency between these components. The subject matter of this thesis deals with a novel waveguide design for a semiconductor laser, which has the potential to deliver increased single spatial mode power emission from laser diode devices, hence allowing more powerful and efficient optical amplifiers. The details of this waveguide concept will be presented in Section 2.10. The following section introduces EDFA and Raman amplifiers, and discusses the need for laser diode devices with greater single mode output power. Finally the structure of this thesis is outlined.

1.2 Raman and Erbium Doped Fibre Amplifiers.

As mentioned previously, it is still not possible to transmit optical signals over inter-continental distances without regenerating the signal at certain points along the way. The most common type of amplifier is the EDFA [2]. The general layout of an EDFA is shown in Figure 1.1.

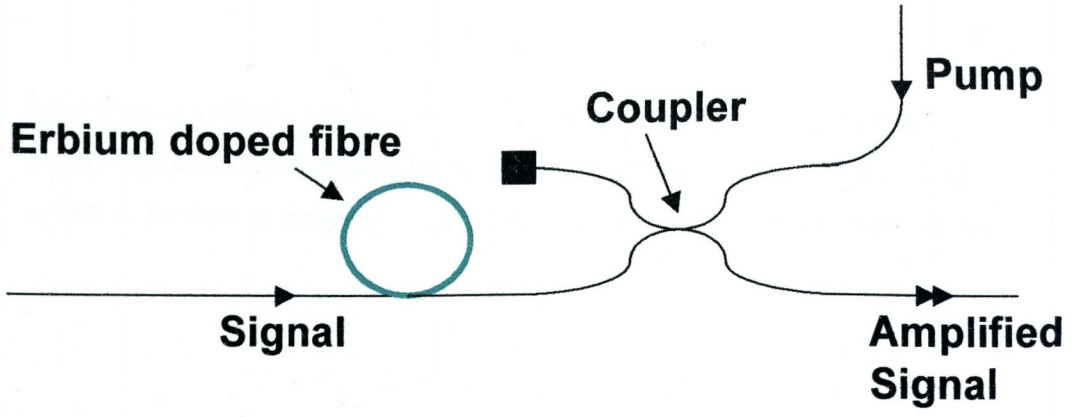

Figure 1-1 Illustration of an Erbium doped fibre Amplifier.

Amplifiers such as these can be pumped by lasers emitting at either 980 or 1480nm [3] (Figure 1.2), and provide gain over a wavelength range of about 40nm that is centred on 1530nm. Once a population inversion is created in the erbium doped fibre, light guided by the fibre that is within this wavelength range will be amplified. Further it is possible to extend the wavelength over which this type of amplifier provides gain by introducing other rare elements into the fibre. Therefore gain in these devices is dependant on a number of factors, the constituent dopants, the respective doping concentrations, the length of fibre used, the pump power level and also the spectral distribution of the pump radiation. While the spectral distribution of the pumping radiation can be controlled through the use of Distributive Feedback Lasers (DFB), the amount of single spatial mode power that can be obtained from a laser diode is limited by factors, which are characteristic of these devices.

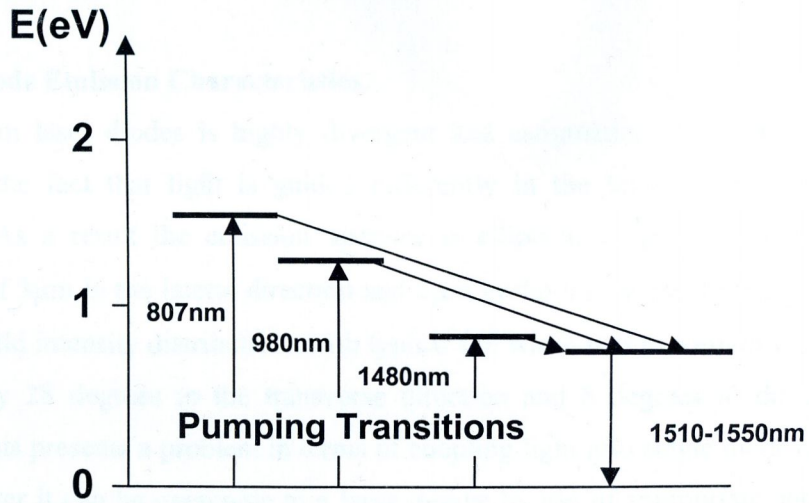

Figure 1-2 Energy levels in an Er^{3+} ion in glass.

Since Raman amplifiers require more power than EDFA's their widespread deployment has until now been limited by the availability of high power pump modules. In short as the power obtainable from single spatial mode laser diodes has

increased so has the feasibility of Raman amplifiers. Figure 1.3 shows a schematic of a Raman amplifier.

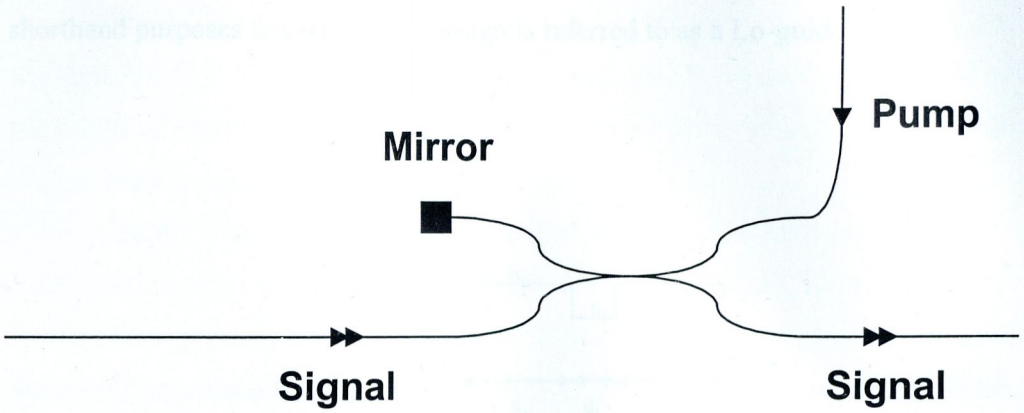

Figure 1-3 Illustration of the layout of a Raman Amplifier.

1.3 Laser Diode Emission Characteristics.

Emission from laser diodes is highly divergent and astigmatic. The astigmatism stems from the fact that light is guided differently in the lateral and transverse directions. As a result the emission aperture is elliptical in shape, with typical dimensions of 3μm in the lateral direction and 1μm in the transverse direction. This leads to farfield intensity distributions with typical full width half maximum values of approximately 28 degrees in the transverse direction and 8 degrees in the lateral direction. This presents a problem in terms of coupling light into single mode optical fibres, however it can be overcome to a large degree by use of appropriate coupling optics. A further problem with laser diodes as regards coupling large amounts of power into optical fibres, is that the power available from these devices is limited by the size of their emission apertures. This limit is set by the catastrophic optical damage (COD) threshold of the laser diode material. Although COD threshold of a device can be increased by facet passivation and the choice of material system [4], there reaches a point where the only way to increase the output from a device is to increase the area of its emitting aperture. Unfortunately as will be explained in Section 2.10 there is a trade off between the size of the emission aperture and beam

stability. In this thesis we present a novel compound waveguide concept, which should offer a new way around this impasse. Counter-intuitively in such structures, the highest order mode is predominantly guided in a region of the waveguide core that has a relatively low refractive index. This concept is illustrated in Figure 1.3. For shorthand purposes this waveguide design is referred to as a Lo-guide.

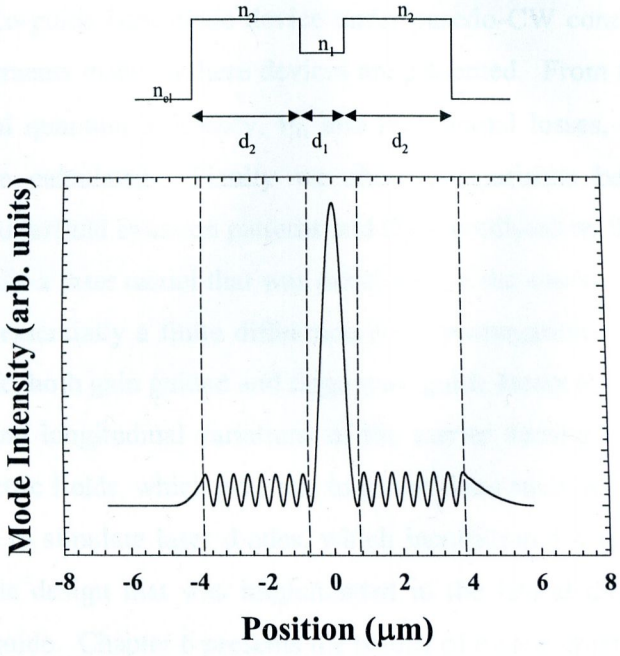

Figure 1-4 Illustration of the refractive index profile of a symmetric Lo-guide structure and the intensity profile of its highest order mode

1.4 Thesis Overview.

Chapter 2 presents much of the basic theory relating to laser diode devices and semiconductor physics, as well as introducing some novel waveguide structures that are based on the Lo-guide concept. The potential advantages of these structures are also detailed here.

In general, Chapters 3 and 4 relate to the incorporation of Lo-guide type structures in the transverse direction, of both optically and electrically pumped semiconductor laser structures. More specifically, Chapter 3 introduces a design

procedure for semiconductor waveguide structures and laser diode devices, this includes a description of a numerical method for calculating the modal solutions of arbitrarily shaped waveguides. The results of some transmission measurements on passive Lo-guide structures are then presented. Details of an optical pumping experiment designed to excite the highest order modes of a Lo-guide type structure implemented in the transverse direction are given. Finally in this chapter we present the results of nearfield measurements that demonstrate the structure is lasing in one its highest order modes.

Chapter 4 is concerned with the electrical and optical characterisation of an electrically pumped Lo-guide laser diode device under pusedo-CW conditions. The results of the measurements made on these devices are presented. From these results values for the internal quantum efficiency, η_i, and the internal losses, α_i, of these novel structures were calculated. Finally we show comparisons between both measured nearfield and farfield emission patterns and those predicted by theory.

Chapter 5 details a laser model that was developed in the course of this work. The model, which is essentially a finite difference beam propagation model, allows the optical fields inside, both gain guided and ridge waveguide lasers to be calculated. It allows for lateral and longitudinal variations of the carrier density as well as for coupling with the electric fields, which give rise to instabilities such as filamentation. This model was used to simulate laser diodes, which incorporated a symmetric Lo-guide ridge waveguide design that was implemented in the lateral direction in the form of a ridge waveguide. Chapter 6 presents the results of measurements made on a Lo-guide device, which was based on the design simulated in Chapter 5. Standard and polarization resolved nearfield measurements reveal this structure to be lasing in its highest order mode. Overall good agreement was obtained between calculation and experiment, however nearfield measurements show that the emission patterns from these devices are dependent on the bias current applied.

1.4 References

1 S. Namiki, and Y. Emori. Ultrabroad Band Raman Amplifiers Pumped and Gain Equalized by Wavelength Division Multiplexed High Power Laser Diodes. *IEEE J. Sel. Quantum Electron.*, QE-7(1): 3-13, January/February 2001

2 John Gowar. *Optical Communications Systems, second edition*. Prentice Hall. Pages 107-113.

3 John Gowar. *Optical Communications Systems, second edition*. Prentice Hall. Page 367.

4 J.K. Wade, L.J. Mawst, D. Botez, M. Jansen, F. Fang, and R.F. Nabiev. High continous wave power, 0.8um-band, Al-free active-region diode lasers. *Appl. Phys. Lett.*, 70(2): 149-151, January 1997.

Chapter 2

Basic Concepts.

2.1 Overview.

This chapter contains the background physics that will be required in the following chapters. The chapter starts by examining the physics of a general laser cavity. Some select experts of semiconductor physics is then introduced. At this point some of the major steps in the evolution of the laser diode are discussed. Then after an introduction to ray and guided wave optics, the Lo-Guide waveguide concept is introduced. Finally we review some existing high laser diode structures.

2.2 A General Laser Cavity.

In its most basic form a laser [1] can be considered as an optical gain medium inside a resonant optical cavity. The gain medium is a material, which under normal conditions absorbs radiation over a particular wavelength range. However by pumping such a material with electrical or optical energy it is possible to create a population inversion of the energy levels or bands associated with a particular transition. Once a population inversion has been achieved radiation traveling through the material will be amplified rather than being absorbed. If this amplification, commonly referred to as gain, is sufficient to overcome the losses associated with the cavity, then lasing action will occur. The pump power necessary to overcome the losses of the laser cavity is termed the *threshold* pump power. What is stated above is true about almost every type of laser system, it is therefore the type of gain medium and cavity configuration used which differentiate the various types of lasers that exist. The purpose of this thesis is to

investigate the properties of a particular type of laser, the semiconductor laser diode, which incorporates a novel waveguide design.

2.3 The Criteria for Lasing Action.

Figure 2.1 shows a schematic of a laser cavity. Optical loss mechanisms of the cavity include, absorption and scattering of radiation within the active medium, and transmission of radiation through the mirrors.

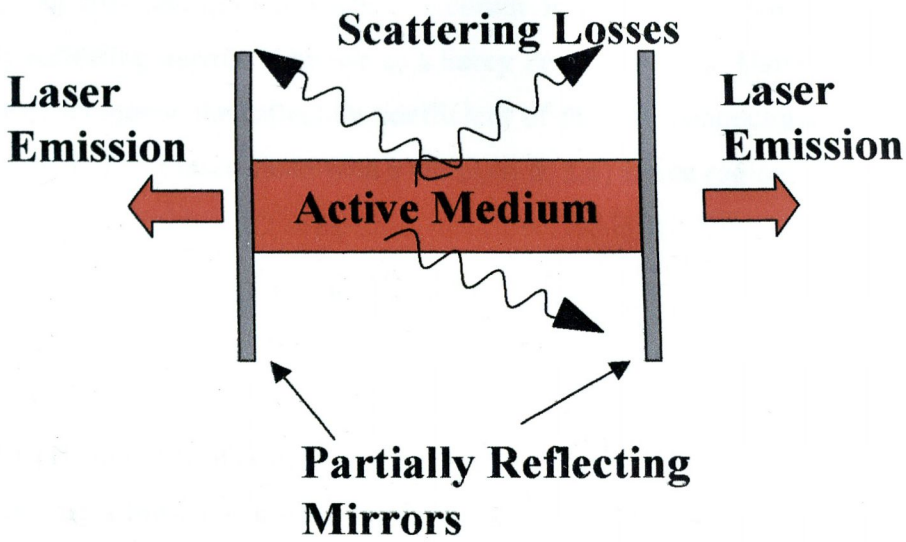

Figure 2-1 An illustraion of a typical laser cavity.

If the optical power passing some point, x in such a cavity is initially $P(x)$, then the power passing the same point after single round trip of cavity is given by

$$P(2l+x) = r_1 r_2 P(x) \exp[(g-\alpha_i)2l] \qquad 2.1$$

where r_1 and r_2 are the mirror reflectivties, L is the cavity length, α_i is the internal losses of the cavity and g is optical gain produced by the active medium. If $P(2l)/P(x) >= 1$, then the optical gain produced by the active medium is sufficient to overcome the losses associated with the cavity and lasing action occurs [2]. Using this as the criteria for lasing, the amount of optical gain necessary to bring the cavity above threshold can be derived, the so called threshold gain as it is referred to is given by Equation 2.2.

$$g_{th} = \alpha_i + \frac{1}{2L}\ln\left(\frac{1}{r_1 r_2}\right). \qquad 2.2$$

2.4 The Fabry-Perot Cavity.

In a laser diode, optical feedback is provided by the cleaved facets of a semiconductor crystal. In this configuration active medium is placed between two planar parallel partially reflecting mirrors is known as a Fabry Perot cavity[3]. Using Fresnel's equation for normal incidence the reflection coefficient of the semiconductor/air interface, r, can be calculated. For a laser diode with a GaAs ($n \cong 3.6$) active region, r is given by:

$$r = \left(\frac{n_2 - n_1}{n_2 + n_1}\right)^2 \cong \left(\frac{3.6-1}{3.6+1}\right)^2 = 0.32. \qquad 2.3$$

It is the large amounts of optical gain per unit length produced by inverted semiconductor materials that allows the mirror losses associated with this type of laser cavity to be overcome. It is also the high gain that allows the realization of laser diodes with very short cavity lengths. In laser diodes as in other laser cavities, standing wave patterns are set up. These standing waves must satisfy the condition:

$$m\frac{\lambda}{2} = L_{opt}, \qquad 2.4$$

where λ is the wavelength of the light in the optical mode and, m, is an integer. L_{opt} is optical path length between the two facets, and is approximately equal to the product of

the length of the cavity, L, and its index of refraction, n. Each value of m that satisfies Equation 2.4, corresponds to an axial or longitudinal mode of the cavity. The spacing between these modes is given by:

$$\Delta\lambda \approx \frac{\lambda^2}{2nL} \qquad 2.5$$

Typical values for the length and refractive index of a GaAs based pump laser diode chip operating at λ=980nm, are L = 1mm and $n \cong 3.6$. Putting these values into the above Equation 2.5 we get:

$$\Delta\lambda \cong \frac{(980\times10^{-9}m)^2}{2(3.4)(1\times10^{-3}m)} = 0.13nm \qquad 2.6$$

In general the wavelength spectrum of a typical Fabry-Perot laser diode will contain a number of longitudinal modes. There are two reasons for this, the wide gain spectrum of semiconductor materials and the poor mode selectivity of the Fabry-Perot cavity.

2.5 Radiative and Non-Radiative Transitions

Figure 2.2, is a schematic representation of some of the various electronic transitions [4] that occur in semiconductor laser materials. The first three processes shown are classed as radiative transitions as they involve a photon of light, while remaining processes are classed as non-radiative. In this diagram the open circles represent unfilled states while the solid circles represent filled states.

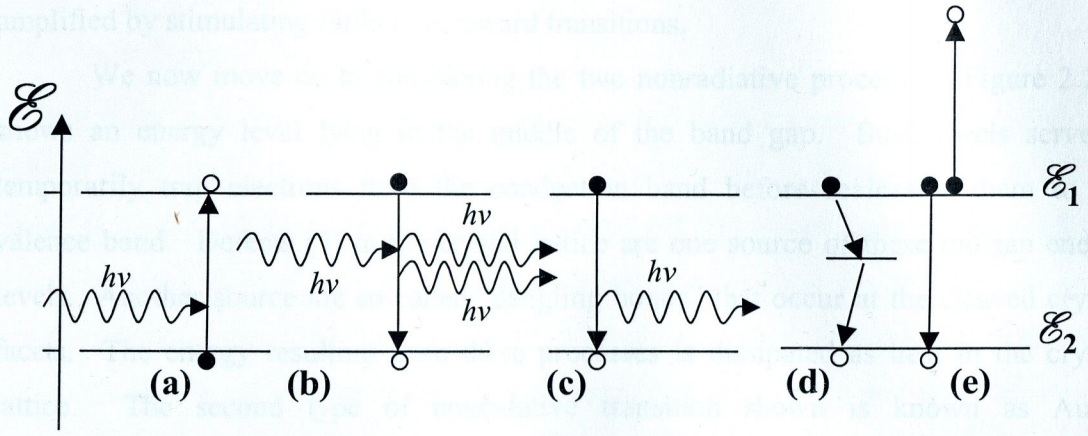

Figure 2-2 Illustration of some of the possible electronic transitions which occur in semiconductor materials (a) Absorption, (b) Stimulated Emission, (c) Spontaneous Emission, (d) Defect recombination and (e) Auger Recombination

The first two processes, absorption and stimulated emission can occur only when the system is stimulated by electromagnetic radiation of the correct frequency. This frequency, υ, is given by the energy separation of the two levels divided by Plank's constant.

$$\upsilon = (\mathscr{E}_2 - \mathscr{E}_1)/h \qquad 2.7$$

Absorption occurs when a photon of radiation stimulates an upward electronic transition. Stimulated emission is the reverse of this process, it occurs when a photon of radiation stimulates a downward electronic transition. This process results in the emission of a photon, which has the same frequency and is in phase with the stimulating radiation. In a laser operating above threshold, feedback from the cavity mirrors ensures that stimulated emission is the dominant process.

Downward transitions can also occur spontaneously in the absence of any electromagnetic radiation, this phenomenon is known as spontaneous emission (Figure 2.2(c)). In fact excited electronic states generally have a mean lifetime, τ, associated with them. This is the average length of time an electron will spend in this state before

relaxing to a lower energy state. In semiconductor lasers spontaneous emission occurs over a large wavelength range, and can be thought of as seed for the laser emission. Cavity modes that lie within the wavelength interval over which there is positive gain are amplified by stimulating further downward transitions.

We now move on to considering the two nonradiative processes. Figure 2.2(d) shows an energy level lying in the middle of the band gap. Such levels serve to temporarily trap electrons from the conduction band before realeasing them to the valence band. Defects [5] in the crystal lattice are one source of these midgap energy levels. Another source are so-called "dangling bonds" that occur at the cleaved crystal facets. The energy resulting from these processes is dissipated as heat in the crystal lattice. The second type of nonradative transition shown is known as Auger recombination. There are several permutations of this process. Figure 2.2(e) depicts the CCCH process [6], which is so-called because it involves three conduction band states and one heavy hole state. In essence what is illustrated here is a collision between two electrons, the result of which is that one electron gets knocked down to the valence band while the other gets excited to a higher energy level in the conduction band. The high energy electron eventually thermalises back down to the bottom of the conduction band, again as in the case of the first nonradative process, energy is released to the crystal lattice in the from of heat. This last process is a significant problem in devices operating at long wavelengths (λ=1.55μm).

2.6 Semiconductor Physics.

As the name implies, semiconductors have electrical resistivities at room temperature intermediate between those of conductors and insulators, with values in the range of 10^{-2} to 10^{9} Ωcm[7]. The properties of this enormously important class of materials is primarily due to their small band gaps, one consequence of this is that unlike in metals the conductivity of semiconductors increases exponentially with increasing temperature. Another consequence of the small band gap energy, is that the addition of small amounts of impurity elements can also significantly alter their conductivities. The ability to alter

the electrically properties of semiconductors in this way, is key to their technological importance.

2.6.1 Semiconductor Band Structure.

At this point it is necessary to categorize semiconductor materials as either direct or indirect band gap materials. This is an important distinction as the active region in laser diode devices must be a direct bandgap material [8]. In direct bandgap materials the lowest conduction band minimum and the highest valence band maximum occur at the same wavevector, **k**, in the Brillouin zone. Whereas in indirect bandgap semiconductors the conduction band minimum and valence band maximum don't occur at the same **k** value. Hence photon emission and absorption require the participation of phonons to conserve momentum. This makes lasing in indirect bandgap material improbable because the lowest energy band to band transition probabilities are much smaller than in direct bandgap materials. This in turn leads to low internal quantum efficiencies, because of the relatively long lifetime of electrons in indirect minima.

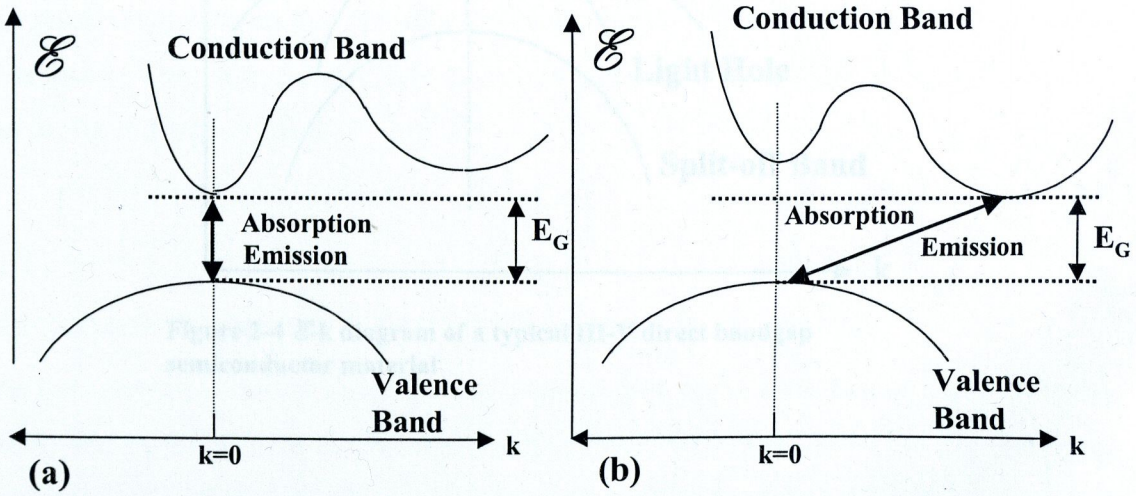

Figure 2-3 Band Structure of (a) direct and (b) indirect bandgap semiconductor materials

Figures 2.3(a) and (b) respectively, show the band structures of typical direct and indirect bandgap materials. Examples of direct bandgap materials include ZnSe, InP and GaAs, whereas indirect bandgap materials include Ge, Si and AlAs. At this point it is worth making a further distinction between Group IV and III-V semiconductor material. Si and Ge are Group IV semiconductors as both of these elements possess four valence band electrons, while GaAs and AlAs are known as III-V semiconductors [9]. Figure 2.4 shows the band structure of a direct bandgap semiconductor in further detail still, this diagram illustrates the conduction and valence bands of a typical direct bandgap III-V semiconductor material.

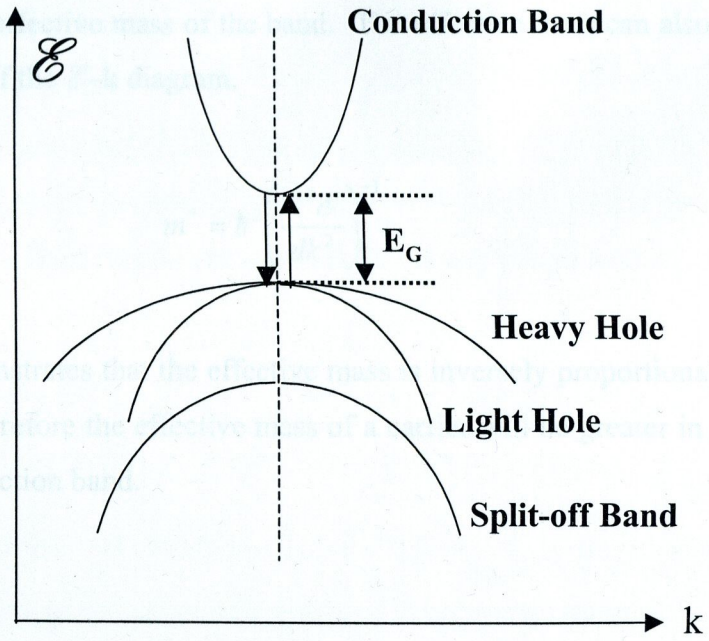

Figure 2-4 $\mathscr{E}$-k diagram of a typical III-V direct bandgap semiconductor material

Here the conduction band and three valence bands, commonly referred to as the, heavy hole, light hole, and split-off band, can be thought of as originating from the discrete atomic energy levels of the isolated atoms that compose the crystal. In this sense, the

conduction band an be thought of as a remnant of an s atomic orbital, while the three valence bands are remnants of the three p atomic orbitals, p_x, p_y, and p_z. The curvature of the conduction band is typically much greater than any of the valence bands.

2.6.2 Effective Mass.

In the vicinity of the band edge, the electronic band structure of a direct bandgap semiconductor can be approximated by a parabolic function.

$$\mathscr{E} = \frac{\hbar^2 k^2}{2m*} \qquad 2.8$$

where m^* is the effective mass of the band. The effective mass can also be expressed in terms curvature of the $\mathscr{E}$–**k** diagram.

$$m^* = \hbar^2 \left(\frac{d^2 \mathscr{E}}{dk^2} \right)^{-1} \qquad 2.9$$

This result demonstrates that the effective mass is inversely proportional to the curvature of the band. Therefore the effective mass of a carrier will be greater in the valence band than in the conduction band.

2.6.3 Quantum Confinement & Density of States function

Advancements in semiconductor growth technologies such as molecular beam epitaxity (MBE) and metal organic chemical deposition (MOCVD), now allow the fabrication of quantum confined structures. As will be discussed later, devices incorporating such structures, demonstrate better performance characteristics over those that don't. In quantum confined structures, electronic states are confined to dimensions comparable to

the de Brogile wavelength, λ_B, of the electron this is defined as $\lambda = h/p$, where p is momentum associated with the electron. The simplest quantum confined structures and by far the easiest to fabricate are known as quantum wells. Other quantum confined structures include, quantum wires and quantum dots, however since these structures are not dealt with in the subject matter of this thesis they will not be discussed any further. Quantum wells typically consist of up to twenty monolayers of narrow bandgap material sandwiched between higher bandgap materials. In a quantum well the electronic states are effectively confined in a two dimensional plane perpendicular to the growth direction. One of the more important implications of the introduction of quantum confinement is the modification in the density of states function. The density of states function of a material describes the distribution of allowed electronic states as a function of energy.

2.6.4 The Density of States Function.

Almost all the properties of crystals can be explained in terms of the nearly free electron model, in this approach electrons are perturbed only weakly by the periodic potential of the crystal lattice. The Schrodinger equation for an electron in such a potential is,

$$-\frac{\hbar^2}{2m^*}\left(\frac{\partial^2}{\partial x^2}+\frac{\partial^2}{\partial y^2}+\frac{\partial^2}{\partial z^2}\right)\Psi_{\mathbf{k}}(\mathbf{r})+U_{\mathbf{k}}(\mathbf{r})\Psi_{\mathbf{k}}(\mathbf{r})=\mathscr{E}_{\mathbf{k}}\Psi_{\mathbf{k}}(\mathbf{r}) \qquad 2.10$$

where, $\Psi_{\mathbf{k}}(\mathbf{r})$, is the wavefunction of the electron, $\mathscr{E}_{\mathbf{k}}$ is the energy of a particular electronic state, and $U_{\mathbf{k}}(\mathbf{r})$ is periodic potential due the crystal lattice.
The Bloch theorem states: [10]

> "The eigenfunctions of the Schrodinger equation for a periodic potential are the product of a plane wave exp(*i***k.r**) times a function $U_{\mathbf{k}}(\mathbf{r})$ with the periodicity of the crystal lattice.",

where **k** is the wavevector of the traveling wave. Now consider if N electrons confined to a crystal of dimensions L_x, L_y and L_z. As a consequence of the Bloch theorem the electronic wavefunctions can be written in the following form.

$$\Psi_{\mathbf{k}}(\mathbf{r}) = U_{\mathbf{k}}(\mathbf{r})\exp(i\mathbf{k}\cdot\mathbf{r}) \qquad 2.11$$

provided that the components of the wavevector **k** satisfy the following relations

$$\begin{aligned} k_x &= 0, \quad \pm\frac{2\pi}{L}, \quad \pm\frac{4\pi}{L}, \ldots\ldots\ldots \\ k_y &= 0, \quad \pm\frac{2\pi}{L}, \quad \pm\frac{4\pi}{L}, \ldots\ldots\ldots \\ k_z &= 0, \quad \pm\frac{2\pi}{L}, \quad \pm\frac{4\pi}{L}, \ldots\ldots\ldots \end{aligned} \qquad 2.12$$

By substituting Equation 2.11 into Equation 2.10, the energies of the allowed k states can be expressed, as a function of the components of the wavevector **k**.

$$\mathscr{E}_{\mathbf{k}} = \frac{\hbar^2}{2m^*}|\mathbf{k}|^2 = \frac{\hbar^2}{2m^*}k^2 = \frac{\hbar^2}{2m^*}\left(k_x^2 + k_y^2 + k_z^2\right) \qquad 2.13$$

In the ground state of a bulk material the total volume of states in k-space with a value less than some constant value of, k, is given by a sphere of radius, k, and volume, V_k. While the volume of k-space occupied by a single electronic state is given by a cube of volume V_s. Therefore the total number of states in such a sphere can thus be written as:

$$N_s = \frac{V_k}{V_s} = \frac{4\pi k^3/3}{(2\pi/L)^3} = \frac{L^3k^3}{6\pi^2} \qquad 2.14$$

In order to simplify this expression the dimensions of the crystal, L_x, L_y and L_z, have all been set equal to L. If the density of **k** states in k space is known through all of k space,

then the number of states N_s contained within the k space volume, V_k can be obtained by integrating the density of states over that volume. This statement is summarised by the following mathematical expression [11].

$$\int_{\kappa} \rho(k)dk = \frac{N_s}{V} \qquad 2.15$$

where $\rho(k)$ is known as the density of states. The volume of the crystal, V, appears in the integral such that it yields the number of states per unit volume of the crystal. By differentiating Equation 2.15 with respect to k and substituting for N_s the following expression is obtained.

$$\rho(k) = \frac{1}{V}\frac{dN_s}{dk} = \frac{k^2}{2\pi^2} \qquad 2.16$$

This equation does not account for the two fold degeneracy of the spin states. In most cases the density of states is required as a function of energy. Using the relation,

$$\rho(\mathscr{E})d\mathscr{E} = \rho(k)dk \rightarrow \rho(\mathscr{E}) = \frac{\rho(k)}{d\mathscr{E}/dk} \qquad 2.17$$

it is possible to obtain the density of states as a function of energy. Therefore in a bulk semiconductor crystal that has a parabolic band structure, the density of states function can be written as:

$$\rho(\mathscr{E}) = \frac{\sqrt{\mathscr{E}}}{4\pi^2}\left(\frac{2m^*}{\hbar^2}\right)^{3/2} \qquad 2.18$$

Figure 2.5(a) shows the density of states in a bulk crystal as a function of energy. The density of states function for an infinitely deep quantum well will now be derived. We therefore consider N electrons confined to a crystal of dimensions L_x, L_y and L_z, in which

$L_y << L_x$ and L_z. As a result of quantization in the y-direction, the total volume of each sub-band is now represented by a disk of radius k. This results in the following expression for the number of states in a sub-band. (Again, in order to simplify these expressions L_x and L_z are set equal to L.)

$$N_s = \frac{\pi k^2}{(2\pi / L)^2} = \frac{L^2 k^2}{4\pi} \qquad 2.19$$

Following a similar procedure to that used in the bulk case, the total number of **k** states per unit volume of crystal is given by

$$\rho(k) = \frac{k}{2\pi L_x}. \qquad 2.20$$

Using Equation 2.17 the two dimensional density of states may be expressed as a function of energy.

$$\rho(\mathscr{E}) = \frac{m^*}{2\pi\hbar^2}\left(\frac{1}{L_x}\right) \qquad 2.21$$

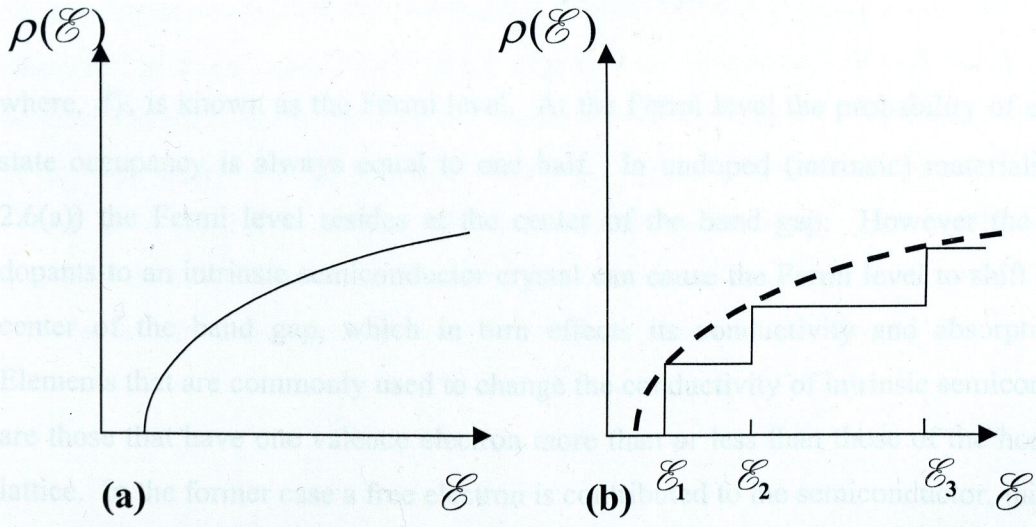

Figure 2-5 Density of states versus energy for (a) bulk and (b) quantum well structures.

Figure 2.5(b) shows the density of states as a function of energy in a typical quantum well structure. This graph reveals a step like function as opposed to the continuous parabolic curve obtained for the bulk case [12]. One of the interesting features with regard to the two dimensional system is that the density of states is non zero at the band edge, unlike in a three dimensional system. This has important implication for gain and absorption in quantum well systems, since a high peak gain requires the population inversion of levels which have a high density of states. In a bulk laser this can only be achieved after first filling the lower lying energy levels. In a quantum well laser this is unnecessary as the peak gain is associated with levels at the bottom of the band.

2.6.5 Fermi-Dirac Statistics and Doping.

As electrons are fermions they obey Fermi-Dirac statistics. Therefore at a given temperature, T, the probability that an electronic state with energy, $\mathscr{E}$, is occupied is given by the Fermi-Dirac distribution.

$$f(\mathscr{E}) = \frac{1}{1+\exp(\mathscr{E}-\mathscr{E}_F)/kT} \qquad 2.22$$

where, $\mathscr{E}_F$, is known as the Fermi level. At the Fermi level the probability of electronic state occupancy is always equal to one half. In undoped (intrinsic) materials (Figure 2.6(a)) the Fermi level resides at the center of the band gap. However the addition dopants to an intrinsic semiconductor crystal can cause the Fermi level to shift from the center of the band gap, which in turn effects its conductivity and absorption [13]. Elements that are commonly used to change the conductivity of intrinsic semiconductors, are those that have one valence electron more than or less than those of the host crystal lattice. In the former case a free electron is contributed to the semiconductor, this type of impurity is called a donor since it donates an electron to the material. Semiconductors doped in this way are referred to as n-type materials. Figure 2.6(b) shows the position of the Fermi level relative to conduction and valence bands in n-type material.

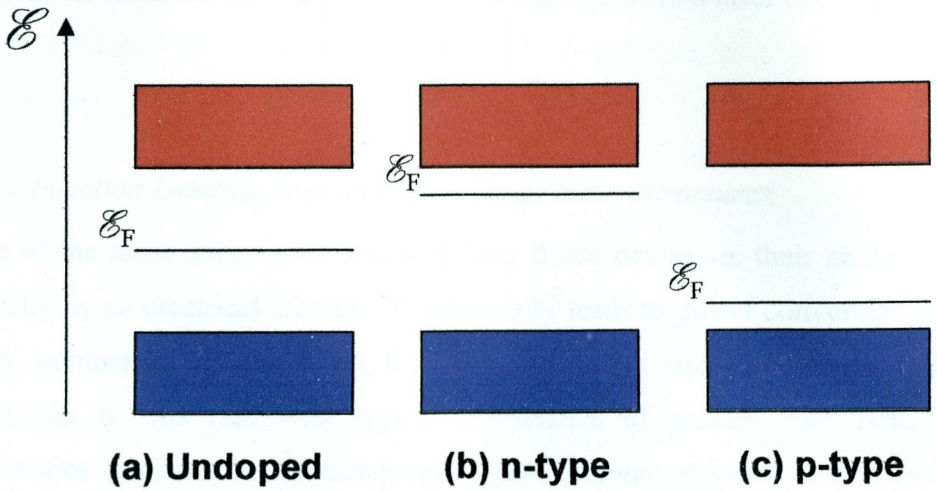

Figure 2-6 The relative positions of the Fermi level in (a) intrinsic, (b) n-type and (c) p-type semiconductor material.

In the latter case one of the covalent bonds formed by the impurity element will be short one electron, this deficiency may be compensated for by acquiring an electron from a neighboring atom. In this way the vacancy, usually called a hole, can travel through the lattice and serve as an additional free charge carrier. Elements such as these are termed acceptors as they may accept one free electron from the crystal. Semiconductors doped in this way are referred to as p-type materials. Figure 2.6(c) shows the position of the Fermi level relative to conduction and valence bands in a p-type material. The conductivity of intrinsic material will be increased by either n-type or p-type doping, as both processes increase the number of free charge carriers in the material.

2.7 A Brief History of the Laser Diode.

In the next few subsections we outline the major steps in the history of the laser diode. With regard to the subject matter in this thesis, the main point of this synopsis is to outline the rationale behind incorporating a waveguide in a laser diode device.

2.7.1 Injection Luminescence and Laser Diode Heterostructures.

One of the most important features of laser diode devices is their ability to be pumped directly by an electrical current. This typically leads to power conversion efficiencies of 50%, compared to around 1% for most solid state and gas lasers. CO_2 lasers are exception to this rule with typical efficiencies of greater than 10%. The energy conversion process in semiconductor opto-electronic devices is known as injection luminescence, it is this process that is responsible for the high efficiency of such devices. Injection luminescence is the emission of radiation due to the recombination of injected carriers at a forward biased p-n junction. This process can be explained qualitatively by making reference to an energy band diagram of a p-n junction.

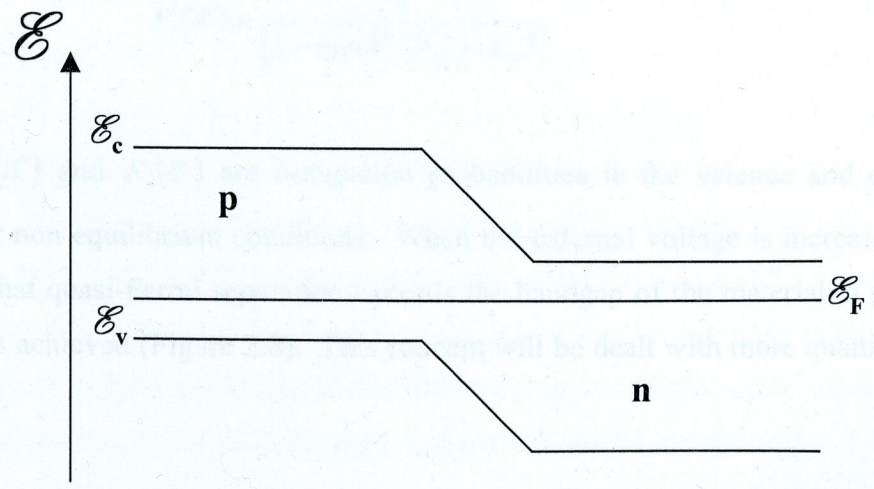

Figure 2-7 Energy band diagram as a function of distance across an unbiased p-n junction.

Figure 2.7 shows the how the energy bands of n-type and p-type materials are altered when they are brought into contact to form a p-n junction. After the materials are brought into contact carriers diffuse across the junction, causing the Fermi level to become continuous. The diffusion of electrons and holes across the junction also results in the formation of a thin depletion region. Within this region the electrons and holes are sparse with positively ionized donor atoms on one side of the junction and negatively ionized acceptors on the other side. This carrier distribution now present sets up an electric field, which distorts the energy bands in the vicinity of the junction. Applying a so-called "forward bias" potential difference, reverses the electric field across the junction, this forces more carriers into the depletion layer where they recombine. Since there is no longer an equilibrium situation the Fermi level is no longer continuous across the junction. Instead the electron and hole populations statistics on either side of the junction are now governed by quasi-Fermi levels. Equations 2.23 and 2.24 give the occupation probabilities for conduction and valence band in terms of the quasi-Fermi levels, $\mathscr{E}_{Fc}$ and $\mathscr{E}_{Fv}$.

$$F_c(\mathscr{E}) = \frac{1}{\left[1+\exp(\mathscr{E}-\mathscr{E}_{Fc})/k_BT\right]} \qquad 2.23$$

$$F_v(\mathscr{E}) = \frac{1}{\left[1+\exp(\mathscr{E}-\mathscr{E}_{Fv})/k_BT\right]} \qquad 2.24$$

Where $F_c(\mathscr{E})$ and $F_v(\mathscr{E})$ are occupation probabilities in the valence and conduction band under non equilibrium conditions. When the external voltage is increased to such an extent that quasi-Fermi separation exceeds the bandgap of the material, a population inversion is achieved (Figure 2.8). This concept will be dealt with more quanitatively in Section 2.8.

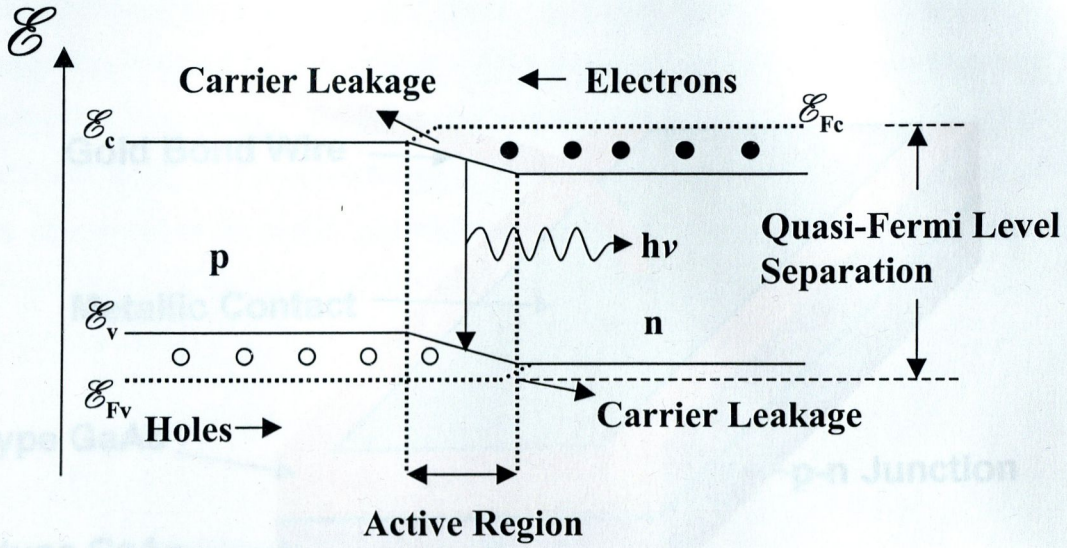

Figure 2-8 Energy band diagram as a function of distance across a forward biased p-n junction.

The first semiconductor lasers were nothing more than electrically contacted p-n junctions of the type just described above. Figure 2.9 is a schematic illustration of an early GaAs homojunction device. In this type of laser, optical gain is provided by a forward biased GaAs p-n junction, and an optical cavity is formed by the cleaved GaAs crystal facets at each end of the device. While structures such as these proved that is was possible to fabricate laser devices from semiconductor materials, threshold current densities in excess of 50,000 A/cm^2 meant room temperature operation was impossible. The problem with homojunction devices was that they had no mechanism for providing either carrier or optical confinement. In effect the width of the active region in these devices, was defined by the diffusion length of carriers within the material.

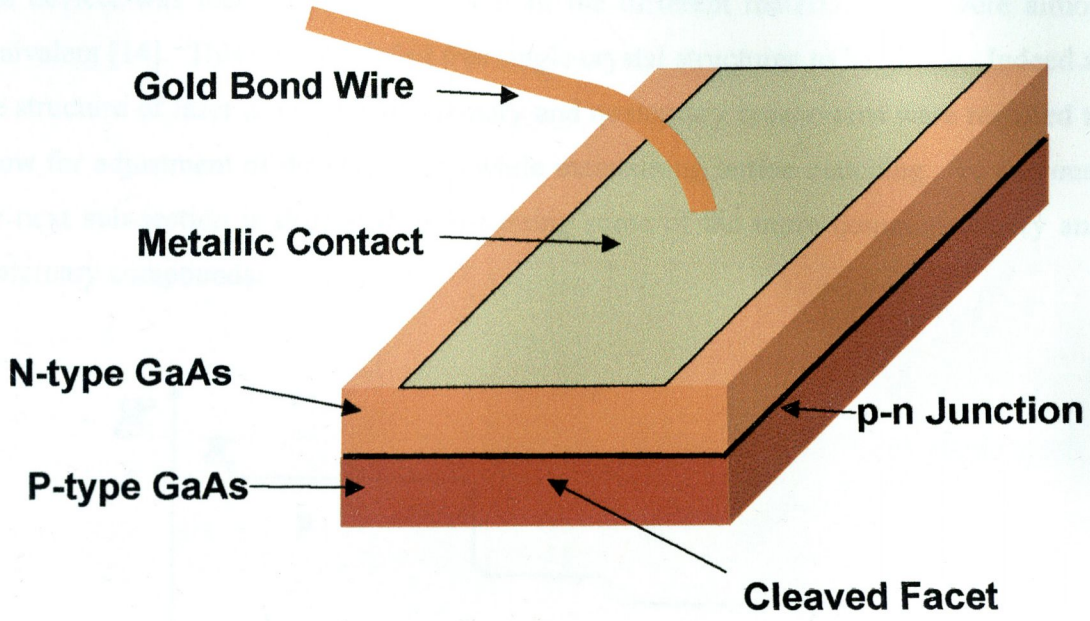

Figure 2-9 Illustration of a simple homojunction laser diode.

The failings of homojunction lasers were addressed with the invention of the double heterostructure device. In a double heterosturcture, materials with different bandgaps are incorporated into the junction. Figure 2.10(a) shows the bandgap variation across an unbiased double heterostructure device. As the thin central region has a bandgap that is smaller than the surrounding material, it acts to trap carriers injected from the doped regions on either side. In structures of this type the width of the active region could effectively be defined by the thickness of the narrow bandgap region. This allowed the fabrication of low threshold devices, which were capable of room temperature operation. The relative extent to which the total change in bandgap energy impacts upon the conduction and valence bands, is determined by the band offsets of the particular material involved. Thus the choice of material used will have a bearing on how effectively a particular structure traps the different types of carriers. Figure 2.10(b) shows a double heterostructure laser under forward bias. The smaller index of refraction of the doped cladding layers, means that the active region acts as a waveguide, which confines light to

a well defined optical mode. Furthermore, since the evanesnant field of the optical mode propagates in wider bandgap material, the internal losses of the optical mode are also reduced. The first double heterostructure devices consisted of an intrinsic layer GaAs sandwiched between two doped AlGaAs layers. A critical requirement in the design of this device, was that the lattice constants of the different materials used were almost equivalent [14]. This allowed defect free single crystal structures to be grown. Indeed as the structure of laser diode evolved, ternary and quaternary compounds were required to allow for adjustment of the energy gap while maintaining lattice matching. To this end, the next sub-section is dedicated to discussing some of the more common ternary and quaternary compounds.

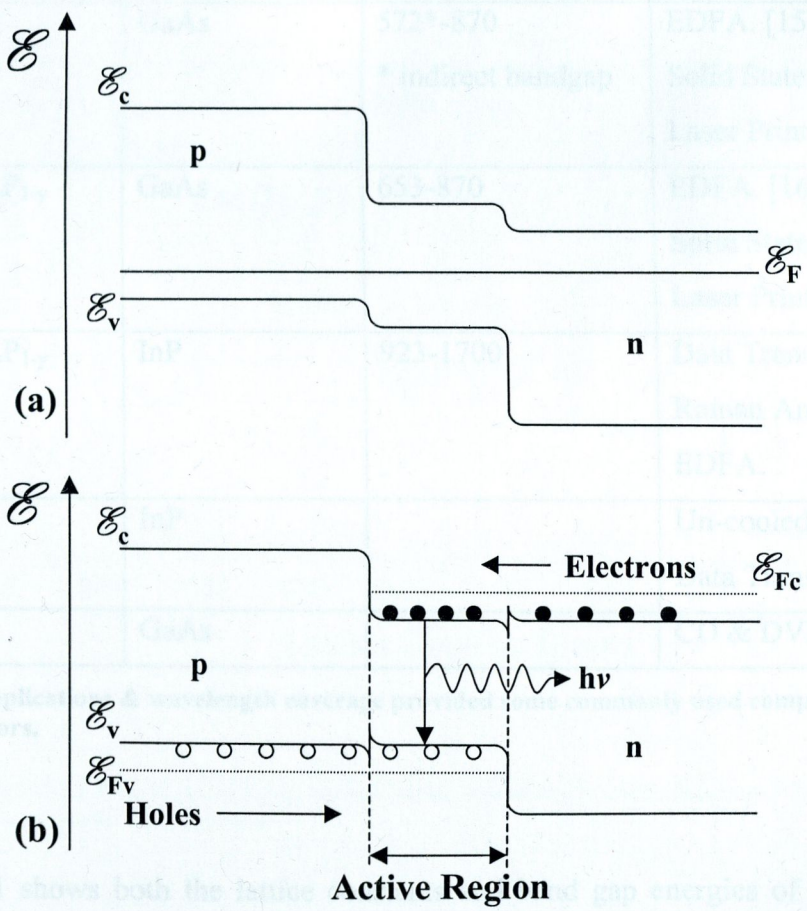

Figure 2-10 Energy band diagrams as a function of distance across (a) an unbiased double heterostructure device (b) a forward biased double heterostructure device.

2.7.2 Ternary and Quaternary Compounds.

At this point it is worth looking at some of semiconductor compounds, from which laser diodes are fabricated. To a large degree the emission wavelength required from a laser diode device determines what alloy system it will be fabricated from, or at the very least the substrate material it will be grown on. Table 2.1 lists some of the more common semiconductor material systems, along with the wavelength range spanned by these materials, and applications for laser diodes at these wavelengths.

Semiconductor Compound	**Substrate**	**Spectral Coverage (nm)**	**Applications**
$Al_xGa_{1-x}As$	GaAs	572*-870 * indirect bandgap	EDFA. [15] Solid State Pump Lasers Laser Printers
$In_{1-x}Ga_xAs_yP_{1-y}$	GaAs	653-870	EDFA. [16] Solid State Pump Lasers Laser Printers
$In_{1-x}Ga_xAs_yP_{1-y}$	InP	923-1700	Data Transmission. Raman Amplifiers [17]. EDFA.
AlGaInAs	InP		Un-cooled Lasers for Data Transmissions [18].
AlGaInP	GaAs		CD & DVD lasers [19]

Table 2-1 Applications & wavelength coverage provided some commonly used compound semiconductors.

Figure 2.11 shows both the lattice constants and band gap energies of some common binary semiconductor compounds. The compounds of most importance in this plot are GaAs and InP, because not only are they used as epi-layers in many laser diode devices, but they also serve as the substrate material for almost all laser diodes in use today. Also

shown on this plot are two of the most important material systems used to fabricate laser diode devices, $Al_xGa_{1-x}As$ and $In_{1-x}Ga_xAs_yP_{1-y}$. $Al_xGa_{1-x}As$ lattice matched to GaAs is the material system most commonly used to provide laser emission at 980nm. While $In_{1\_x}Ga_xAs_yP_{1-y}$ lattice matched to InP is the material system most commonly used to provide laser emission at 1300nm and 1550nm. Using the semiconductor alloy systems discussed above it is possible to fabricate semiconductor devices, which confine carriers and photons to different extents.

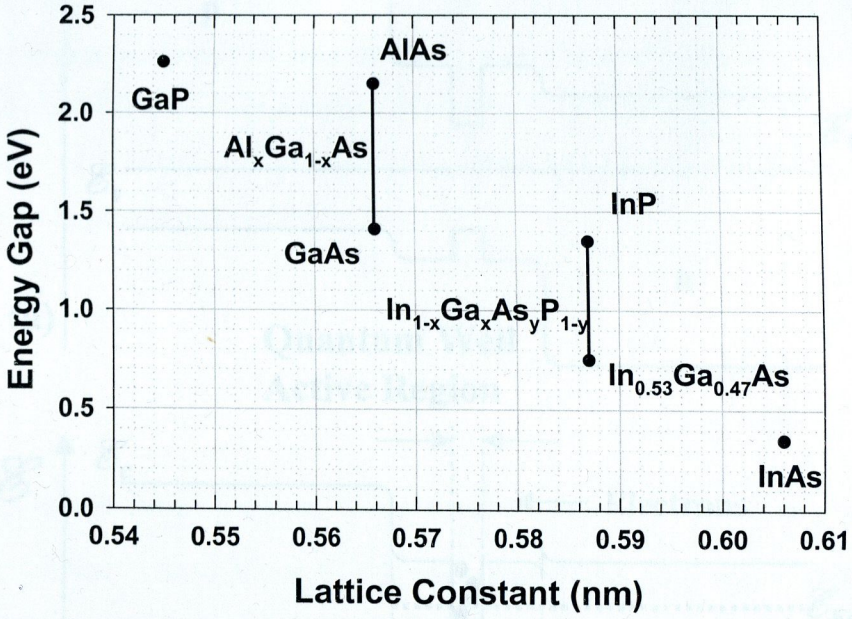

Figure 2-11 Plot of energy gap versus lattice constant for some common binary semiconductor compounds.

2.7.3 The Separate Confinement Heterostructure (SCH).

The rationale behind a separate confinement heterostructure is easy to understand, use a tiny active region to lower the threshold of the device, while employing a separate larger waveguide to confine the optical mode effectively. The ability of modern growth techniques to fabricate, so called, quantum well devices has already been discussed (Section 2.6.3). In separate confinement heterostructures quantum wells are employed to provide carrier confinement. Depending on the intended application a device may contain several quantum wells.

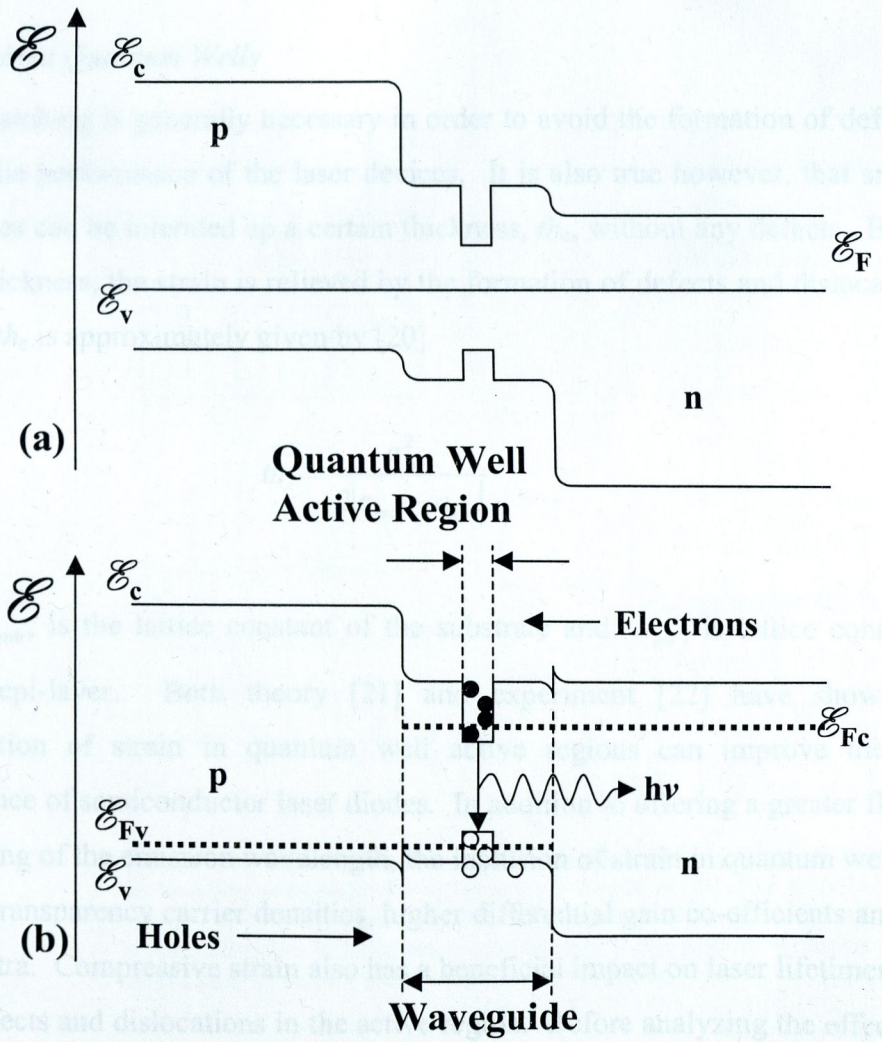

Figure 2-12 Energy band diagrams as a function of distance across (a) an unbiased separate confinement heterostructure (b) a forward biased separate confinement heterostructure.

As the quantum wells by themselves provide poor optical confinement they are generally placed in the center of a separate waveguiding structure. The introduction of a separate intrinsic waveguiding layer, allows the overlap of the optical mode with the doped cladding regions to be minimized. This in turn further reduces the internal losses of the device beyond what is attainable from a double heterostructure. Figures 2.12(a) and (b) show the energy band diagram across, (a) an unbiased SCH, (b) a forward biased SCH. Figure 2.12(b) also attempts to show how small offsets (in this case in the valence band) can lead to carrier leakage from the quantum wells.

2.7.4 Strained Quantum Wells

Lattice matching is generally necessary in order to avoid the formation of defects which degrade the performance of the laser devices. It is also true however, that small lattice mismatches can be tolerated up a certain thickness, th_c, without any defects. Beyond this critical thickness, the strain is relieved by the formation of defects and dislocations. The value of, th_c is approximately given by [20]

$$th_c = \frac{a_{sub}^2}{2\left|a_{sub} - a_{epi}\right|} \qquad 2.25$$

where, a_{sub}, is the lattice constant of the substrate and, a_{epi}, is lattice constant of the strained epi-layer. Both theory [21] and experiment [22] have shown that the incorporation of strain in quantum well active regions can improve the operating performance of semiconductor laser diodes. In addition to offering a greater flexibility in the tailoring of the emission wavelength, the inclusion of strain in quantum wells can lead to lower transparency carrier densities, higher differential gain co-efficients and narrower gain spectra. Compressive strain also has a beneficial impact on laser lifetimes as it helps to pin defects and dislocations in the active region. Before analyzing the effects of strain on semiconductor band structure, we first define what is meant by tensile and compressive strain

Compressive Strain: If the lattice constant of the epi-layer is larger than that of the substrate, the resulting strain will be compressive in the plane of the layer, and tensile strain in the direction perpendicular to the interface.

Tensile Strain: If the lattice constant of the epi-layer is less than that of the substrate then the strain in the plane of the layer is tensile, and compressive strain in the perpendicular direction.

Figures 2.13(a) and (b) respectively illustrate the concepts of compressive and tensile strain

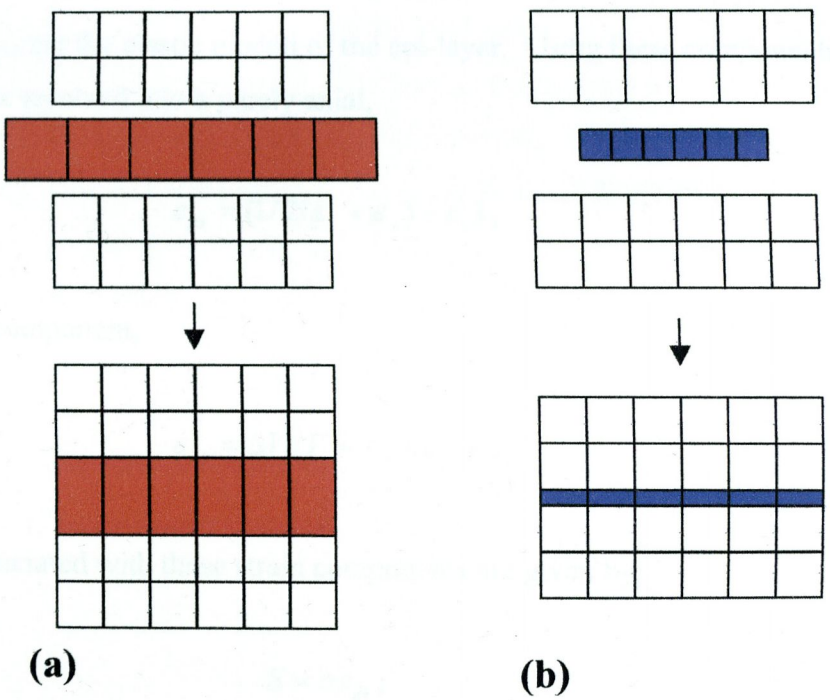

Figure 2- 13 (a) Compressive strain - the strained layer is compressed in the plane perpendicular to the growth direction but relaxes by expanding in the growth direction. (b) Tensile strain - The strained layer is stretches in the plane perpendicular to the growth direction but relaxes by contracting in the growth direction

Since the energy band gap of a semiconductor is related to its lattice constant, the distortion of the crystal lattice due to strain leads to an alteration in the bandgap of the strained layer. The in-plane strain component, $\varepsilon_{\parallel}$, is given by

$$\varepsilon_{\parallel} = -\varepsilon_x = -\varepsilon_y = \frac{a_{epi} - a_{sub}}{a_{sub}} \qquad 2.26$$

while the component of strain perpendicular to the plane of the epi-layer is given by

$$\varepsilon_{\perp} = \varepsilon_z = 2\frac{C_{12}}{C_{11}}\varepsilon_{\parallel} \qquad 2.27$$

where C_{11} and C_{12} are the elastic moduli of the epi-layer. Using these components the total strain can be resolved into a purely axial,

$$\varepsilon_{ax} = (1/2(\varepsilon_x + \varepsilon_y) - \varepsilon_z), \qquad 2.28$$

and hydrostatic component,

$$\varepsilon_{hy} = \Delta V / V = \varepsilon_x + \varepsilon_y + \varepsilon_z. \qquad 2.29$$

The energies associated with these strain components are given by,

$$S = b\varepsilon_{ax}, \qquad 2.30$$

and

$$H = c\varepsilon_{hy}, \qquad 2.31$$

where b and c are lattice deformation potentials, which relate energy shifts in the band structure to the strain components. Using Equations 2.26 and 2.27, H and S can be expressed purely in terms of the elastic moduli and the deformation potentials.

$$H = -2b\frac{C_{11} - C_{12}}{C_{11}}\varepsilon_{\parallel} \qquad 2.32$$

$$S = -c\frac{C_{11} + 2C_{12}}{C_{11}}\varepsilon_{\parallel} \qquad 2.33$$

The axial and hydrostatic components of strain alter the band structure of a semiconductor in different ways. Firstly the hydrostatic component of the strain shifts both the conduction and valence bands. In the case of compressive strain there is an upward shift in the conduction and a downward shift in the valence band resulting in an overall increase in the bandgap energy. For tensile strain the conduction band moves downward and the valence band moves upward resulting in a decrease in the bandgap energy. Secondly, the axial component of the strain lifts the degeneracy of the valence maximum forcing the heavy hole and light hole bands to separate. These effects are summarized qualitatively in Figure 2.14.

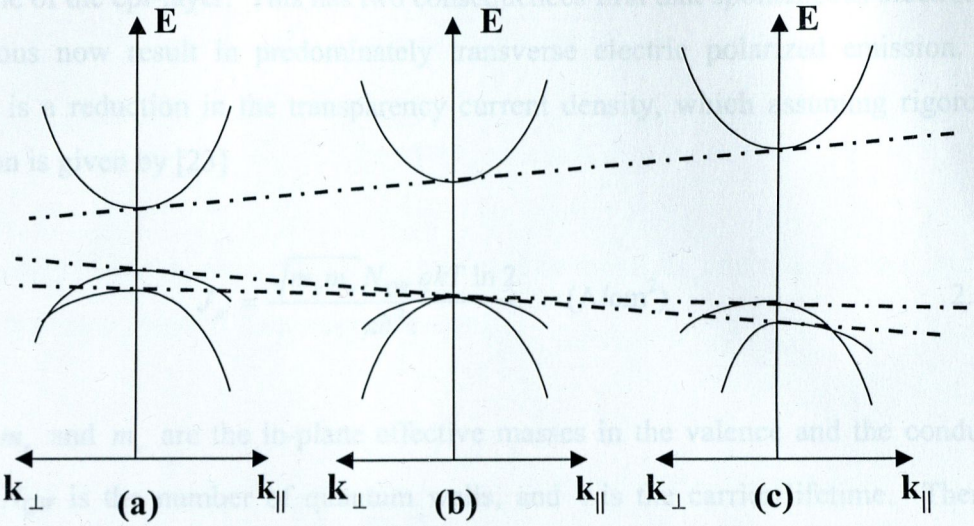

Figure 2-14 Changes in semiconductor band structure resulting from (a) tensile strain, (b) no-strain and (c) compressive strain.

In a bulk material with an unstrained band gap of, E_g, the energy separation between the heavy hole and the conduction band, $E_{C.HH}$, when influenced by strain is given by

$$E_{C,HH} = E_g + H - S \qquad 2.34$$

Similarly the energy separation between the light hole and the conduction band, $E_{C,LH}$, when under the influence of strain is given by

$$E_{C,LH} = E_g + H + S \qquad 2.35$$

Referring back to Figure 2.14, it is also apparent that the presence of strain changes the curvature of the of valence bands, this in turn changes the effective masses associated

with these bands. Under compressive strain the axial component splits the degeneracy of the valence band maximum, with the heavy hole being lifted above the light hole. The heavy hole effective mass is large in the growth direction but is significantly reduced in the plane of the epi-layer. This has two consequences first that spontaneous electron-hole transitions now result in predominately transverse electric polarized emission. The second is a reduction in the transparency current density, which assuming rigorous k-selection is given by [23]

$$J_{tr} = \frac{\sqrt{m_c m_v}\, N_{QW}\, qkT \ln 2}{\pi \hbar^2 \tau} \quad (\mathrm{A/cm^2}) \qquad 2.36$$

where m_c and m_v are the in-plane effective masses in the valence and the conduction bands, N_{QW} is the number of quantum wells, and τ is the carrier lifetime. Therefore devices with compressively strained quantum wells demonstrate reduced threshold currents. Under tensile strain the light hole effective mass is low in the growth direction, but is increased in the in-plane direction.

2.8 Gain.

Material gain is the proportional growth of the photon density per unit length. It is only achieved in a semiconductor material when the number of stimulated downward transitions exceeds the number of upward transitions. The rates at which absorption, stimulated emission and spontaneous emission occur, depend on the occupation probabilities in the conduction and valence band. Furthermore the processes of absorption and stimulated emission are proportional to the electric field intensity, $|E|^2$, while the rate of spontaneous emission is proportional to the vacuum field intensity $|E^v|^2$. In order to work out these rates we initially consider the semiconductor energy gap as a two level system, in which energies of the conduction and valence bands are denoted by, $\mathscr{E}_2$ and $\mathscr{E}_1$, respectively. In this approach the occupation probabilities in the valence and

conduction bands under non-equilibrium conditions, are described by Equations 2.37 and 2.38 respectively.

$$f_1 = \frac{1}{1+\exp(\mathscr{E}_1 - \mathscr{E}_{Fv})/k_B T} \qquad 2.37$$

$$f_2 = \frac{1}{1+\exp(\mathscr{E}_2 - \mathscr{E}_{Fc})/k_B T} \qquad 2.38$$

The transition rates of, absorption R_{12}, stimulated emission R_{21} and spontaneous emission R_{sp} are therefore given by following Equations:

$$R_{12} = R_r f_1(1-f_2) \qquad 2.39$$

$$R_{21} = R_r f_2(1-f_1) \qquad 2.40$$

$$R_{sp} = R_r^{sp} f_2(1-f_1) \qquad 2.41$$

where R_r is the radiative transition rate which would exist if all state pairs were able to participate in the in the transition, assuming rigorous **k** selection. In the case of the spontaneous emission rate, $R_r^{sp} = R_r$ as $|E^v|^2 \rightarrow |E|^2$. From Equation 2.39 and 2.40 the net stimulated emission rate can be defined as

$$R_{st} = R_{21} - R_{12} = R_r(f_2 - f_1) \qquad 2.42$$

this quantity is directly proportional to the optical gain in the material. Since under non-equilibrium conditions the quasi-Fermi level separation, $\Delta\mathscr{E}_F$, is slightly less than the applied voltage across the junction, it is possible to write.

$$\frac{R_{21}}{R_{12}} = \frac{f_2(1-f_1)}{f_1(1-f_2)} = \exp((\Delta\mathscr{E}_F - \mathscr{E}_{21})/k_B T) \qquad 2.43$$

where $\mathscr{E}_{21}$ is the magnitude of the energy gap. Equation 2.43 reveals that the stimulated emission rate be will larger than the absorption rate if,

$$\Delta\mathscr{E}_F > \mathscr{E}_{21} \qquad 2.44$$

This means that the net stimulated emission rate will only be positive when the quasi Fermi level separation is greater the transition energy of interest. Further since the transition energy must at the very least be equal to the bandgap of the material. It can therefore be stated that in order to achieve optical gain in the active region, the voltage across a p-n junction must be greater than the bandgap energy.

2.8.1 Fermi's Golden Rule

To fully evaluate the three transition rates, R_{12} R_{21} R_{sp}, we need only quantify the radiative transition rate, R_r, which occurs in Equations 2.39 to 2.41. Fermi's golden rule is an expression, which describes the rate of decay from an initial state to a continuum of final states in the presence of a time dependent perturbation. Using Fermi's golden rule the transition rate from an initial state to a continuum of final states, $\rho_f(\mathscr{E}_{21})$, is given by

$$R_r = \frac{2\pi}{\hbar}|H_{21}|^2 \rho_f(\mathscr{E}_{21}) \qquad 2.45$$

where the matrix element $|H_{21}|^2$ describes the overlap between the initial and final states and thus the interaction strength between the two states. In a semiconductor material both the initial and final states of the electron are immersed within a large number of nearby states. In this case the final density of states in Equation 2.45 should actually be interpreted as the density of transitions per unit energy. However by assuming strict **k** selection, it is possible to pair up states in the conduction and valence bands. This allows a single density of states function to be used to describe the allowed number of

transitions, as opposed to one for the conduction band and one for the valence band. The reduced density of states as it is referred to can written as [24]

$$\frac{1}{\rho_r(\mathscr{E}_{21})} = \frac{1}{\rho(k)}\frac{d\mathscr{E}_{21}(k)}{dk} = \frac{1}{\rho(k)}\left[\frac{d\mathscr{E}_2(k)}{dk} - \frac{d\mathscr{E}_1(k)}{dk}\right] \qquad 2.46$$

This definition allows $\rho_r(\mathscr{E}_{21})$ to be evaluated at any given point in k-space once the derivatives of the electron and hole energies with respect to k are known. In a semiconductor the transition rate R_r must be written in terms of the reduced density of states as follows

$$R_r = \frac{2\pi}{\hbar}|H_{21}|^2 \rho_r(\mathscr{E}_{21}) \qquad 2.47$$

2.8.2 A General Expression for Optical Gain

As stated previously material gain per unit length is defined as the proportional growth of the photon density as it propagates along some direction in the crystal. This definition can be related back to the transition rates as follows,

$$g = \frac{1}{N_p}\frac{dN_p}{dz} = \frac{1}{v_g N_p}\frac{dN_p}{dt} = \frac{1}{v_g N_p}(R_{21} - R_{12}) \qquad 2.48$$

Here the group velocity, v_g, is used to transform the spatial growth rate to the growth rate with respect to time. The temporal growth is then equated to the net generation rate of photons per unit volume.

$$g = \frac{R_{st}}{v_g N_p} = \frac{R_r}{v_g N_p}(f_2 - f_1) \qquad 2.49$$

Finally substituting for, R_r, using Fermi's Golden rule (Equation 2.47), we have

$$g(\hbar\omega) = \frac{2\pi}{\hbar}\frac{|H_{21}|^2}{v_g N_p}\rho_r(\mathscr{E}_{21})\cdot(f_2 - f_1) \qquad 2.50$$

This expression can be developed further by considering the matrix element, $|H_{21}|^2$, in more detail, the interested reader will find a more in depth analysis of the matrix element in references [25][26]. It suffices here to say that the term, $\frac{2\pi}{\hbar}\frac{|H_{21}|^2}{v_g N_p}\rho_r(\mathscr{E}_{21})$, is a property of the material, while the Fermi factor, $f_2 - f_1$, is a function of the carrier injection level.

2.9 Optical Waveguiding

It was previously stated that early homojunction laser diodes had no means of providing optical confinement, and as a result these early devices were very inefficient. The incorporation of optical waveguides in laser diodes improved the operating efficiency of such devices.

2.9.1 The Slab Waveguide

In order to provide optical confinement it is necessary to incorporate a waveguide into the laser cavity. In the transverse direction, this is usually achieved by growing dielectric layers of different refractive index. The simplest example of such a waveguide is the symmetric three layer slab waveguide. Figure 2.15 shows an example of such a structure, in this illustration the refractive indices of the core and cladding are labeled n_1 and n_2 respectively, and the core thickness given by $2d$. Since the refractive index of the core is greater than those of the surrounding cladding layers, light in core will be guided due to total internal reflection for angles of incidence greater than the critical angle, ϕ_c. The critical is the angle between incident ray and the normal to the core cladding interface,

the measure this angle is set by the refractive indices of core and cladding layers (Equation 2.53). The following sections will consider the propagation of light in a symmetric slab waveguide, using the principles of both the geometrical and guided wave optics.

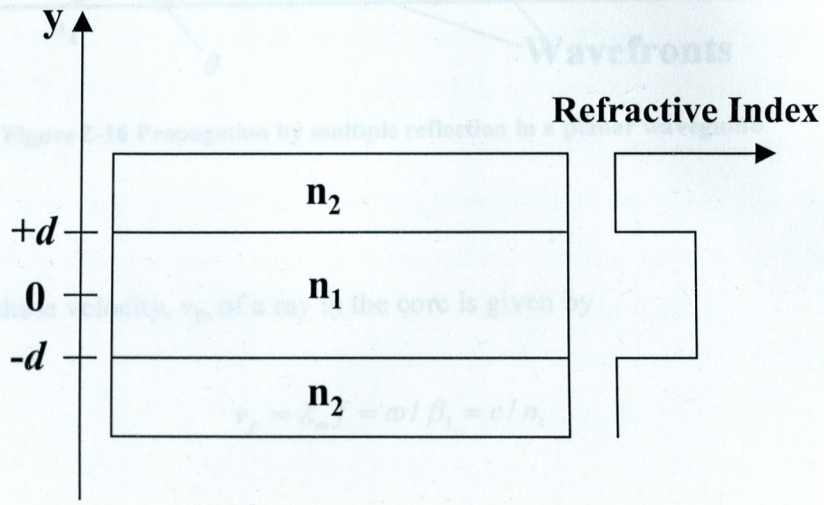

Figure 2-15 A symmetric three layer slab waveguide

2.9.2 The ray approximation

The ray approximation describes the propagation of light in the limit as the wavelength, $\lambda \to 0$, in this limit the effects of diffraction become negligible. Consider a ray of light propagating along the positive sense of the z-axis, in the core of a slab waveguide. A zig-zag path is traced out as the ray of light is reflected back and forth from each core cladding boundary. Figure 2.16 shows such a ray traveling at an angle θ to the plane of the waveguide.

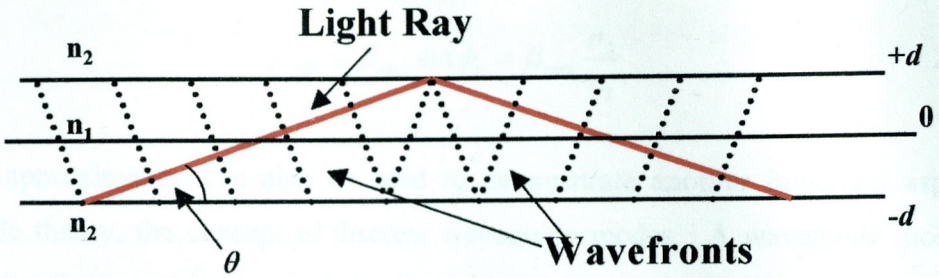

Figure 2-16 Propagation by multiple reflection in a planar waveguide

While the phase velocity, v_p, of a ray in the core is given by

$$v_p = \lambda_m f = \omega / \beta_1 = c / n_1 \qquad 2.51$$

the apparent phase velocity, $(v_p)_z$, with which associated wavefronts intercept any line parallel to the plane of the guide is given by

$$(v_p)_z = (\lambda_m \sec\theta) f = (\omega / \beta_1)\sec\theta = \omega / \beta_1 \cos\theta = \omega / \beta$$

$$\text{thus } \beta = \beta_1 \cos\theta \qquad 2.52$$

In this equation, β is the propagation constant of the guided wave in the core, while β_1 is the propagation constant of the plane wave in the guide layer. It is clear from this that the propagation constant of the guided wave must always be less than the propagation constant of the planes wave in the core. In light of this fact we henceforth refer to β_1 as β_{max}. Since a ray of light will only be guided, if its angle of incidence with the core cladding interface is greater than the critical angle, ϕ_c, the maximum angle of obliqueness, θ_m, can be calculated from

$$\cos\theta_m = \sin\phi_c = n_2 / n_1 \qquad 2.53$$

The critical angle therefore also determines a minimum value for β, which is given by

$$\beta_{\min} = \beta_{\max} \sin\phi_c = \beta_{\max} \frac{n_2}{n_1} \qquad 2.54$$

The ray approximation can also be used to demonstrate another important aspect of waveguide theory, the concept of discrete waveguide modes. A waveguide mode is a specific distribution of light, which is allowed to propagate in the core of a waveguide. Every allowed mode is characterized by a unique propagation constant. In order for a mode to be guided it must have a propagation constant β, such that $\beta_{\min} < \beta < \beta_{\max}$. It is also necessary that guided waves interfere constructively after a multiple reflections. Referring back to Figure 2.16 this condition is fulfilled only if [27]

$$2d \operatorname{cosec}\theta(1 - \cos 2\theta) = 4d \sin\theta \qquad 2.55$$

This means that there are only a finite number of allowed ray trajectories and thus a finite number of allowed modes. The angular deviation of the ray trajectories associated with guided modes is limited to a number of angles, these angles $\theta_{i = 1,2,3...}$ may be obtained from the relation

$$\sin\theta_i = \frac{i\lambda_m}{4d} = \frac{i\lambda}{4n_1 d} \qquad 2.56$$

2.9.3 Guided Wave Optics and the Helmholtz Equation

In the last section, light propagation in a slab was explained in terms of light rays being reflected back and forth from the core cladding boundaries. Although this approach proves useful for describing the behavior of light in multimode devices, it is inadequate for single mode waveguides. In such devices the wavelength of the radiation has roughly

the same dimensions as the core of the waveguide, this makes it more important to include the effects of diffraction. A more rigorous analysis is therefore necessary to therefore necessary to describe the propagation of light in these devices. Maxwell's equations for an inhomogenous, isotropic, non-conducting and space-charge free region may be written as.

$$\nabla \times \mathbf{E} = -\frac{\partial \mathbf{B}}{\partial t} \qquad 2.57$$

$$\nabla \times \mathbf{H} = \frac{\partial \mathbf{D}}{\partial t} \qquad 2.58$$

$$\nabla \cdot \mathbf{D} = \varepsilon_0 \nabla \cdot (\varepsilon_r \mathbf{E}) = \varepsilon_0 \left[\nabla(\varepsilon_r) \cdot \mathbf{E} + \varepsilon_r \nabla \cdot \mathbf{E} \right] = 0 \qquad 2.59$$

$$\nabla \cdot \mathbf{B} = 0 \qquad 2.60$$

Where $\mathbf{E}$ is the electric field vector, $\mathbf{D}$ is the electric displacement vector, $\mathbf{B}$ is the magnetic induction vector and $\mathbf{H}$ is the magnetic field vector. Also $\mathbf{D}$ is related to $\mathbf{E}$ via the expression $\mathbf{D} = \varepsilon_r \varepsilon_0 \mathbf{E}$ and $\mathbf{B}$ is related to $\mathbf{H}$ via the expression $\mathbf{B} = \mu_r \mu_0 \mathbf{H}$. By taking the curl of Equation 2.57 it can be rewritten in following form:

$$\nabla \times \nabla \times \mathbf{E} = -\mu_r \mu_0 \frac{\partial}{\partial t} (\nabla \times \mathbf{H}) \qquad 2.61$$

Now substituting Equation 2.58 into Equation 2.61 we obtain:

$$\nabla \times \nabla \times \mathbf{E} = -\mu_r \mu_0 \frac{\partial^2 \mathbf{D}}{\partial t^2} \qquad 2.62$$

The Laplacian operator, ∇^2, acting on a vector, $\mathbf{F}$, is defined as $\nabla^2 \mathbf{F} = \nabla(\nabla \cdot \mathbf{F}) - \nabla \times \nabla \times \mathbf{F}$. Using this identity [28] Equation 2.62 may be written in the following form

$$\nabla(\nabla \cdot \mathbf{E}) - \nabla^2 \mathbf{E} = -\mu_r \mu_0 \frac{\partial^2 \mathbf{D}}{\partial t^2} \qquad 2.63$$

Rearranging the right hand side of Equation 2.59 yields the following expression [29] for $\nabla \cdot \mathbf{E}$:

$$\nabla \cdot \mathbf{E} = \left(-\frac{1}{\varepsilon_r} \right) \nabla(\varepsilon_r) \cdot \mathbf{E} \qquad 2.64$$

Substituting Equation 2.64 into Equation 2.63 we obtain

$$\nabla^2 \mathbf{E} - \varepsilon_r \varepsilon_0 \mu_r \mu_0 \frac{\partial^2 \mathbf{E}}{\partial t^2} = -\nabla \left(\frac{1}{\varepsilon_r} \nabla(\varepsilon_r) \cdot \mathbf{E} \right) \qquad 2.65$$

If the refractive index takes the form of a step index profile the term on the right hand side of Equation 2.65 is non-zero only at the interfaces between the dielectric layers [30]. Thus assuming the electric field, **E**, varies as $e^{i\omega t}$, and that the refractive indices of both the core and cladding layers are constant, Equation 2.65 can be written in the form of the well known Helmholtz equation.

$$\nabla^2 \mathbf{E} + k_0^2 \varepsilon_r \mathbf{E} = 0 \qquad 2.66$$

where k_0 is the wave number in free space, which is defined by $k_0 = 2\pi / \lambda$. A similar wave equation for **H** can be derived from Equations 2.57 and 2.58 in the same way, this is

$$\nabla^2 \mathbf{H} + k_0^2 \varepsilon_r \mathbf{H} = 0 \qquad 2.67$$

Since we are interested in guided mode solutions whose z dependence can be written as $\exp(-i\beta z)$, the Laplace operator in Equations 2.66 and 2.67 assumes the form $\nabla = \partial^2 / \partial x^2 + \partial^2 / \partial y^2 - \beta^2$, where β is the propagation constant of the guided wave.

The wave equations for the Cartesian components of **E** and **H** can now be written out in the form.

$$\left(\frac{\partial^2}{\partial x^2}+\frac{\partial^2}{\partial y^2}\right)\psi+(n^2(x,y)k_0^2-\beta^2)\psi=0 \qquad 2.68$$

where ψ, can represent any of the field components $E_x\ E_y\ E_z\ H_x\ H_y\ H_z$. It is assumed that the solutions to Equation 2.68 are of the from

$$\psi=\psi_0(x,y)\exp\{-i(\omega t-\beta z)\}. \qquad 2.69$$

2.9.4 TE and TM modes

The concept of TE and TM can best be illustrated by reverting to the Cartesian component of Maxwell's equations. This process yields two independent solution sets, the first known as TE (transverse electric) is described by the equations [31]:

$$E_x=E_0(y)\exp\{-i(\omega t-\beta z)\} \qquad 2.70$$

$$H_y=\frac{\beta}{\mu_r\mu_0\omega}E_x \qquad 2.71$$

$$H_z=\frac{-1}{i\mu_r\mu_0\omega}\frac{\partial E_y}{\partial x} \qquad 2.72$$

In TE modes the electric field is polarized in the plane of the slab waveguide, in a laser diode device this would correspond to the plane of the active region. The other solution set,

$$H_x=H_0(y)\exp\{-i(\omega t-\beta z)\} \qquad 2.73$$

$$E_y=-\frac{\beta}{\varepsilon_r\varepsilon_0\omega}H_x \qquad 2.74$$

$$E_z = \frac{1}{i\varepsilon_r \varepsilon_0 \omega} \frac{\partial H_x}{\partial y} \qquad 2.75$$

describes what are known as TM (transverse magnetic) modes. In TM modes it is the magnetic field that is polarised in the plane of the waveguide. The field components of TE and TM modes can be summarized as follows.

TE modes	$\mathbf{E}(E_x,0,0)$ $\mathbf{H}(0,H_y,H_z)$
TM modes	$\mathbf{E}(0,E_y,E_z)$ $\mathbf{H}(H_x,0,0)$

As the optical confinement and facet reflectivity of TE modes are greater than their TM counterparts [32], it is normally the case that laser diode emission is TE polarized (Exceptions to this rule are structures that incorporate tensile strained quantum wells). The discussion here is therefore restricted to solutions of Equation A1.23. Further since we are dealing with a symmetric slab waveguide of the type in Figure 2.15, Equation A1.23 can be written in the following form

$$\frac{d^2E_x(y)}{\partial x^2} + (n_2^2k_0^2 - \beta^2)E_x(y) = 0 \qquad x > d$$

$$\frac{d^2E_x(y)}{\partial x^2} + (n_1^2k_0^2 - \beta^2)E_x(y) = 0 \qquad -d < x < d$$

$$\frac{d^2E_x(y)}{\partial x^2} + (n_2^2k_0^2 - \beta^2)E_x(y) = 0 \qquad x < -d \qquad 2.76$$

It can be shown that the form of the solutions [33] to these equations (which will be solved in Section 3.2.2) depends on the value of the propagation constant. Figure 2.17 illustrates some of the possible solutions of the Equations Set 2.76. For $\beta > k_0 n_1$, solution (a), $E_x(y)$ is exponential everywhere and is not a physically reasonable solution. For $k_0 n_2 < \beta < k_0 n_1$, solutions (b) and (c), while the electric field is sinusoidal in the core of the waveguide, it decays exponentially in the cladding layers. Such solutions are referred to as guided modes. At a given wavelength the number of guided will depend on the

thickness of the waveguide core and the refractive indices, n_1 and n_2. For $\beta < k_0 n_2$, solution (d), the solution is sinusoidal in all three layers. These solutions are known as radiation modes as they are not effectively guided by the structure.

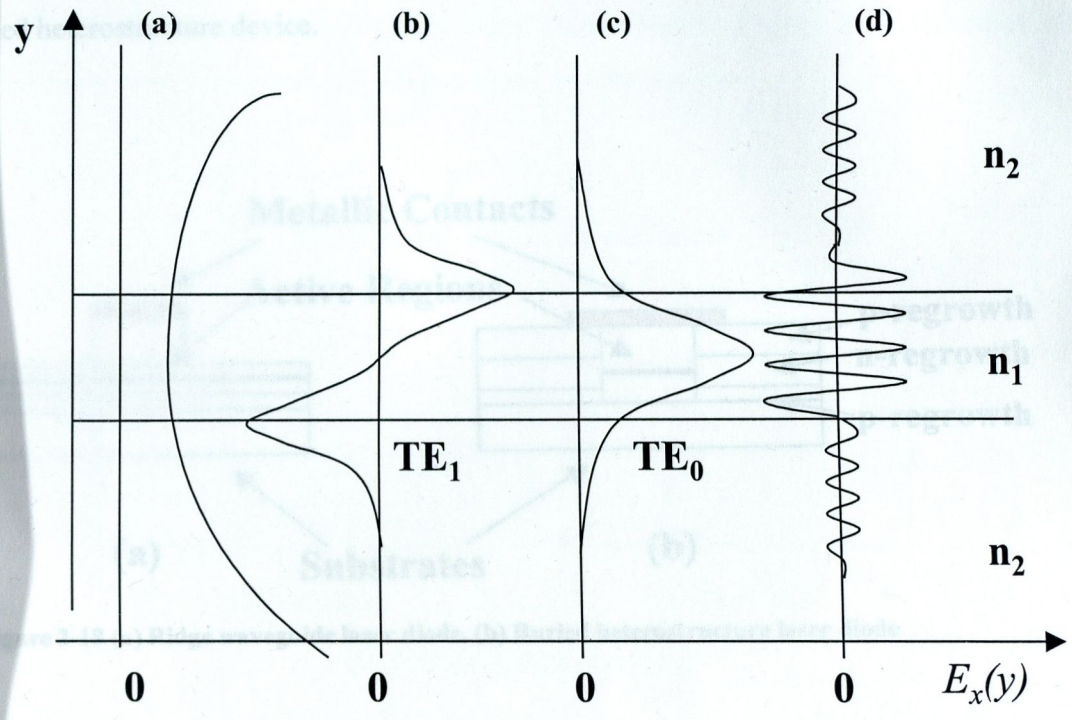

Figure 2-17 Possible solutions of Equation Set 2.76

2.9.5 Lateral Optical Confinement.

Perhaps the easiest way of providing optical confinement in the lateral direction is by defining a ridge on the surface of the semiconductor [34]. In this approach an oxide such as SiO is then deposited over the semiconductor surface except on the top surface of the ridge, such that this is the only region which is electrically contacted. It noted that these procedures are preformed before the wafer is cleaved up into individual devices. Using a numerical technique known as the effective index method (Section 3.2.3), it is possible to predict how light propagating underneath such a ridge structure will be guided. While

other more complicated device structures such as buried heterostructures [35] allow tighter confinement of the optical field in the lateral direction, ridge waveguide devices do however have the advantage that they require only a single crystal growth step. Figure 2.18 shows the epitaxial structure of both a typical ridge waveguide and one type of buried heterostructure device.

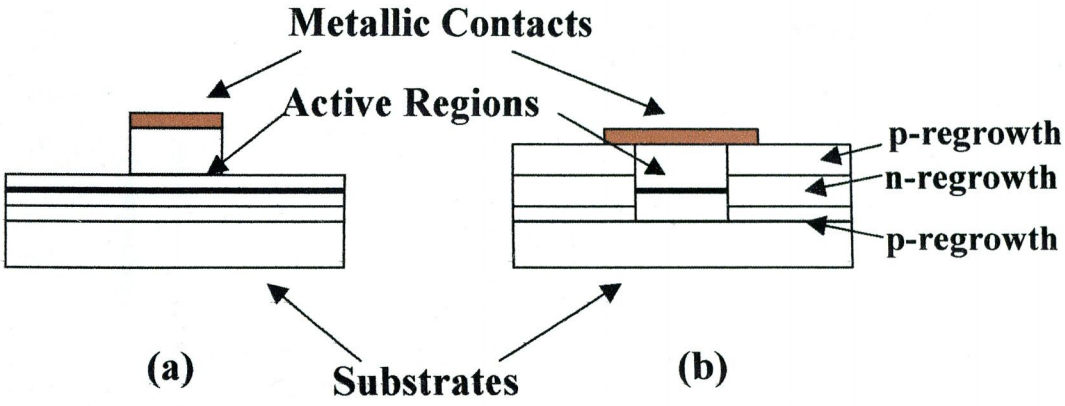

Figure 2-18 (a) Ridge waveguide laser diode, (b) Buried heterostructure laser diode

2.10 The Lo-guide Concept: Introduction & Rationale

In this section a novel waveguide design is introduced, which should allow increased single spatial mode light output from a ridge waveguide laser. One of the major applications for laser diodes emitting at λ=980nm is as pump sources for Erbium Doped Fibre Amplifiers (EDFA). In order to achieve efficient fibre coupling it is necessary that these devices lase in a single spatial mode. A common failure mechanism in these high power laser diodes is degradation of the facet due to catastrophic optical damage (COD) [36]. The internal power density at which COD occurs in GaAs lasers is roughly 10MW/cm^2 [37]. The area of a laser's emission aperture thus limits the power that can be obtained from it. Furthermore this problem cannot simply be solved by increasing the size of the emission aperture, since single lateral mode operation generally requires the active region to be less than or equal to 3μm in width. This requirement arises because in

order to prevent shifts in the optical mode due to carrier induced changes in the refractive index, the effective index, Δn_{eff}, associated with the ridge should be greater than or equal to 3.5×10^{-3} [15]. Ridge waveguides in which Δn_{eff} is less than 3.5×10^{-3}, suffer from effects which are associated with gain guided devices. Such effects include, kinks in the light-current characteristic [38] and beam instability. Gain guided devices also tend to support more longitudinal modes than index guided lasers. Figure 2.19 illustrates some of the characteristics of gain guided and index guided devices.

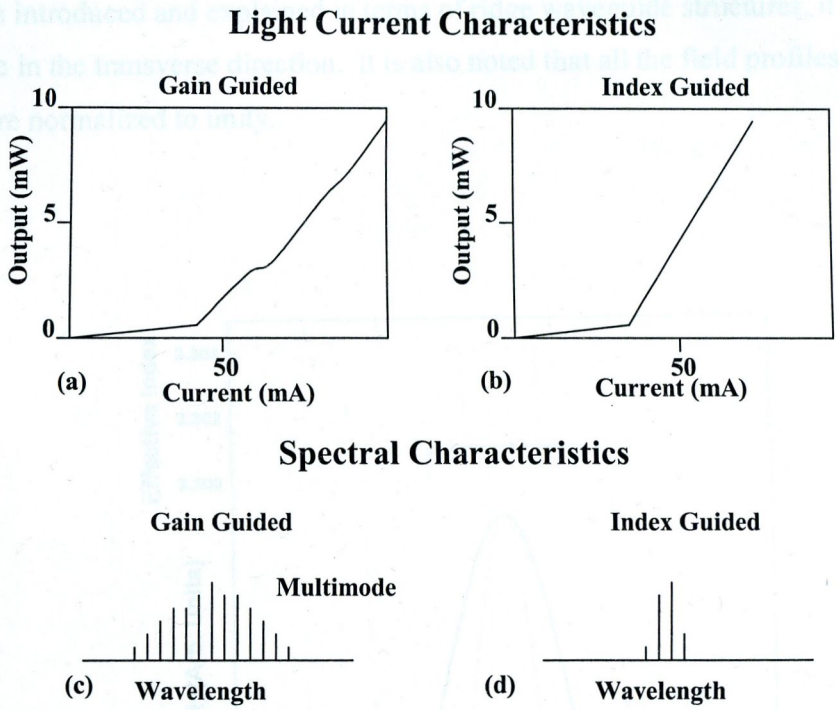

Figure 2-19 Typical light-current characteristics of (a) gain guided and (b) index guided laser diodes. Spectral characteristics associated with (a) gain guided and (b) index guided laser diodes

Although ridge waveguides in which $\Delta n_{eff} > 3.5\times10^{-3}$ achieve good device characteristics, they also support a second lateral mode if their width is increased beyond 2.9μm in width. This in turn limits the maximum output power obtainable from the device. There is therefore a trade off between the lateral spot size and mode stability. The following

subsections discuss a number of novel waveguide designs [39], which if implemented as a ridge waveguides, should allow single mode emission from apertures greater than 6μm in width.

2.10.1 Concept development.

This section introduces the simple rationale behind the novel waveguide concept, which is referred to as a Lo-guide structure. It is worth mentioning that although the Lo-guide concept is introduced and explained in terms of ridge waveguide structures, it is equally applicable in the transverse direction. It is also noted that all the field profiles in this Section are normalized to unity.

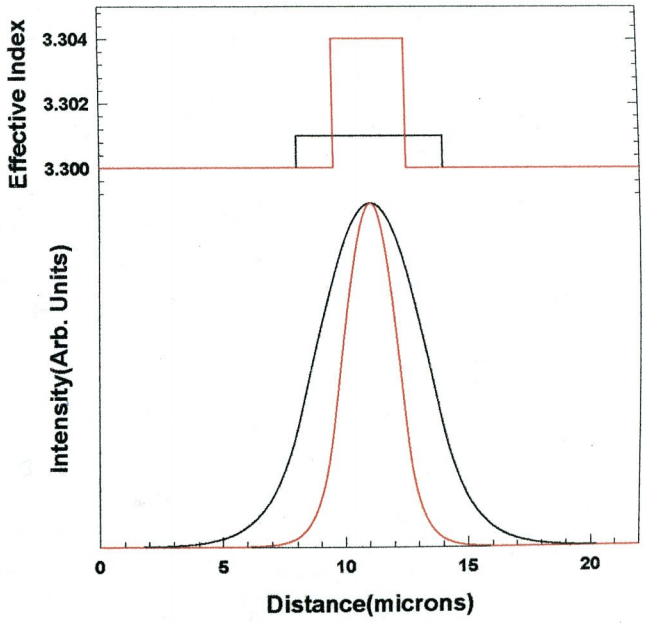

Figure 2-20 Intensity profile of the fundamental mode of single mode ridge waveguide with effective index step of $3x10^{-3}$ (red), Intensity profile of the fundamental mode of single mode ridge waveguide with effective step of $1x10^{-3}$ (black). The area under black curve is 61% greater than the area under the red curve.

Figure 2.20 shows the only lateral mode supported by a 6μm wide ridge waveguide with an effective index step of 1.0×10^{-3} (black) and the only mode supported by a 3.2μm wide ridge with an effective index of 3×10^{-3} (red). We now examine the lateral distributions of light, which are allowed when two ridge waveguides identical to the 3.2μm waveguide shown in Figure 2.20, are placing on either side of the 6.0μm ridge waveguide also in Figure 2.20. For the purpose of this example the distance between the inner ridge and the two adjacent ridges is set at 2μm. Figure 2.21 shows the lateral effective index profile and the allowed modes of such a structure. It is shown that such a configuration supports three guided modes. The first two are predominately guided by the two outer ridge waveguides, while the highest order mode is predominately guided by the central ridge waveguide. It is noted that this mode does extend to the outer edges of the two outer waveguides.

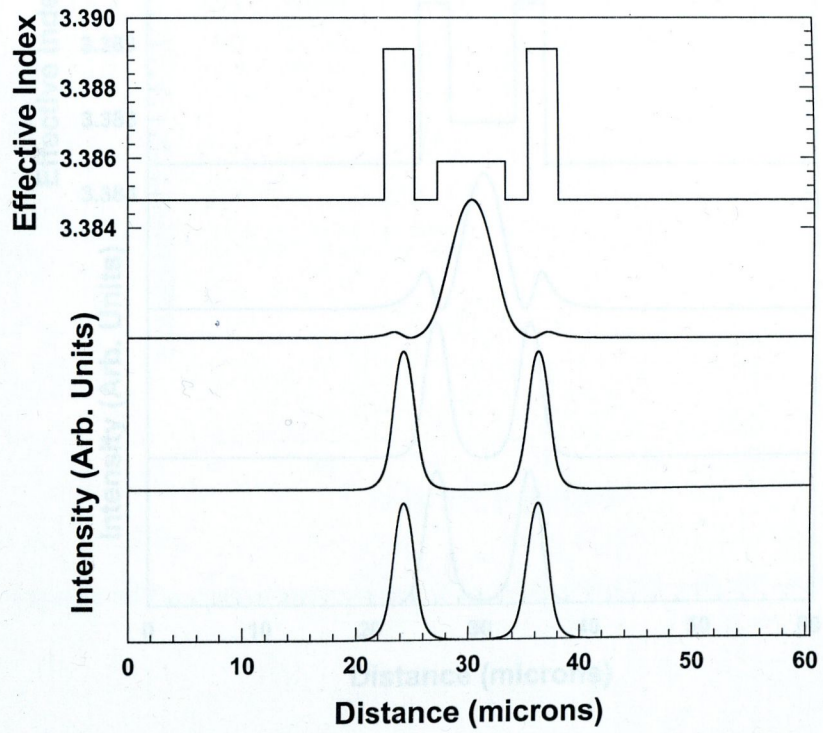

Figure 2-21.Mode structure associated with the effective index profile due to three separate ridge waveguides.

It is now considered what happens in the limit, as the distances between the central and outer ridges are decreased to zero. Figure 2.22 shows the effective index of and the lateral modes supported by such a structure. As in the case of the previous structure, the high index regions almost exclusively guide the first two modes. However although the highest order mode is still predominately guided in the central region of the structure, a far greater fraction of this mode now leaks out into the high index regions. This is a counter intuitive result as the bulk of the optical mode now appears to be guided in a low index region. It is believed that the high index side regions will act to stabilize the mode. It will be demonstrated (Chapter 6) that it is possible to obtain single lateral mode operation from a device incorporating a similar structure. Such a situation can be achieved by selectively pumping the central low index region.

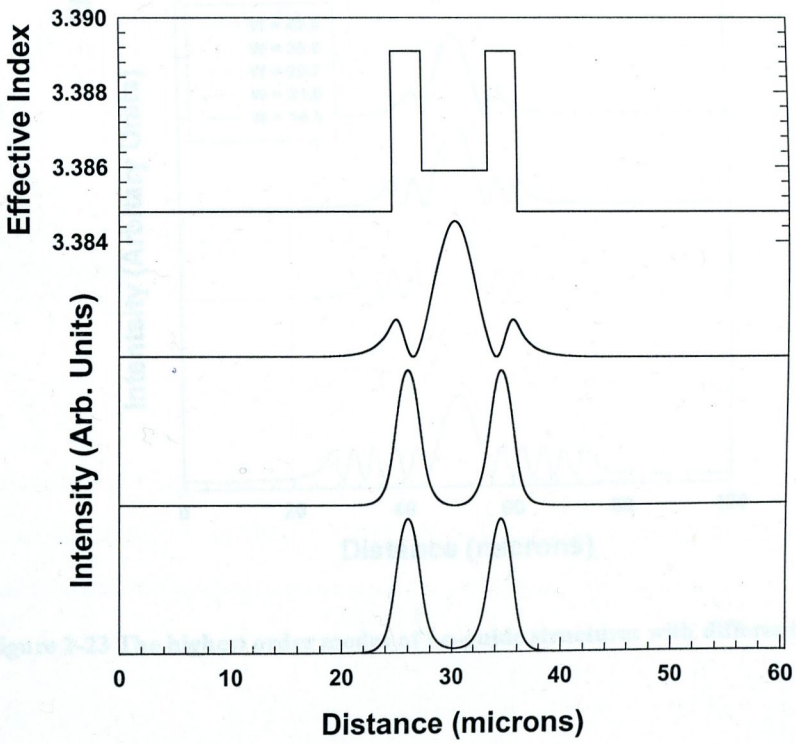

Figure 2-22 Mode structure associated with the effective index profile of a Lo-guide ridge waveguide.

It was also found that it was possible to increase the width of the high index regions in discrete steps, while maintaining the shape of the optical mode in the low index. Figure 2.23 shows how the highest order mode of a Lo-guide structure is affected by increasing the widths of the high index regions. In this example the width of the high index regions are increased in 3.55μm increments. Such a structure offers the possibility of coherent emission from a broad emission aperture

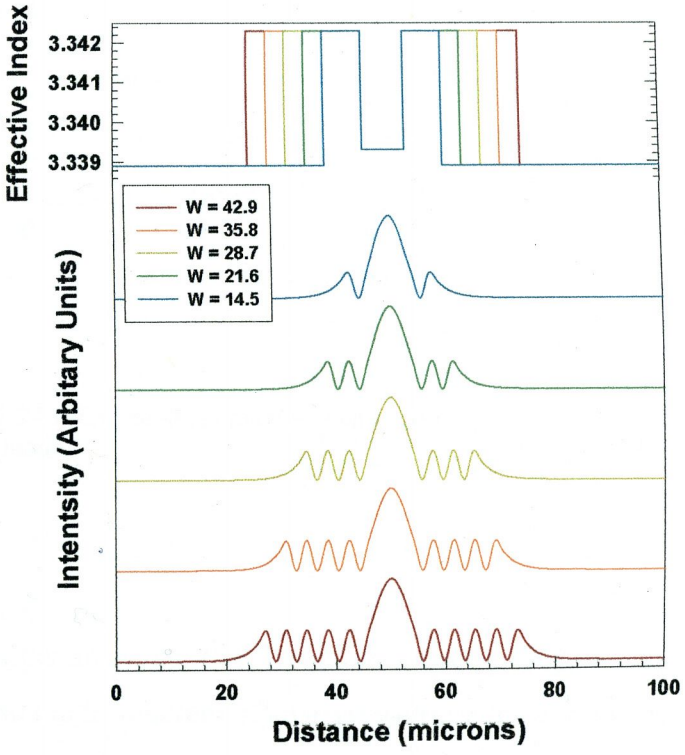

Figure 2-23 The highest order modes of Lo-guide structures with different ridge widths

Another way of achieving coherent emission across a broad aperture design is to couple a number of the structures in Figure 2.22 together. Figure 2.24 shows the effective index profile of such a structure and the intensity profile of its highest order mode.

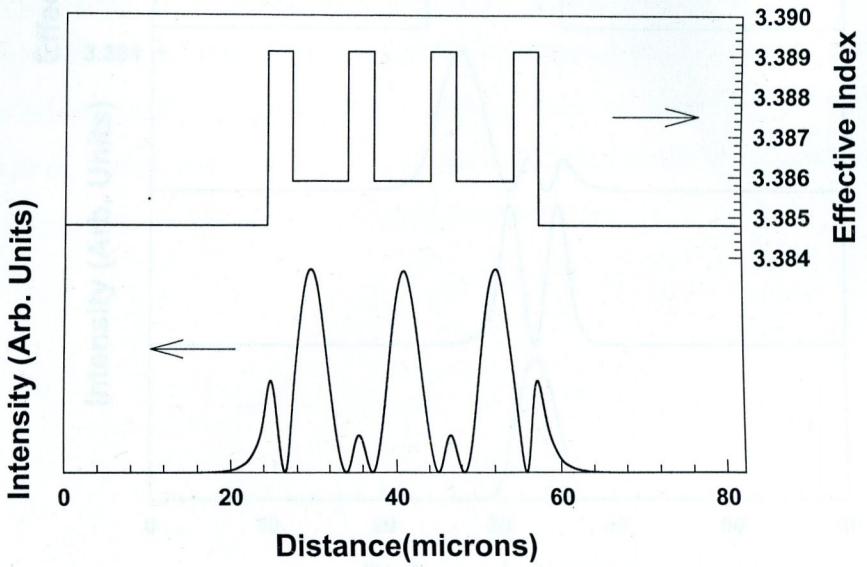

Figure 2-24 Effective index profile of coupled Lo-guide and intensity profile of its highest mode.

Finally we consider an asymmetric Lo-guide structure. Figure 2.25 shows the effective index profile and mode structure of an asymmetric ridge waveguide structure. Chapters 3 & 4 discuss respectively, discuss optically and electrically pumped asymmetric Lo-guide structures, which are implemented in the growth direction.

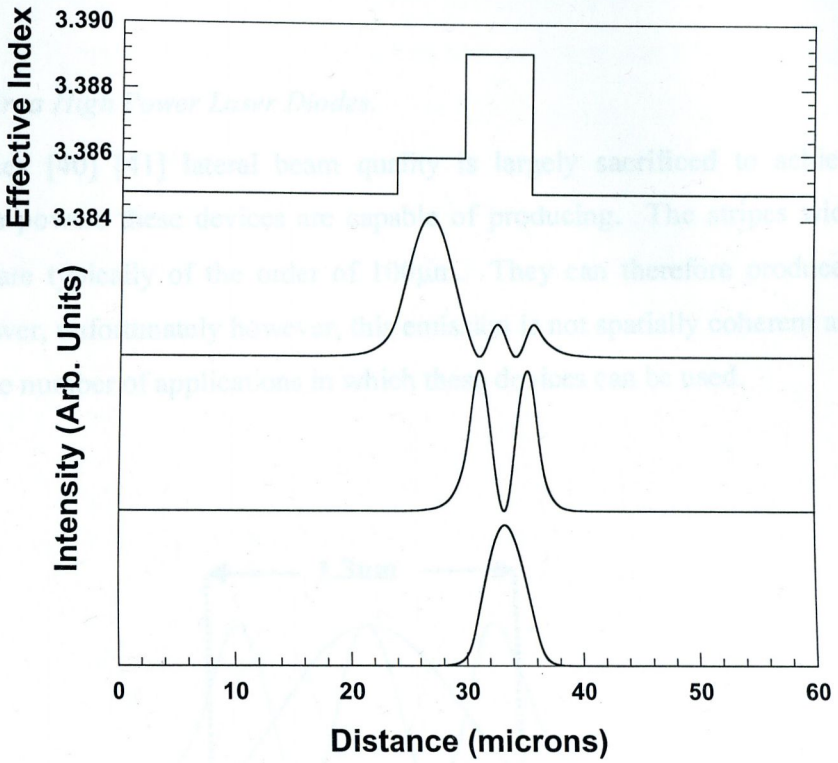

Figure 2-25 Effective index profile of asymmetric Lo-guide structure and intensity profile of its highest mode.

2.11 Review of High Power Structures.

In this section we review some of the existing high power semiconductor laser devices available. In all of the devices, which will be discussed there is a trade off between output power and beam quality. In some devices beam quality is sacrificed in order to obtain extremely high powers, whereas in other devices beam quality cannot be neglected and high power emission must be achieved under a tight set of constraints. Ultimately it is the requirement of the particular application that dictate what type of device will be

used. Below the structure, beam characteristics and intended applications of various high power devices are discussed.

2.11.1 Broad Area High Power Laser Diodes.

In these devices [40] [41] lateral beam quality is largely sacrificed to achieve the extremely high powers these devices are capable of producing. The stripes widths of these devices are typically of the order of 100μm. They can therefore produce large amounts of power, unfortunately however, this emission is not spatially coherent and this fact restricts the number of applications in which these devices can be used.

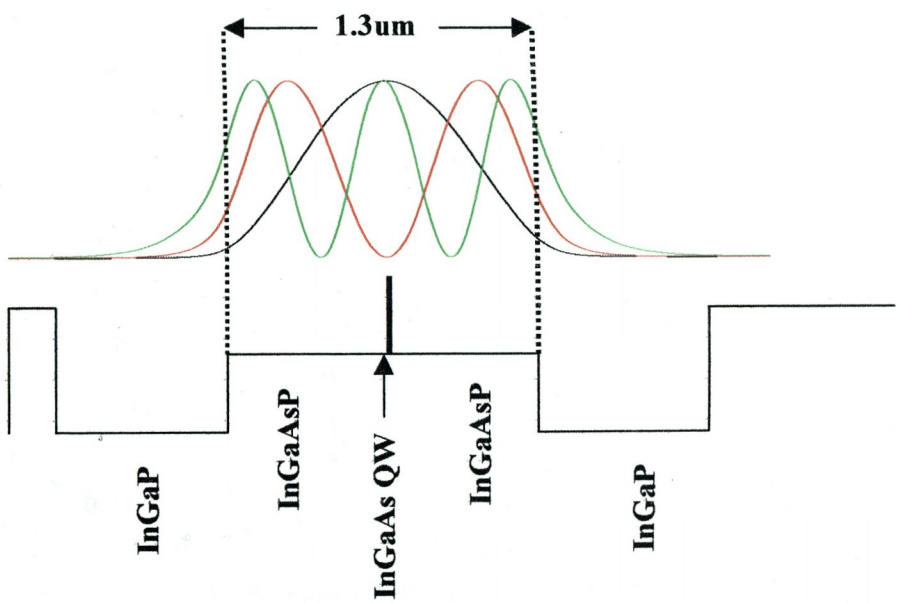

Figure 2-26 Large optical cavity structure as employed in a broad area device.

These devices generally use large optical cavity (LOC) structures [42] to confine light in the transverse direction. LOC structures are basically separate confinement heterostructures, in which the optical waveguide core has been broadened to the extent

that its fundamental mode is almost exclusively guided in the core of the waveguide. If the core of the waveguide is left undoped, devices with very low internal loses can be fabricated. Although such structures typically support three guided modes, lasing action occurs only in the fundamental mode of the structure. The reason for this can be understood by making reference to Figure 2.26. Specifically the 1st order mode (red) has a minimal overlap with the quantum well active region, while the 2nd order mode (green) suffers from free carrier absorption losses in the highly doped cap and substrate layers. The gain threshold necessary to excite the fundemental mode (black) is thus much less than required for the other modes of the structure. These devices generally typically use Al free (InGaP/InGaAsP) material systems, which have better thermal and electrical conductivity than the conventional GaAs/AlGaAs material system.

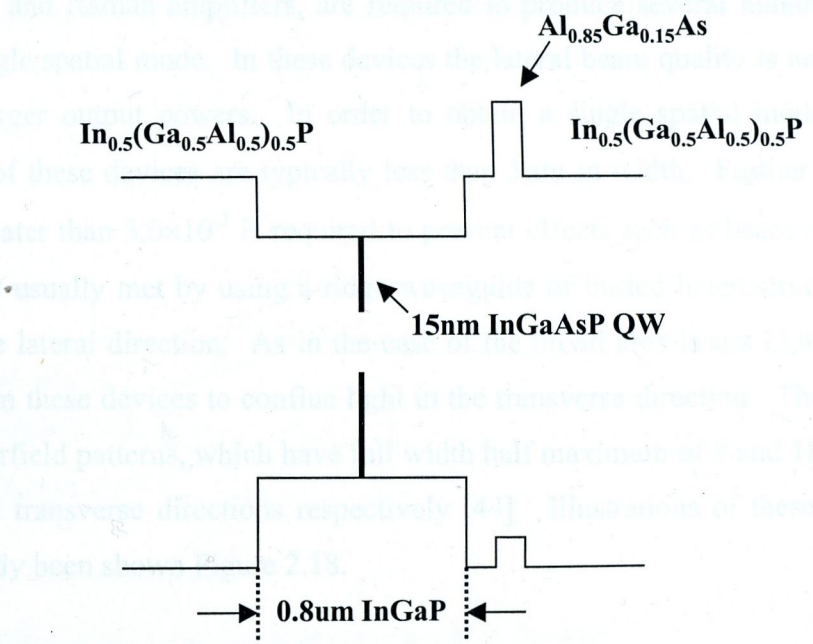

Figure 2-27 AlGaAs layer incorporated in a large optical cavity to prevent carrier leakage.

An interesting design modification to these structures is the inclusion $Al_{0.85}Ga_{0.15}As$ layer in the n-type InGaP cladding layer [43] (Figure 2.27). Due to band offset considerations this layer serves to prevent carriers leaking out of the active region, without having a large effect on the series resistance of the device. The effect of this electron stoping layer is to lessen the effect of temperature on the threshold current. In these devices the Full Width Half Maximum (FWHM) of the farfield pattern in the transverse direction can be as low as 18 degrees. While output of powers up to 10 Watts continuous wave (CW) have been obtained, applications for these devices include the pumping of solid state lasers.

2.11.2 Single Mode High Power Laser Diodes.

We now move from one extreme to the other. Pump lasers such as those commonly used in EDFAs and Raman amplifiers, are required to produce several hundred milli-Watts from a single spatial mode. In these devices the lateral beam quality is not comprised to achieve larger output powers. In order to obtain a single spatial mode the emission apertures of these devices are typically less than 3μm in width. Further a lateral index step of greater than 3.0×10^{-3} is required to prevent effects such as beam steering. These criteria are usually met by using a ridge waveguide or buried heterostructure to confine light in the lateral direction. As in the case of the broad area lasers LOC structures are also used in these devices to confine light in the transverse direction. These devices can produce farfield patterns, which have full width half maximum of 8 and 18 degrees in the lateral and transverse directions respectively [44]. Illustrations of these types of laser have already been shown Figure 2.18.

2.11.3 High Brightness Structures.

Some applications require more power than can be obtained from narrow stripe lasers, yet also require the emission to be coherent. In short what these applications require is high brightness emission. The brightness [45] of a source, B, is given by,

$$B = P / A\Omega$$

where, P, is the optical output power, A is the area of the emission aperture and, Ω, is the solid into which power is emitted. So to achieve high brightness the emission from a device one of the requirements is that emission must be diffraction limited. In the following subsection we review two devices, which produce coherent emission from broad area apertures.

2.11.3.1 Master Oscillator Power Amplifiers (MOPA's)

MOPAs typically consist of a narrow stripe laser coupled into a tapered amplifier. The structure of such devices is illustrated in Figure 2.28. The epitaxial structure of these devices is similar to that of a conventional laser structure.

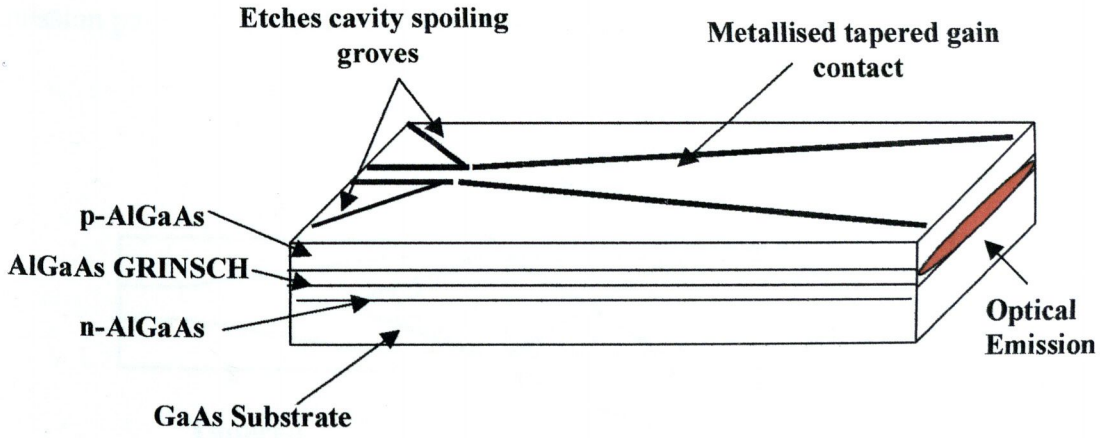

Figure 2- 28 Master oscillator power amplifier structure.

The purpose of the cavity spoiling groves is to deflect unwanted scattered light away from the tapered region and the substrate. These groves are etched trenches down through the active region and are angled with respect to both the symmetry axis of the

taper and the plane of the active region. These groves prevent the oscillation of unwanted Fabry-Perot modes. The operation of these devices is easy enough to understand, the emission from the narrow stripe laser experiences diffraction on leaving this section of the device, the beam then expands to fill the angle defined by the taper. Assuming the tapered region is pumped with a uniform current density, the local gain at a particular point under the taper will be inversely proportional to the power density at that point. Therefore an input Gaussian beam profile in the lateral direction will become more and more uniform as it travels along the taper, eventually approaching a top hat distribution. This happens because the gain saturates along the axis of taper first, due to the larger initial intensity in the center of the beam. For a more detailed explanation of the operation of these devices the interested reader is referred to a review paper by Walpole [44]. As the emission from these devices is coherent, it can by focused down to a small spot. This means the output power from these devices can be efficiently coupled into optical fibres [46] [47], which in turn means they can be used as pump lasers for fibre amplifiers. Figure 2.29 shows optics necessary to efficiently couple light from MOPA structures into an optical fibre. To date output powers up to several Watts [48] [49] have obtained from these devices. The main drawback with regard to these devices is that the emission pattern is dependant on the injection current level.

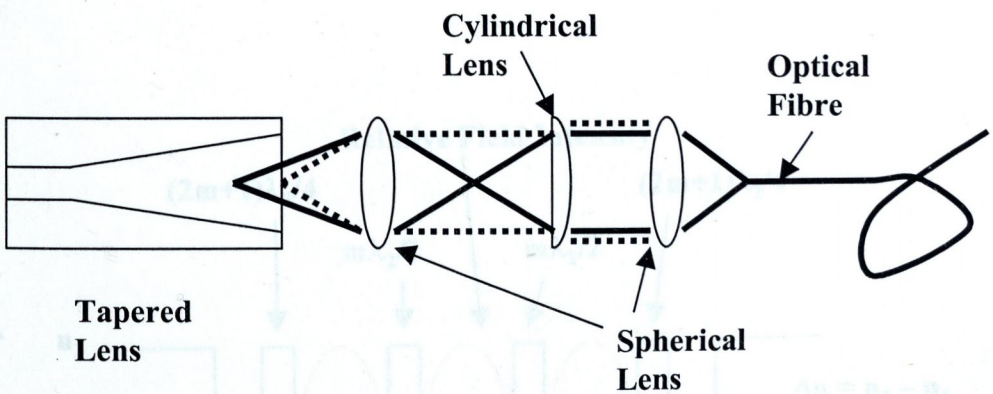

Figure 2-29 Optical setup required to efficiently couple light from a MOPA structure into a single mode fibre

2.11.3.2 Anti-Resonant Reflecting Optical Waveguide (ARROW) Structures.

The development of the resonant optical waveguide (ROW) [50] had a profound impact in the field of anti-guided laser arrays. Figure 2.30 shows the lateral refractive profile of a, so-called, three core ARROW structure [51]. The resonance conditions for this structure are given in terms of, λ_2, and, λ_1, which are respectively the laterally projected wavelengths in the inter-element regions and the antiguided cores. Equations 2.77 and 2.78 gives expressions for λ_2, and, λ_1.

$$\lambda_2 = \lambda / \sqrt{n_2^2 - n_{eff}^2} \qquad 2.77$$

$$\lambda_1 = \lambda / \sqrt{n_1^2 - n_{eff}^2} \qquad 2.78$$

This structure is quite similar to the coupled Lo-guide structure introduced in Section 2.22. In this figure an attempt is made to show the field intensity in the ARROW structure, it is noted that this is not a calculated intensity profile. What differentiates the Lo-guide structure and the ARROW structure, is that the highest order mode in the Lo-guide structure is guided, whereas the mode of interest in the ARROW structure is a radiation, or anti-guided mode.

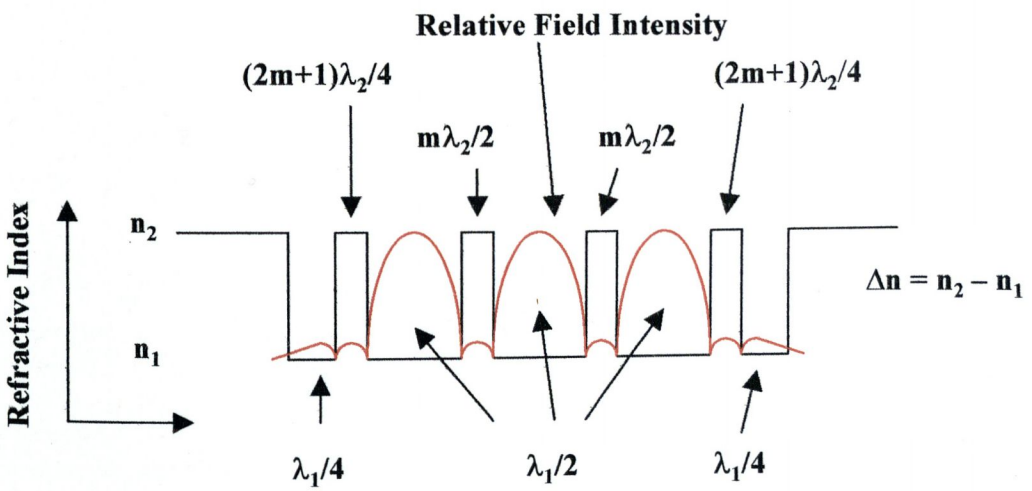

Figure 2-30 Effective index profile and fundamental in phase mode of a three core ARROW structure.

The main drawback with regard to ARROW structures is there small tolerance to fabrication errors, which makes them inherently difficult to manufacture.

2.12 Summary.

To conclude, in this chapter much of the basic theory relating to laser diode devices and semiconductor physics has been presented. Also the Lo-guide concept, the investigation of which is the main subject of this thesis, has been introduced. Also of some the existing high power structures that are available were reviewed. In subsequent chapters the characteristics of active and passive Lo-guide structures are investigated. Further we will conclusively demonstrate Lo-guide type devices, which lase in their highest order modes.

2.13 References

1 John Wilson and John Hawkes. *Optoelectronics: An Introduction*. Prentice Hall. Pages Chapter 5.

2 John Gowar. *Optical Communications Systems, second edition*. Prentice Hall. Pages 357-361

3 G.P. Agrawal and N.K. Dutta. *Long Wavelength Semiconductors Lasers*. Van Nostrand Reinhold Company Inc. Page 29.

4 Mitsuo Fukuda. *Optical semiconductor Devices*. Wiley Series in Microwave and Optical Engineering. Chapter 1

5 P.T. Landsberg. *Recombination in Semiconductors*. Cambridge 1991. Chapter 5

6 L. A. Coldren and S. W. Corzine. *Diode lasers and photonic integrated circuits.* Microwave and optical engineering. Wiley, 1995 Page 154

7 C. Kittle. *Introduction to Solid State Physics Sixth Edition*. Wiley. Chapter 8

8 H. Kressel and M. Ettenberg. *Handbook of Laser Science and Technology*. Wiley. Section 2.2, Semiconductors Lasers.

9 H.C. Casey, Jr. and M.B. Panish. Heterostructure Lasers Part B. Materials and Operating Characteristics. Academic Press 1978. Chapter 5

10 C. Kittle. *Introduction to Solid State Physics Sixth Edition*. Wiley. Page 163

11 P. S. Zory Jr. (Editor) *Quantum Well Lasers*. Academic Press 1993.

12 C. Weisbuch and B. Vinter. *Quantum Semiconductor Structures; Fundamentals and Applications.* Academic Press 1991. Chapter 2.

13 G. Burns. *Solid State Physics*. International Press, 1985. Page 309.

14 L. A. Coldren and S. W. Corzine. *Diode lasers and photonic integrated circuits.* Microwave and optical engineering. Wiley, 1995. Page 11

15 N. Chand, S. N. G. Chu, N. K. Dutta, J. lopata, M. Geva, A. V. Syrbu, A. Z. Mereutza, and V. P. Yakolev. Growth and fabrication of high-performance 980-nm strained InGaAs quantum-well laser for erbium-doped fiber amplitifiers. *IEEE J. Quantum Electron.,* QE-30(2):424-440, February 1994.

16 H. Asonen, A. Ovtchinnikov, G. Zhang, J. Nappi, P. Savolainen, and M. Pessa. Aluminum-Free 980-nm GaInAs/GaInAsP/GaInP Pump lasers. *IEEE J. Quantum Electron.*, QE-30(2): 415-423, February 1994.

17 D. Garbuzov, R. Menna, A. komissarov, M. Maiorov, V. Khalfin, A. Tesoun, S.Todorov and J. Connolly. 1400-1480nm Ridge Waveguide Pump Lasers with 1Watt CW Output for EDFA and Raman Amplification. *Proc. OFC.* pp WC2-1 to WC2-3. 2001

18 C. Zah, R. Bhat, B.N. Pathak, F. Favire, W. Lin, M.C. Wang, N.C. Andreadakis, D.M. Hwang, M.A. Koza, T. Lee, Z Wang, D. Darby, D. Flanders and J.J. Heish. High Performance Uncooled 1.3μm $Al_xGa_yAs_{1-x-y}P$/InP Strained Layer Quantum well Lasers for Subscriber Loop Applications. *IEEE J. Quantum Electron.,* QE-30(2): 511-522, February 1994

19 H.D. Summers, C.H. Molloy, P.m. Smowton, P. Rees, I. Pierce, and D.R. Jones. Experimental Analysis of Self Pulsation in 650nm Wavelength AlGaInP Laser Diodes with Epitaxial Absoring Layers. *IEEE Journal of Selected Topics in Quantum Electron,* 5(3): 745-749, May/June 1999

20 N. Peyghambarian, S.W. Kock and A. Mysyrowicz. *Introduction to Semiconductor Optics.* Printice Hall 1993. Chapter 8.

21 E. Yablonovitch and E.O. Kane. Reduction of Lasing Threshold Current Density by the Lowering of the Valence Band Effective Mass. *J. Lightwave Technol.,* LT-4, no. 5, pp. 504-506. May 1986.

22 P.J.A. Thijs, L.F. Tiemeijer, P.I. Kuindersma, J.J.M. Binsma, and T.V. Dongen. High Performance 1.5μm Wavelength InGaAs-InGaAsP Strained Quantum Well Laser and Amplifiers. *IEEE J. Quantum Electron.,* QE-27(6): 1426-1438, June 1991

23 L.F. Tiemeijer, P.J.A. Thijs, P.J. de Waard, J.J.M. Binsma, and T.V. Dongen. Dependence of polarization, gain, linewidth enhancement factor and K factor on the sign of the strain of InGaAs/InP strained layer multiquantum well lasers. *Appl. Phys. Lett.,* 58(24), pp 2738-2740, June 1991.

24 L. A. Coldren and S. W. Corzine. *Diode lasers and photonic integrated circuits.* Microwave and optical engineering. Wiley, 1995. Page 124.

25 P.T. Landsberg. *Recombination in Semiconductors.* Cambridge 1991. Section 7.3.2

26 L. A. Coldren and S. W. Corzine. *Diode lasers and photonic integrated circuits.* Microwave and optical engineering. Wiley, 1995. Section 4.3.1.

27 John Gowar. *Optical Communications Systems, second edition.* Prentice Hall. Pages Section 2.5

28 D.E. Bourne and P.C. Kendall. Vector Analysis and Cartesian Tensors, 3rd Edition. Chapman and Hall 1992. Section 4.8.

29 D. Marcuse. Solution of the Vector Wave Equation for General Dielectric Waveguides by the Galerkin Method. *IEEE J. Quantum Electron.*, QE-28(2): 459-465, February 1992

30 C.H. Henry, and, R.H. Verbeek. Solution of the scalar wave Equation for Arbitrarily Shaped Dielectric Waveguides by Two Dimensional Fourier Analysis. *J. Lightwave Technol.*, 7(2), pp. 308-313. February 1989.

31 John Gowar. *Optical Communications Systems, second edition*. Prentice Hall. Appendix 2.

32 G.P. Agrawal and N.K. Dutta. *Long Wavelength Semiconductors Lasers*. Van Nostrand Reinhold Company Inc. Chapter 2

33 Erwin Kreyseig. *Advanced engineering mathematics, Seventh edition*. pages, Wiley 1993. Section 2.2.

34 M. Mounowitz and D.J. Vezzetti. Mode Structure and Lateral Confinement in Strip Loaded Optical Waveguides: Effect. *J. Lightwave Technol.*, 10(4), pp. 426-431. February 1989.

35 L. A. Coldren and S. W. Corzine. *Diode lasers and photonic integrated circuits.* Microwave and optical engineering. Wiley, 1995. Section 1.7

36 Mitsuo Fukuda. *Reliability and Degradation of Semiconductor Lasers and LEDs* Artech House 1991. Section 4.3

37 J.K. Wade, L.J. Mawst, D. Botez, R.F. Nabiev, M. Jansen, and J.A. Morris. 6.1W continuous wave front facet power from from Al-free active region (λ=805nm) diodes lasers. *Appl. Phys. Lett.*, 72(1) pp 4-6, January 1998

38 Mitsuo Fukuda. *Optical semiconductor Devices*. Wiley Series in Microwave and Optical Engineering. Section 3.2.4

39 S. G. Krivoshlykov. Compound Waveguide Lasers and Optical Parametric Oscillators. *United States Patent*. Pat No. 5,574,818.

40 L.J. Mawst, A. Bhattacharya, J. Lopez, D. Botez, D.Z. Garbuzov, L. DeMarco, J.C. Connolly, M. Jansen, F. Fang, and R.F. Nabiev. 8W continous wave front-facet power from broad-waveguide Al-free 980nm diode lasers. *Appl. Phys. Lett.*, 69(11): 1532-1534, September 1996.

41 S. O'Brien, H. Zhao, A. Schoenfelder and R.J. Lang. 9.3W CW (In)AlGaAs 100um wide lasers at 970nm. *Electron. Lett.*, 33(22):1869-1870, October 1997

42 A. Al-Mulhanna, L.J. Mawst, D. Botez, D. Z. Garbuzov, R. U. Martinelli and J. C. Connolly. High-power (>10W) continous-wave operation from 100-um-apetature 0.97-um-eitting Al-free diode lasers. *Appl. Phys. Lett.*, 73(9): 1182-1184, August 1998.

43 A. Al-Muhanna, J. K. Wade, T. Earles, J. Lopez and L. J. Mawst. High-performance, reliable, 730-nm-emitting Al-free active region diode lasers, *Appl. Phys. Lett.*, 73(20): 2869-2871, November 1998.

44 B. Schmidt, S. Pawlik, B. Mayer, S.Mohrddiek, I. Jung, B. Sverdlov, N. Lichtenstein, N. Matuschek, and C. Harder. Highly efficient 980nm single mode modules with over 0.5 Watt pump power. *Proc. OFC.* pp WC1-1 to WC1-3 2001

45 J.N. Walpole. Semiconductor amplifiers and lasers with tapered gain regions. *Optical and Quantum Electronics*, 28: 623-645, 1996

46 J.C. Livas, S.R. Chinn, E.S. Kintzer, J.N. Walpole, C.A. Wang, and L.J. Missaggia. Single Mode Optical Fibre Coupling of Tapered Gain Region Devices. *IEEE Photon. Technol. Lett.*, 6(3):422-424, March 1994

47 J.C. Livas, S.R. Chinn, E.S. Kintzer, J.N. Walpole, C.A. Wang, and L.J. Missaggia. High Power Erbium Doped Fibre Amplifier with 975nm Tapered Gain Region Pumps. *Electron. Lett.,* 1994, 30, pp. 1054-1055.

48 R. Parke, D. F. Welch, A. Hardy, R. Lang, D. Mehuys, S. O'Brien, K. Dzurko, and D. Scifries. 2.0W CW, Diffraction-Limited operation of a monolithically integrated master oscillator power amplitifier. *IEEE Photon. Technol. Lett.*, 5(3):297-300, March 1993.

49 S. O'Brien, R. Lang, R. Parke, J. Major, D.F. Welch, and D. Mehuys. 2.2W Continous wave diffraction limited monolithically integration master oscillator power amplifier at 854nm. *IEEE Photon. Technol. Lett.*, 9(4):440-442, March 1993.

50 D. Botez, L.J. Mawst, G.L. Peterson, and T.J. Roth. Phase Locked Arrays of Antiguides: Modal Content and Discrimination. *IEEE J. Quantum Electron.,* QE-26(3): 482-495, March 1990

51 C. Zmudzinski, D. Botez, L.J. Mawst, A. Bhattacharya, M. Nesnidal, and R.F. Nabiev. Three Core ARROW Type Diode Laser: Novel High Power, Single Mode Device, Effective Master Oscillator for Antiguided MOPA's

Chapter 3

Waveguide Design and Analysis.

3.1 Introduction.

This chapter details the numerical and experimental analysis, which was carried out on conventional waveguide designs and novel waveguides designs of the type discussed in section 2.10. Here we detail the procedure for designing such structures, this includes a description of a numerical method for calculating the modal solutions of arbitrarily shaped waveguides. The epitaxial structures of the samples, which were grown in order to experimentally verify the novel waveguide concept are also presented here. The results of transmission measurements made on both conventional and novel passive waveguides are then detailed, and comparisons are made between theory and experiment. Finally we show the results obtained by optically pumping novel waveguide structures, which contained five $In_{0.20}Ga_{0.80}As$ quantum wells. These results conclusively demonstrate a Lo-guide type device lasing in one of its highest order modes.

3.2 Waveguide Design Procedure

In passive waveguides it is the refractive index step between the core and cladding layers, the core thickness, and the wavelength of light being guided, which determine the number and shape of the allowed guided modes. To design an optical waveguide in a material system such as $Al_xGa_{1-x}As$ [1] it is necessary to have two things. Firstly a method of calculating the refractive index of, $Al_xGa_{1-x}As$, at a specified wavelength and containing a

particular mole fraction of aluminum. Secondly a method for finding the guided mode solutions of arbitrarily shaped dielectric waveguides

3.2.1 The Refractive Index of III-V Semiconductor Alloy Systems

A semi-empirical approach for calculating the refractive indices of $Al_xGa_{1-x}As$ compounds is adopted here. The dielectric constant for a given material at a specific angular frequency, ω, can be written in terms of its real and imaginary components as follows

$$\varepsilon(\omega) = \varepsilon_1(\omega) + i\varepsilon_2(\omega) \qquad 3.1$$

The Kramers-Kronig relations [2], relate the real and imaginary parts of the dielectric constant:

$$\varepsilon_1(\omega) = 1 + \frac{2}{\pi}\mathscr{P}\int_0^\infty \frac{\omega'\varepsilon_2(\omega')}{(\omega')^2 - \omega^2}d\omega' \qquad 3.2$$

$$\varepsilon_2(\omega) = \frac{2\omega}{\pi}\mathscr{P}\int_0^\infty \frac{\varepsilon_1(\omega')}{\omega^2 - \omega'^2}d\omega' \qquad 3.3$$

where $\mathscr{P}$ stands for the Cauchy principle value of the integral. In this case the singularity at $\omega = \omega'$ is excluded from the integration. These relationships allow ε_1 to be calculated if ε_2 is known and vice versa. In a semiconductor material the real component of the dielectric constant can be written as:

$$\varepsilon_1(\omega) = \varepsilon_1^{F(\mathscr{E}_0,\mathscr{E}_0+\Delta)}(\omega) + \varepsilon_1^D(\omega) + \varepsilon_1^C(\omega) + \varepsilon_{1\infty} \qquad 3.4$$

Where $\varepsilon_1^{F(\mathscr{E}_0,\mathscr{E}_0+\Delta)}(\omega)$ is the free electron-hole contribution to the permittivity arising from the $\mathscr{E}_0$ and $\mathscr{E}_0+\Delta_0$ energy gaps (Figure 3.1), $\varepsilon_1^D(\omega)$ and $\varepsilon_1^C(\omega)$ are contributions due to

discrete and continuum exciton states, and $\varepsilon_{1\infty}$ is the background dielectric constant arising from higher lying energy gap transitions such as $\mathscr{E}_1$, $\mathscr{E}_1+\Delta_1$ and $\mathscr{E}_2$. The approach [3] used here to calculate $\varepsilon_1(\omega)$ considers only the contributions from free electron hole pairs as the contributions from excitionic states are very small compared with $\varepsilon_1^{F(\mathscr{E}_0,\mathscr{E}_0+\Delta_0)}(\omega)$. This is because at room temperature, the binding energies of excitions in most semiconductor compounds are small compared to the value of k_BT. The contribution of the lowest direct gap transition $\mathscr{E}_0$ to $\varepsilon_2(\omega)$ is given by

$$\varepsilon_2^{F(\mathscr{E}_0)}(\omega) = A\frac{1}{(\hbar\omega)^2}(\hbar\omega-\mathscr{E}_0)^{\frac{1}{2}}, \qquad \hbar\omega \geq \mathscr{E}_0, \tag{3.5}$$

where the parameter A, is dependant on the composition of the ternary system.

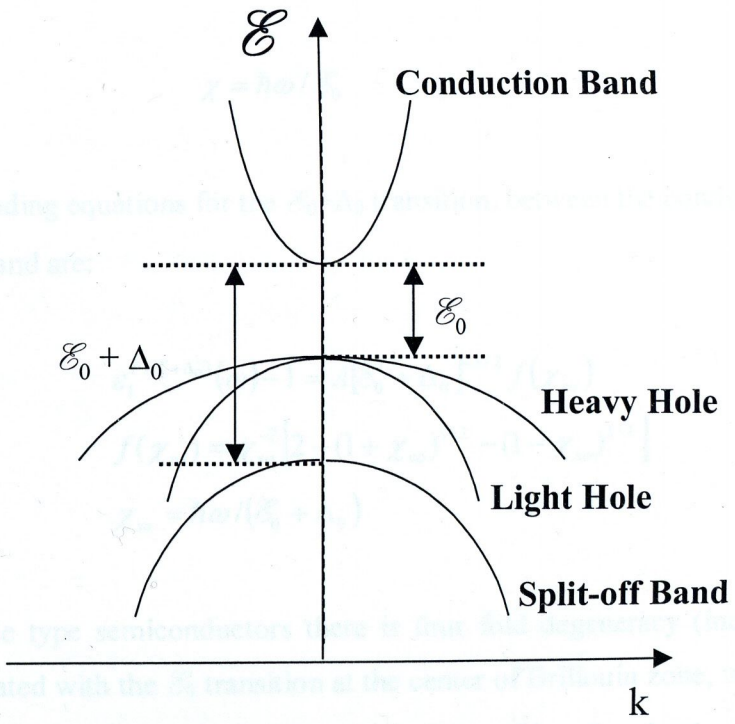

Figure 3-1 $\mathscr{E}_0$ and $\mathscr{E}_0+\Delta_0$ electronic transitions

In Equation 3.5, the value of $\varepsilon_2^{F(\mathscr{E}_0)}(\omega)$ is governed by the square root of the difference between photon energy and $\mathscr{E}_0$, this is expected since the absorption spectrum of a material should be the same shape as its density of states function. It has been previously shown (Section 2.6.4) that the density of states function in a bulk semiconductor crystal also increases in proportion with $\mathscr{E}^{1/2}$, for $\mathscr{E} \geq \mathscr{E}_g$. The Kramers-Kronig transformation of Equation 3.5 results in the following contribution to the real part of the dielectric constant.

$$\varepsilon_1^{F(\mathscr{E}_0)}(\omega) - 1 = A\mathscr{E}_0^{-3/2} f(\chi) \qquad 3.6$$

where

$$f(\chi) = \chi^{-2}\left[2 - (1+\chi)^{1/2} - (1-\chi)^{1/2}\right] \qquad 3.7$$

and

$$\chi = \hbar\omega / \mathscr{E}_0 \qquad 3.8$$

The corresponding equations for the $\mathscr{E}_0+\Delta_0$ transition, between the conduction band and the split-off band are:

$$\varepsilon_1^{F(\mathscr{E}_0+\Delta_0)}(\omega) - 1 = A\left[\mathscr{E}_0 + \Delta_0\right]^{-3/2} f(\chi_{so}) \qquad 3.9$$

$$f(\chi_{so}) = \chi_{so}^{-2}\left[2 - (1+\chi_{so})^{1/2} - (1-\chi_{so})^{1/2}\right] \qquad 3.10$$

$$\chi_{so} = \hbar\omega / (\mathscr{E}_0 + \Delta_0) \qquad 3.11$$

In zinc blende type semiconductors there is four fold degeneracy (including both spin states) associated with the $\mathscr{E}_0$ transition at the center of Brillouin zone, while there is only two fold degeneracy associated the $\mathscr{E}_0+\Delta_0$ transition. Therefore in zinc blende materials, $\varepsilon_1(\omega)$, can be written as:

$$\varepsilon_1(\omega) = A\left\{f(\chi) + \frac{1}{2}\left[\mathscr{E}_0(\mathscr{E}_0 + \Delta_0)\right]^{3/2} f(\chi_{so})\right\} + B \qquad 3.12$$

Where B includes any contributions from higher lying energy gaps. Like A the parameter **B** is dependant on the composition of the alloy system. Numerical expressions for A and B have previously been found fitting by Equation 3.12 with experimental data [1], these expressions are:

$$A(x) = 6.3 - 19.0x \qquad 3.13$$

$$B(x) = 9.4 - 10.2x \qquad 3.14$$

Using these expressions together with Equation 3.12 the real part of the dielectric constant, $\varepsilon_1(\omega)$, can be found for any composition of $Al_xGa_{1-x}As$, which is lattice matched to GaAs. The real part of the refractive index for these materials is now simply obtained by taking the square root of $\varepsilon_1(\omega)$.

3.2.2 Numerical Solutions of the Wave Equation

Once the refractive indices of the individual layers in a structure are known it is possible to calculate the intensity distribution of its allowed guided modes. In Appendix 1 it is shown that in TE modes, the component of electric field parallel to the plane of a planar waveguide, E_x, must satisfy the equation.

$$\frac{d^2E_x}{dy^2} + k_0^2\left[n(y) - n^2{}_{eff}\right]E_x = 0 \qquad 3.15$$

Where $n(y)$ is the refractive index profile in the transverse direction, k_0 is the wavenumber in free space and n_{eff} is the mode effective index. The effective index of a particular mode given by: $n_{eff} = \beta / k_0$. Solutions of Equation 3.15 can be obtained numerically using a series expansion method [4]. It is well known that any arbitrary function that satisfies certain constraints with regard to continuity and finiteness can be

expressed as a series expansion in terms of a complete set of orthogonal basis functions. Hence the field distribution in the waveguide can be written as a series expansion:

$$E_x(y) = \sum_{n=1}^{N} c_n \sin\left(\frac{\pi}{L} ny\right) \qquad 3.16$$

where, n, is an integer, L, is the length of the computational domain. Substituting this series expansion into Equation 3.15 and using the orthogonality property of the sine function, yields the matrix equation:

$$A_{nm} c_n = \left(n^2(y) - n_{eff}^2\right) c_m \qquad 3.17$$

where A_{nm} is defined as follows

$$A_{nm} = \frac{2}{L_y} \int_0^{L_y} \left[n^2(y) - n_{eff}^2\right] \sin\left(\frac{\pi}{L_y} ny\right) \sin\left(\frac{\pi}{L_y} my\right) dy - \left(\frac{\pi n}{k_o L_y}\right)^2 \delta_{nm} \qquad 3.18$$

Solving this eigenvalue problem yields the effective index n_{eff}, and the expansion coefficients c_n for each allowed optical mode. Substituting the appropriate values of c_n and n_{eff} back into Equation 3.16 yields the electric field distributions for the corresponding modes. However of the N^2 eigenvalues, only very few are of physical significance. Guided modes can be distinguished from radiation modes on the basis that their effective refractive indices will lie between those of the core and cladding layers. The intensity distributions of these modes can be obtained by squaring the corresponding electric field distributions. It is now possible to calculate the fractional overlap of a given mode, with any portion of the waveguide. The fractional overlap of a guided mode with the active region of a laser diode is generally referred to as the confinement factor. Represented by the symbol, Γ_y, the transverse confinement factor of a particular field distribution is given by

$$\Gamma_y = \frac{\int_{active\_region} |\psi(y)|^2 dy}{\int_{-\infty}^{\infty} |\psi(y)|^2 \, dy} \qquad 3.19$$

3.2.3 The Effective Index Method.

As mentioned in Section 2.9.5 ridge waveguide structures are employed in laser diodes to provide optical confinement in the lateral direction. One technique used to analyse the waveguiding properties of devices which incorporate such structures is the effective index method. In this approach the electric field distributions in the lateral and transverse directions are calculated separately. This technique is treated more formally [5] in Appendix 2. However a more complete mathematical analysis of this procedure is given by Buus [6]. Consider the ridge waveguide shown in Figure 3.2(a).

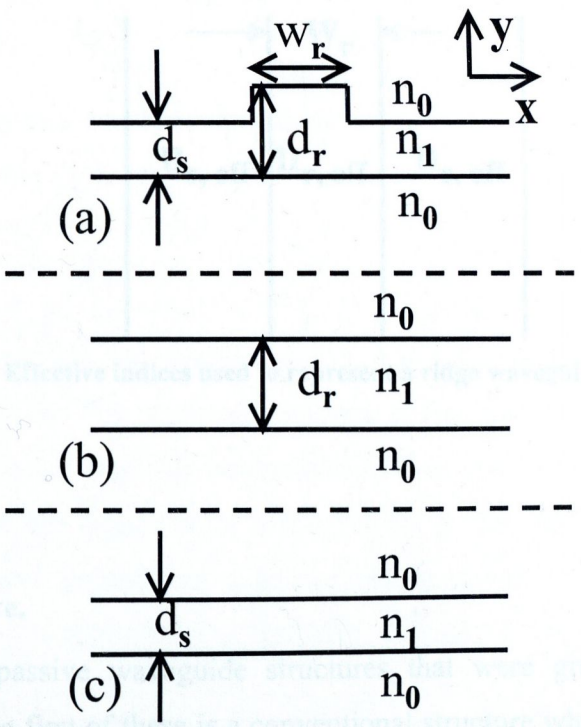

Figure 3-2 A ridge waveguide (a) can be regarded as being made up of one thick (b) and two narrow (c) slab waveguides.

The ridge waveguide can be considered as two separate slab waveguides (Figures 3.2(a) and 3.2(b), a thinner slab of thickness d_s and thicker slab of thickness d_r. Each will support its own guided modes, whose field distributions and propagation constants can be calculated either analytically or numerically. If w_r is large enough, it may be regarded as a slab waveguide, the fundamental mode of this structure has a propagation constant β_r, that defines for it an effective index, $n_{r,eff} = \beta_r / k$. Similarly the fundamental mode of the smaller slab waveguide has a propagation constant β_s, which defines for it an effective index $n_{s,eff}$, given by $n_{s,eff} = \beta_s / k$. We can now regard the original waveguide in Figure 3.2(a) as a composite slab structure consisting of effective refractive index regions as shown in Figure 3.3. The modes of this slab structure can be calculated numerically using the method detailed previously. Hence, a more complicated two dimensional problem has been converted into two simpler one dimensional problems.

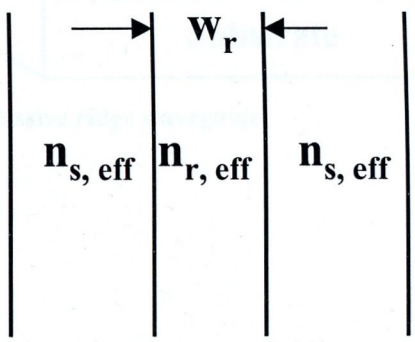

Figure 3-3 Effective indices used to represent a ridge waveguide.

3.3 Sample Structure.

Details of various passive waveguide structures that were grown by MOCVD are presented below. The first of these is a conventional structure while the latter two are of the type discussed in section 2.10. In the ensuing sections the results of transmission measurements made on these samples will be examined. The conventional wavguide

structure (Figure 3.4) consisted of a slab of GaAs (3.0 μm thick) sandwiched between two $Al_{0.3}Ga_{0.7}As$ cladding layers. The difference in refractive index difference between the GaAs core and the cladding layers was approximately 0.165. The upper cladding layer had ridge waveguide structure photolithographically developed upon it. The ridge provided optical confinement in the lateral (perpendicular to growth) direction, while the high index GaAs layer guided light in the transverse (parallel to growth) direction. As stated previously the purpose of performing transmission measurements on these conventional structures was to validate the experimental setup and the numerical model.

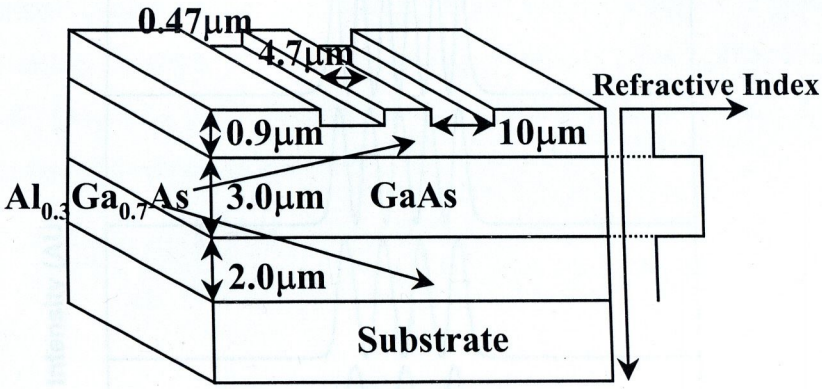

Figure 3-4 Passive ridge waveguide.

The refractive index profile and mode structure of this transverse multimode waveguide are shown in Figure 3.5. This structure supports seven guided modes in all. It can be seen from this Figure 3.5 that the fundamental mode has less of an overlap with the cladding regions than the higher order modes. This means that the fundamental mode will be more efficiently guided and will thus have a lower loss than the higher order modes.

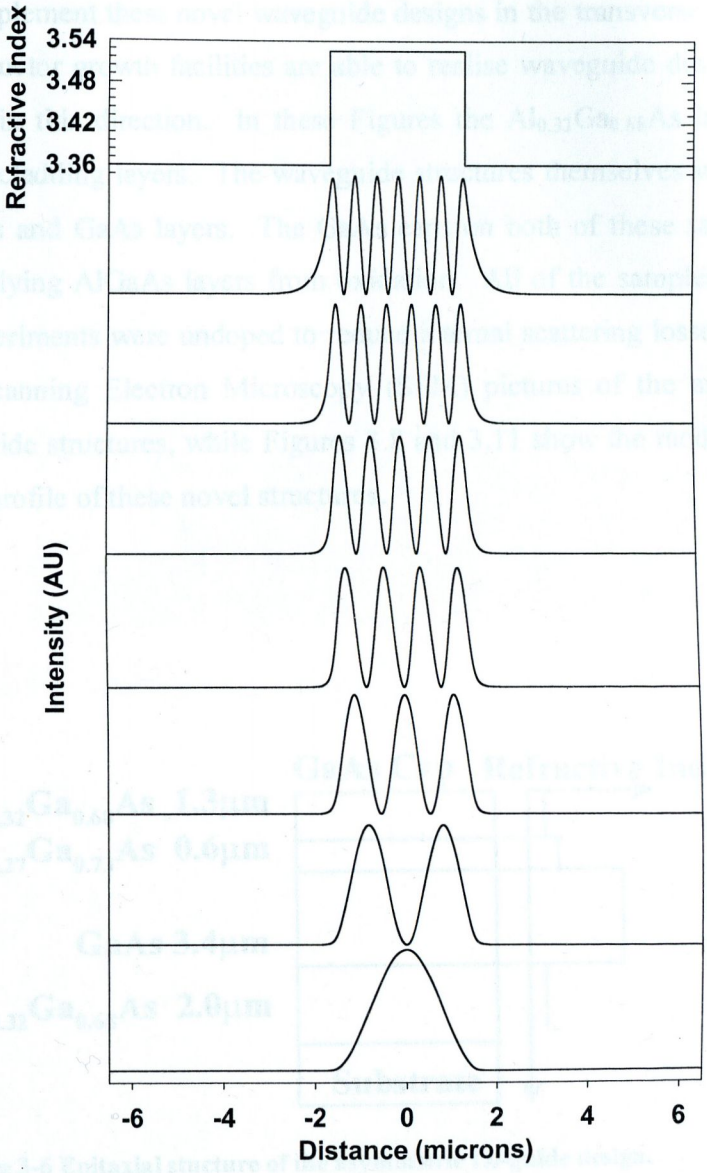

Figure 3-5 Mode Structure of transverse multimode waveguide

Figures 3.6 and 3.9 show the expitaxial structure of the novel compound waveguides. It was chosen to implement these novel waveguide designs in the transverse direction since current semiconductor growth facilities are able to realise waveguide design parameters more accurately in this direction. In these Figures the $Al_{0.32}Ga_{0.68}As$ layers form the upper and lower cladding layers. The waveguide structures themselves were formed by the $Al_{0.28}Ga_{0.72}As$ and GaAs layers. The GaAs caps on both of these samples were to protect the underlying AlGaAs layers from oxidation. All of the samples used in these transmission experiments were undoped to reduce internal scattering losses. Figures 3.7 and 3.10, are Scanning Electron Microscopy (SEM) pictures of the asymmetric and symmetric Lo-guide structures, while Figures 3.8 and 3.11 show the mode structure and refractive index profile of these novel structures.

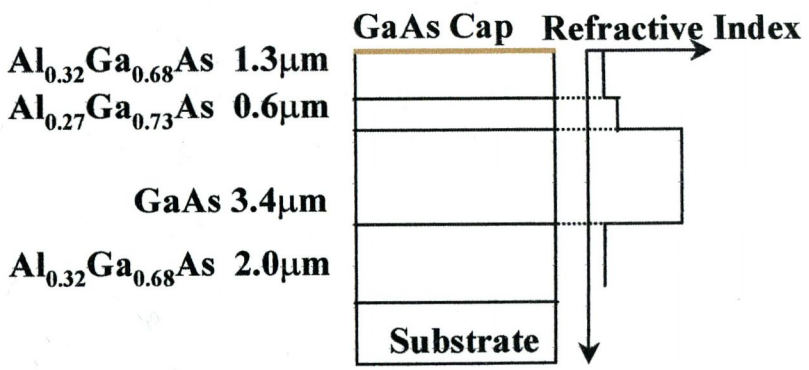

Figure 3-6 Epitaxial stucture of the asymmetric Lo-guide design.

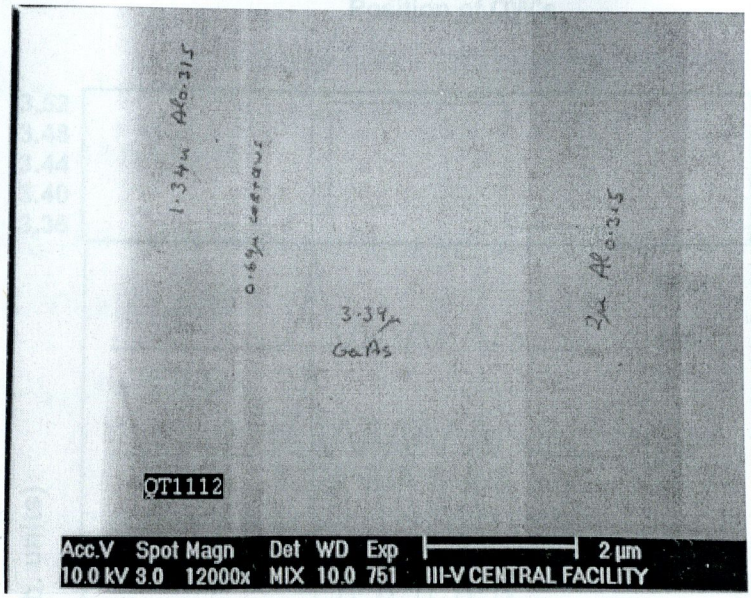

Figure 3-7 SEM picture of the asymmetric Lo-guide design.

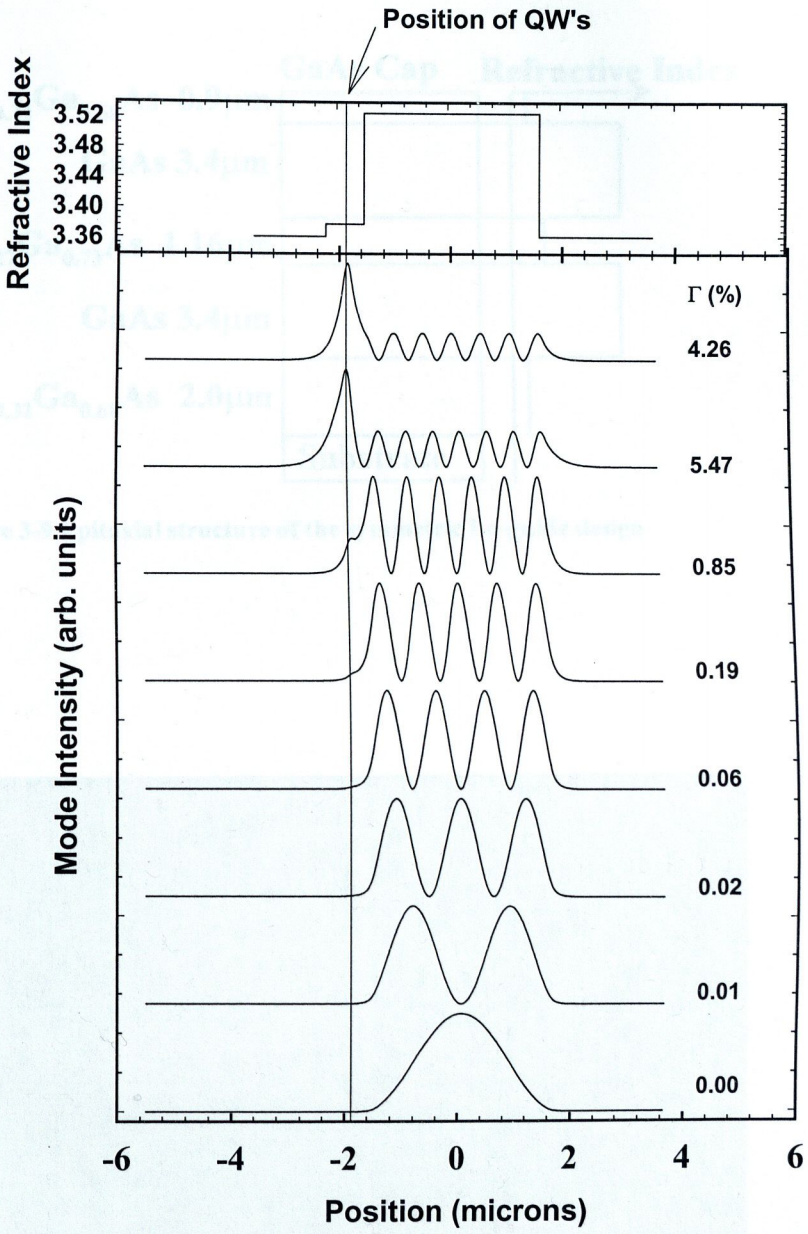

Figure 3-8 Mode structure of the asymmetric Lo-guide design. The quantum wells and confinement factors indicated should be ignored at present, as they relevant to a future discussion

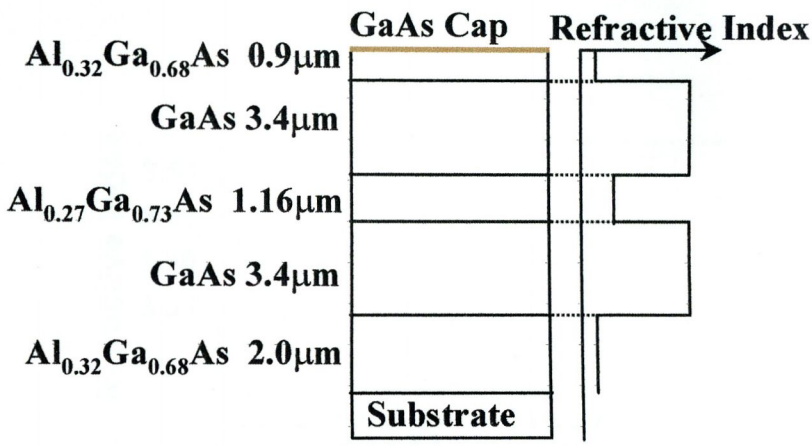

Figure 3-9 Epitaxial structure of the symmetric Lo-guide design

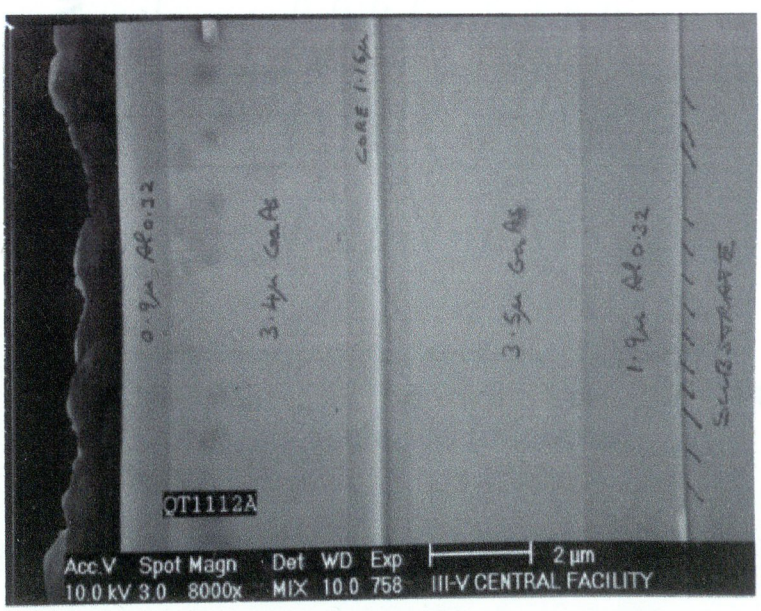

Figure 3-10 SEM picture of the symmetric Lo-guide design

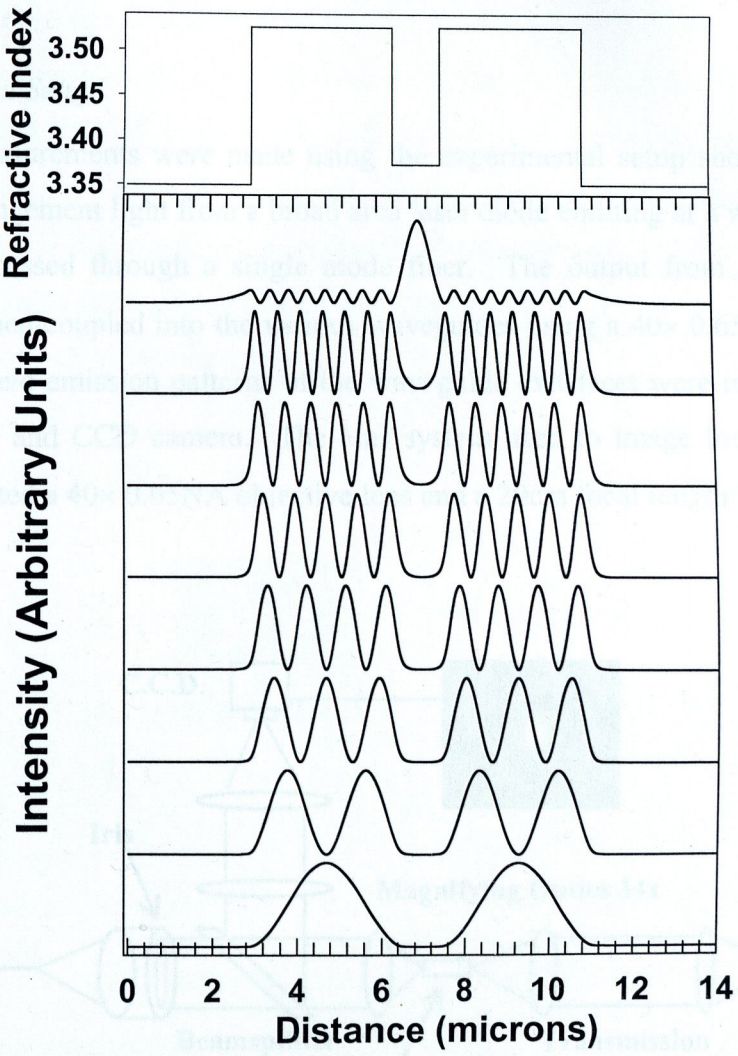

Figure 3-11 Mode structure of the symmetric Lo-guide design.

3.4 Transmission Measurements: Introduction.

The mode structure of the Lo-guide devices was initially assessed by measuring their transmission properties. Firstly however, in order to calibrate our measurement setup, we performed transmission measurements on the conventional semiconductor waveguide structure.

3.4.1 Experimental Setup.

Transmission measurements were made using the experimental setup shown in Figure 3.12. In this arrangement light from a broad area laser diode emitting at a wavelength of, λ=980nm, was passed through a single mode fiber. The output from the fibre was collimated, and then coupled into the various waveguides using a 40× 0.65NA objective lens. The near-field emission patterns of the waveguide exit facet were imaged using a lens relay system and CCD camera. The lens system used to image the facets of the waveguide consisted a 40× 0.65NA objective lens and a 20cm focal length lens.

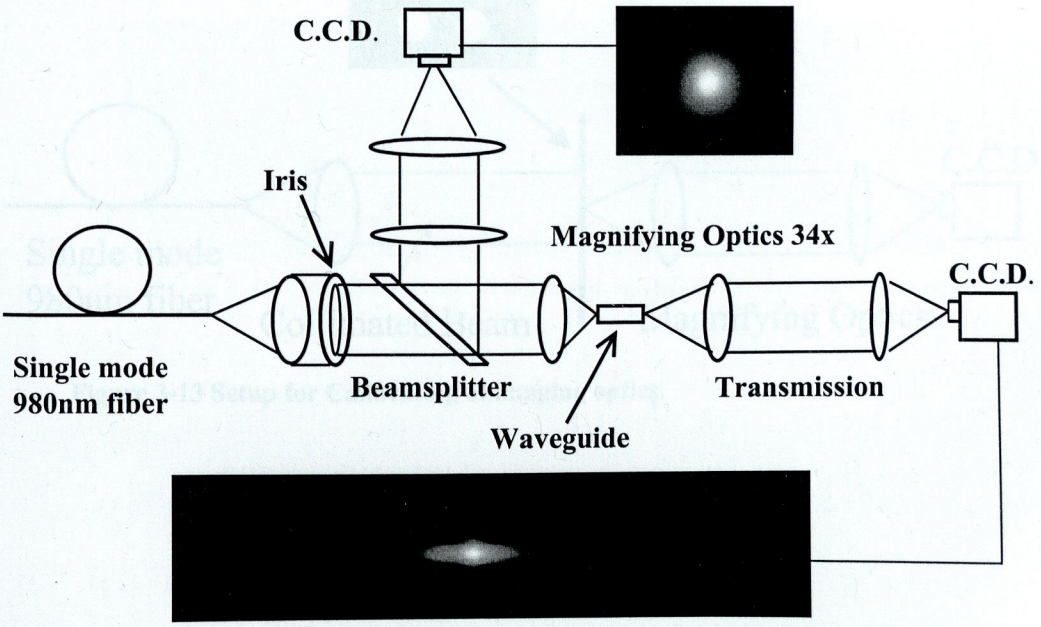

Figure 3-12 Experimental setup for making transmission measurements.

The magnification of this system was calibrated by imaging an electron beam etched pin-hole array of known dimensions using the same optics. Figure 3.13 shows the experimental setup that was used to perform this procedure. The purpose of the single mode fiber in this experimental setup was to spatially filter the light emitted from the laser. The emission from the fiber was both single lobed and circularly symmetric around the axis of the fiber. Consequently the collected light beam characteristics are superior to those of a beam collected directly at the laser facet. The absence of astigmatism in the beam allowed the beam to be easily focused to a spot on the waveguide facet. The diameter of the spot formed on the waveguide facet was measured to be about 1.3 μm (FWHM). The iris in the setup allowed the numerical aperture of the focusing lens to be varied. It was ensured that the incident waveguide facet coincided with the focal plane of the lens, by collimating light reflected back from the facet.

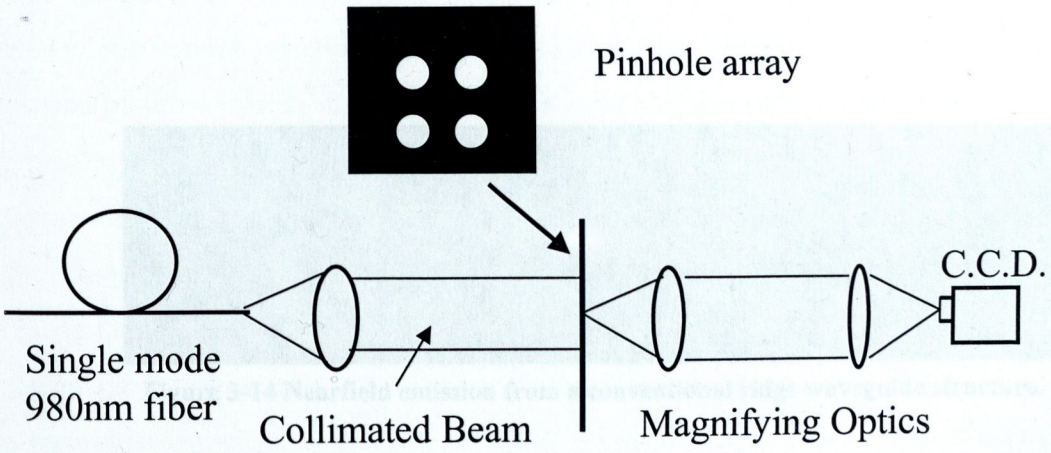

Figure 3-13 Setup for Calibrating of imaging optics.

3.4.2 Results and Discussion.

Nearfield emission patterns from the waveguide structures described in section 3.4.1 were obtained using the setup just described. The samples used in these experiments were cleaved to a length, l=2.0mm. This was done in order to ensure that the shape of the intensity distribution at the exit facet was not dependant on how the light was coupled into the waveguide. This hypothesis was tested by varying the beam waist of the collimated light that was being focused onto the entrance facet, and also by scanning the focused spot across this facet. Figure 3.14 shows the emission pattern from the conventional ridge structure shown in Figure 3.4. This structure was designed to be multimode in the transverse direction and single mode in the lateral direction. It can be seen from Figure 3.15 that the light is primarily guided in the fundamental mode with some slight contributions from higher order modes. This result indicates that the loss for the fundamental transverse mode of the structure is lower than for the higher modes. Further it also validated the waveguide model, which in turn allowed us to measure the characteristics of the Lo-guide structures with confidence.

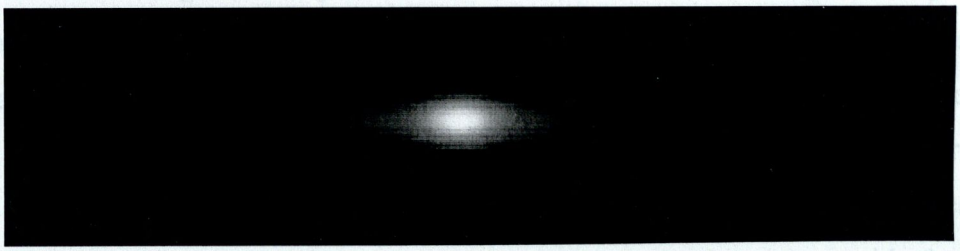

Figure 3-14 Nearfield emission from a conventional ridge waveguide structure.

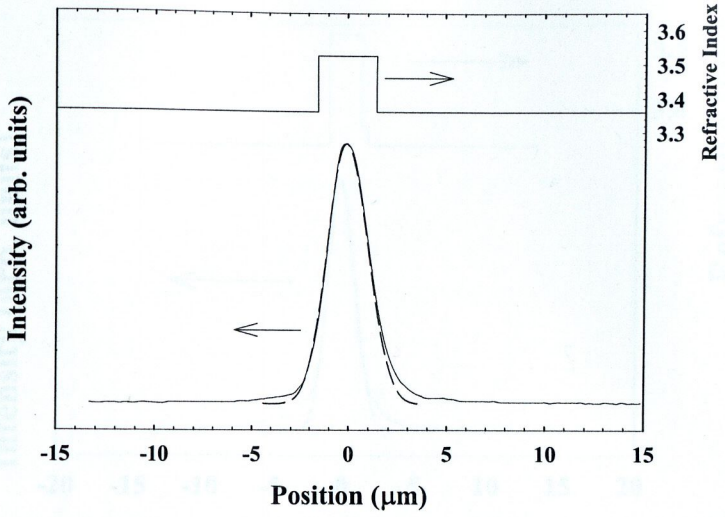

Figure 3-15 Comparison of, the measured transverse intensity distribution (solid) and the calculated intensity distribution of the conventional structure's fundamental transverse mode (dashed)

Nearfield images of both the symmetric and asymmetric novel waveguides, were obtained using the same experimental setup that used to obtain nearfield images for the conventional structures. Again the samples that were used were 2mm in length. Analysis of emission patterns relating to the asymmetric structure showed that the light was again being predominately guided by the lowest order transverse mode. This occurs because the lowest order mode also has the highest effective index, is thus more tightly confined and therefore experiences lower losses than the other guided modes. Extensive efforts were made to couple light into the other modes of the structure by varying the numerical aperture of the focusing lens and by scanning the focused spot the facet waveguide facet in the transverse direction. But as in the case of the conventional waveguide the output emission pattern remained insensitive to these changes in the input coupling setup. Below Figure 3.16 shows the measured light intensity profile, the calculated intensity profile of the fundamental mode, and refractive index profile in the transverse direction of the asymmetric waveguide shown in Figure 3.6. The growth direction in Figure 3.16 is in the direction of the positive sense of the horizontal scale

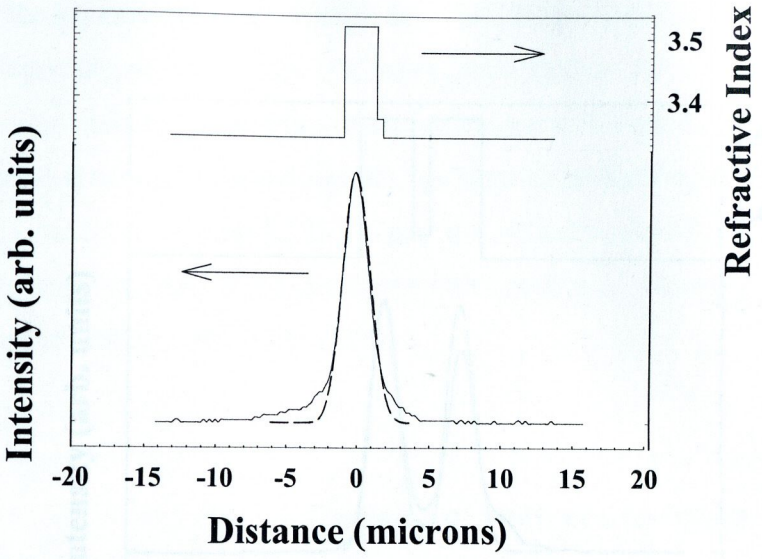

Figure 3-16 Comparison of, the measured transverse intensity distribution (solid) and the calculated intensity distribution of the asymmetric Lo-guide's fundamental transverse mode (dashed).

As in the case of the previously measured structures the emission patterns from the symmetric Lo-guide structure showed the light being predominately guided in the structure's lower order modes. In particular the two lobes in Figure 3.17 correspond perfectly with the high refractive index regions of the guiding structure. However unlike the asymmetric, the shape of the measured transverse intensity profile was in this case sensitive to changes in the position of the focused spot upon the facet. As in the previous two cases the growth direction in Figure 3.17 is in the direction of the positive sense of the horizontal scale. On the basis of these experiments it was obvious that in order to preferentially select the postulated highest order mode of these novel structures, it would be necessary to give those modes a competitive advantage.

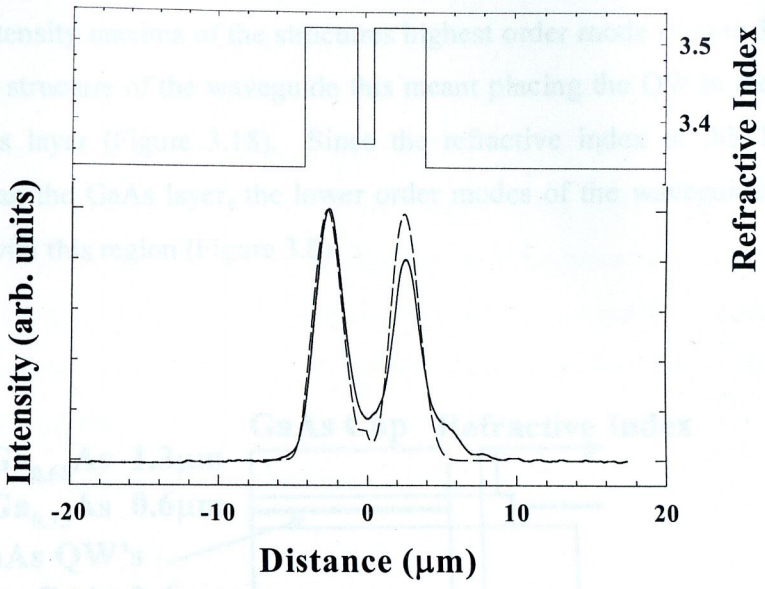

Figure 3-17Comparison of, the measured transverse intensity distribution (solid) and the calculated intensity distribution of the symmetric Lo-guide's fundamental transverse mode (dashed).

3.5 Optical Pumping.

The results of the last section, showed that it was not possible to selectively excite a particular higher order transverse mode, of either a conventional multimode waveguide or Lo-guide structure, simply by coupling light into them using an objective lens. Light coupled into these structures in this manner was nearly exclusively guided in the fundamental modes of these structures. This was accounted for by the fact these modes had the higher effective indices than the other modes and were thus more efficiently guided. It was therefore clear that in order to selectively excite the postulated highest order modes of the novel structures, it would be necessary to give them a competitive

advantage. To achieve this end it was decided to incorporate five $In_{20}Ga_{80}As$ quantum wells (QW) into the asymmetric novel waveguide. This design modification would allow the structure to optically pumped. The QW were positioned in the wavguide so as to correspond to the intensity maxima of the structures highest order mode (Figure 3.8). In relation to expitaxal structure of the waveguide this meant placing the QW in the center of the $Al_{0.28}Ga_{0.72}As$ layer (Figure 3.18). Since the refractive index of this layer is substantially less than the GaAs layer, the lower order modes of the waveguide have a very small overlap with this region (Figure 3.8).

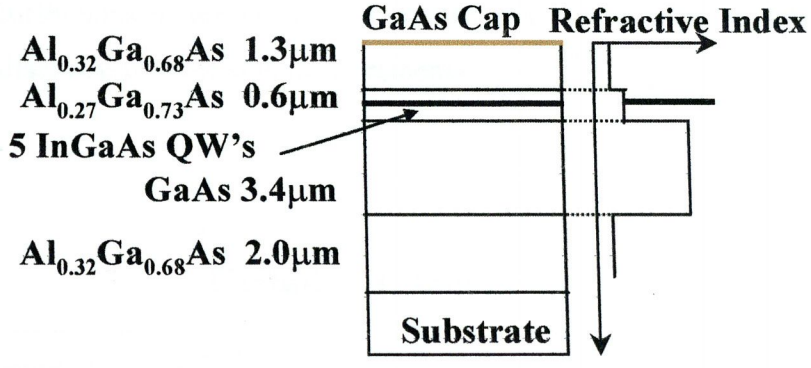

Figure 3-18 Asymmetric Lo-guide structure containing five InGaAs quantum wells.

Again from referring to Figure 3.8, it can be seen that the two highest order modes of the structure had confinement factors with the multiple quantum well active region, which were more than an order of magnitude greater than those of the other modes. The modified structure should now function as a laser device if sufficiently pumped by an external laser source of the appropriate wavelength. It was further expected that excitation of the quantum well material would preferentially excite the waveguide's two highest order modes. These modes should have a much lower lasing threshold and experience far greater positive feedback from the cavity than the other modes. A similar approach to this one was used by Hofstetter *et al* in [7], to selectively excite a higher order transverse mode of a GaN/AlGaN waveguide.

3.5.1 Experimental Details.

Due to bandgap considerations and the availability of an appropriate wavelength pump laser, it was only feasible to attempt to optically pump the asymmetric waveguide structure. Figure 3.19 shows a schematic diagram of the experimental setup used for optical pumping. The sample was pumped using a Q switched, frequency doubled, Nd:YAG laser with emission at λ = 532nm and pulse length of 5ns. The pump laser emission was focused to a narrow (≈50 μm FWHM) stripe using both a cylindrical and spherical lens. Care was taken to ensure that the stripe was of uniform intensity along the full length of the sample (2.1mm). The pump energy was measured with a calibrated Gentec energy meter and was varied using a variable neutral density filter. Nearfield intensity distributions of the facet were imaged in the same way as they were in the previously disclosed transmission measurements.

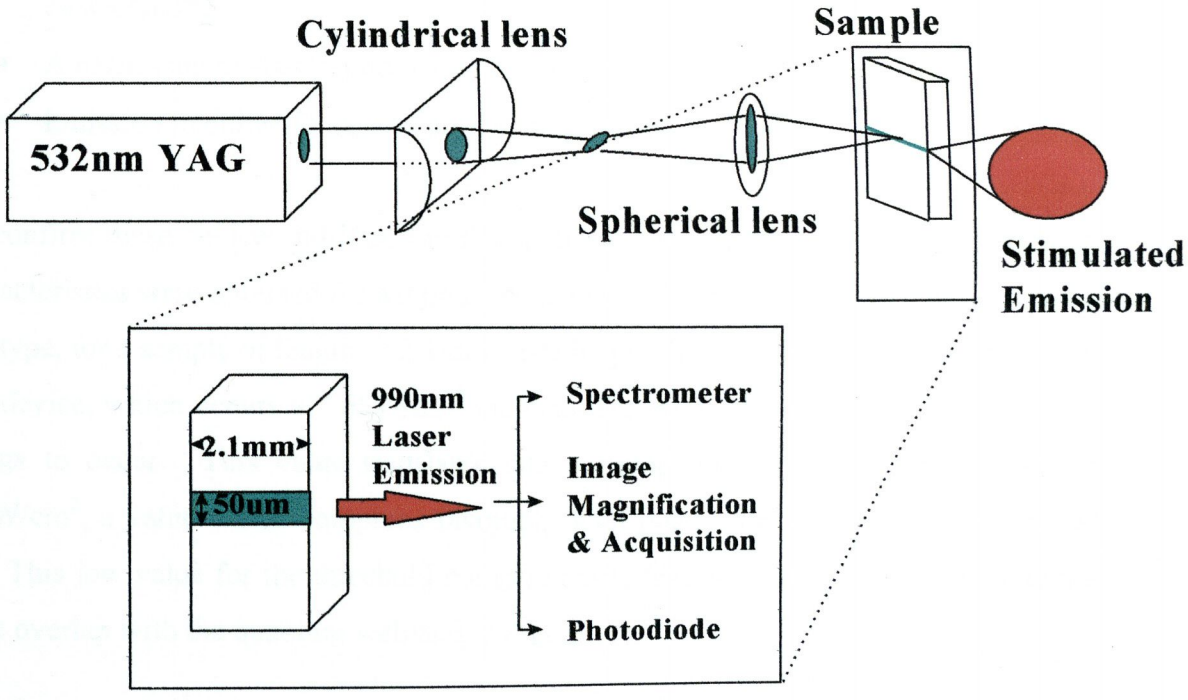

Figure 3-19 Optical pumping setup

A light emission versus pump power characteristic was obtained by collecting and collimating the edge emission from the sample, then focusing it onto a Si photodiode. In both of these measurements the collected light was passed through a GaAs wafer to filter out any green light reflected from the edge of the sample. Spectra of the laser emission were also taken at different pump energies using a spectrometer, CCD combination. Finally a Glan Thompson polariser was used to determine the polaristion of the laser emission.

3.5.2 Experimental Characterization and Results.

Before imaging the emission patterns from these devices, it was first necessary to ensure that the devices were indeed lasing. The following criteria were used to assess whether lasing action was taking place:

- The observation of a threshold in the output power versus pump intensity characteristic,
- A narrowing of spectral linewidth above threshold,
- Emission in either TE or TM polarization states.

To confirm these devices fulfilled the first criteria, output power versus pump intensity characteristics were obtained for a number of devices. Figure 3.20 shows a typical plot of this type, for a sample of length, l=2.1mm. The huge change in the quantum efficiency of this device, which occurs at 75kW/cm^2 indicates the pump threshold where laser action beings to occur. This value translates into a pump intensity per quantum well of 15kW/cm^2, a value which compares favorably with others reported in the literature [8] [9]. This low value for the threshold pump intensity also indicates that lasing mode has large overlap with the quantum well active region.

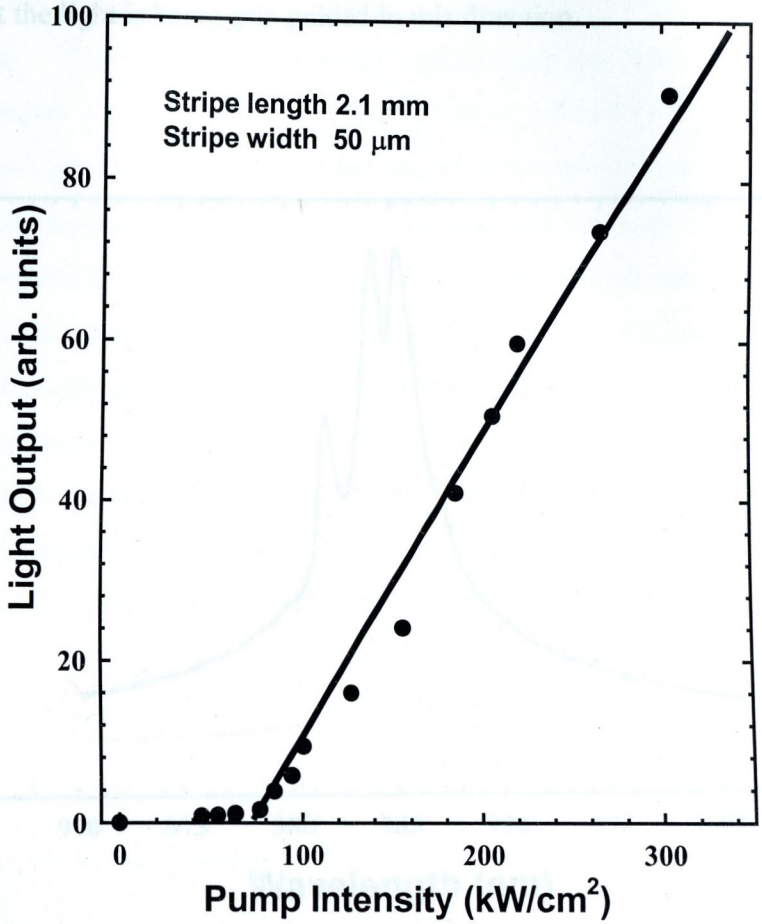

Figure 3-20 Light emission versus optical pump power for asymmetric Lo-guide structure.

The second criteria was verified by comparing the FWHM of spectral linewidth above and below threshold, the values obtained for these quantities were 6nm and 25nm respectively. Figure 3.21 shows measured emission spectra at pump intensities of 100kW/cm^2, 1.33× threshold (red), and 300kW/cm^2, 4.0× threshold (black). The spectral resolution of our measurement setup was estimated to be 0.5nm, consequently we were unable to distinguish the individual Fabry-Perot modes of the laser cavity (free spectral

range ≈ 0.05nm). The spectral modulation is almost certainly due to the waveguide being multimode in the lateral direction. This in turn is due the optical stripe being 50μm wide and the fact that the light is being gain guided in this direction.

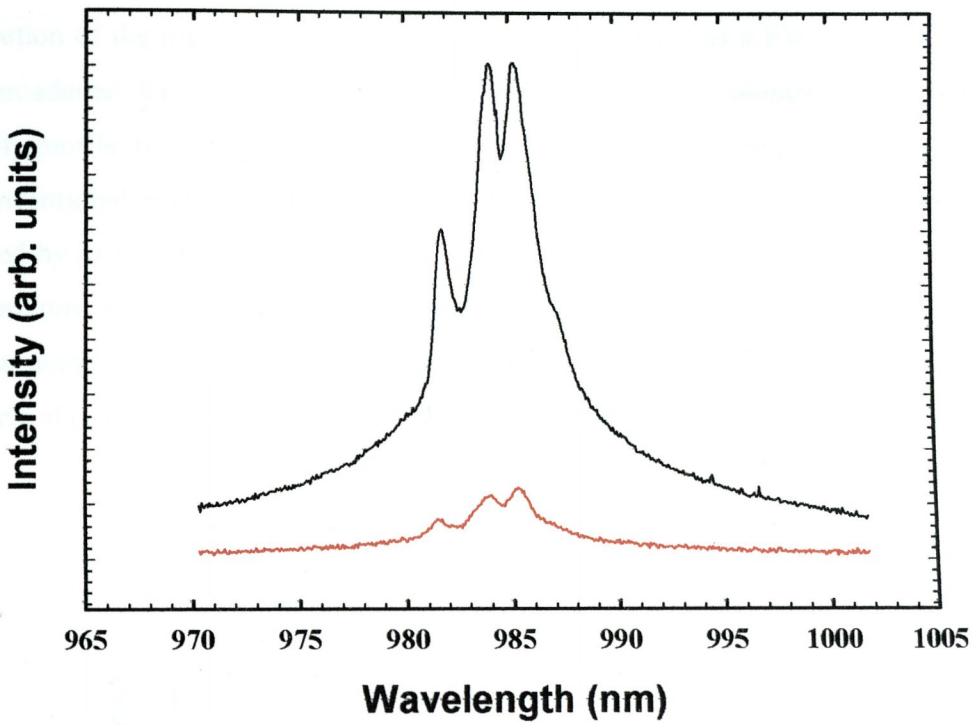

Figure 3-21 Measure wavelength spectrum produced by the optically pumped asymmetric Lo-guide structure at approximately 1.33× (red) and 4.00× (black) threshold

Finally the laser emission was determined to be TE polarized. This is was to be expected for the reasons detailed in Section 2.9.4

3.5.3 Near Field Measurements.

With conclusive evidence of lasing action in these structures now demonstrated, their above threshold nearfield emission patterns were now examined. Figure 3.22 shows the

measured calculated and expected transverse emission profiles. The black line is the measured transverse intensity profile produced by optically pumping the structure above threshold. The red line is the calculated intensity profile of the structures highest order transverse mode. The differences between calculation and measurement can be somewhat reconciled by taking into account the spatial resolution of the experimental setup. The green line attempts to account for this, by convolving the calculated intensity distribution of the highest order mode with a Gaussian that had a FWHM of 1μm [10]. This broadened intensity profile shows significantly better agreement with measured intensity profile, than the purely theoretical mode profile. As can be seen from Figure 3.8 the conventional modes could not produce a nearfield pattern resembling that, which was obtained by experiment. Therefore we conclude that the structure is lasing, in one of, or an admixture of, the structures two highest order modes [11]. This result also explains the low pump threshold value reported in Section 3.5.2, since these are the only modes that have significant overlap with the QW active region (4.26% and 5.47%).

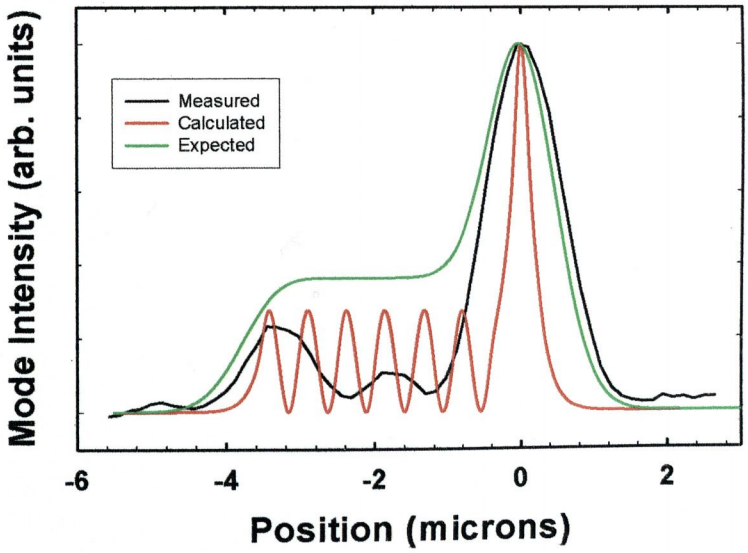

Figure 3-22 Measured, Calculated and Expected transverse nearfield intensity profiles

3.6 Summary.

This Chapter has been concerned with the characterisation of conventional and Lo-guide passive waveguide structures and with the investigation of an optically pumped Lo-guide laser device under pusedo-CW conditions. In the latter case, measurements were made of the emitted power versus optical pump power for devices with 2mm different cavity lengths. From these results values for the slope efficiency and the pump threshold were obtained. Wavelength spectra were measured at different pump powers to ensure a narrowing in the laser linewidth was obversed as threshold was exceeded. The primary function of the measurements mentioned thus far was to demonstrate lasing action in these devices. However the low threshold pump power already suggested that the device was lasing in one of its two highest modes, as these were the only modes with a significant overlap with the QW active region. Finally measurement of the nearfield emission patterns from these devices confirmed this to be the case.

3.7 References.

1 S. Adachi. GaAs,AlAs, and $Al_xGa_{1-x}As$: Material parameters for use in research and device applications. *J. Appl. Phys.*, 58(3), August 1985.

2 G. Burns. *Solid State Physics*. International Press 1985. Section 13.5

3 S. Adachi. Refractive indices of III-V compounds: Key properities of InGaAsP relavant to device design. *J. Appl. Phys.*, 53(8), August 1982

4 D. Marcuse. *Theory of Dielectric Optical Waveguides 2nd Edition*. Academic press 1991.

5 D. C. Mehuys. "*High Power Semiconductor Lasers*", in *Semiconductor lasers II*. E. Kapon (Editor). Academic Press 1999.

6 J. Buss. The Effect Index Method and its Application to Semiconductor Lasers. *IEEE J. Quantum Electron.*, QE-18(7): 1083-1089, July 1982

7 D. Hofstetter, D.P. Bour, R.L. Thornton, and N.M. Johnson, Excitation of a higher order transverse mode in an optically pumped $In_{0.15}Ga_{0.85}N/In_{0.05}Ga_{0.95}N$ multiquantum well laser structure. *Appl. Phys. Lett.*, 70(13):1650-1652, March 1997.

8 F.P. Logue, P. Rees, J.F. Heffernan, C. Jordan, J.F. Donegan, J. Hegarty, F. Hiei, and J. Ishibashi. Effect of Coulomb enhancement on optical gain in (Zn,Cd)Se/ZnSe multiple quantum wells. *Phys. Rev. B*, 54(23): pp 16417-16420, December 1996.

9 J.F. Donegan, C. Jordan, P. Rees, F.P. Logue, J.F. Heffernan, and J. Hegarty. A study of internal loses in CdZnSe/ZnSe multiple quantum well materials. *J. Crystal Growth*, 159:653-656, 1996

10 Erwin Kreyseig. *Advanced engineering mathematics, Seventh edition*. Wiley 1993. Chapters 6 and 10.

11 J. A. Patchell, F.P. Logue, J. O'Gorman, J. Hegarty, B. A. Usievich and V. A. Sychugov. Demonstration of high-brightness-mode propagation in a compound waveguide structure. *Appl. Phys. Lett.*, 75(2): 169-171, July 1999

Chapter 4

A Prototype Laser Diode Structure.

4.1 Introduction.

Having demonstrated that it was possible to excite the last mode before cut-off in our novel waveguide by optically pumping, it was decided to incorporate a similar waveguide design in a laser diode device. This represented the first attempt to implement the Lo-guide concept in an electrically pumped device. Again due to energy band considerations and wavguiding issues, it was easier to implement the Lo-guide concept in the growth direction based on the asymmetric waveguide structure. This device is basically a separate confinement heterostructure in which the carriers are confined by the quantum wells and the light by the waveguide structure. The main difference between this and the optically pumped structure, is that the layers in this structure are doped so as to allow the device to be electrically pumped. The refractive index profile of this device was also slightly different from that of the optically pumped sample. This design modification was to ensure that there was only one mode that had an anti-node in the low refractive index region of the structure, as opposed to the optically pumped sample that had two. This Chapter details the structure of the novel laser diodes mentioned above, and the experimental analysis that was carried out on these laser diode devices, and the results obtained.

4.2 Device Structure.

The laser diode devices investigated in this section are essentially separate confinement heterostructures based on the asymmetric waveguide design introduced in Section 2.10.

The waveguide design was realized using GaAs/$Al_xGa_{1-x}As$ layers of different composition and thickness, grown on a GaAs substrate. The complete expitaxial structure of these laser diode devices is shown in Figure 4.1. The top two layers of the structure, the GaAs cap and the $Al_{0.30}Ga_{0.7}$ As upper cladding layer were doped p-type with respective acceptor concentrations of $5\times10^{18}cm^{-3}$ and $5\times10^{17}cm^{-3}$. As in the case of the optically pumped structure, it was intended that these devices should lase in their highest order transverse mode. To this end two 10nm InGaAs quantum wells (surrounded by three 10nm GaAs barrier regions) were optimally placed in the $Al_{0.27}Ga_{0.73}As$ layer to achieve the highest possible overlap with this mode. Also the low index $Al_{0.27}Ga_{0.73}As$ region of the waveguide was left undoped to reduce the internal cavity losses [1]. The high index region of the waveguide structure, the bottom cladding layer and the substrate were doped n-type with respective donor concentrations of $5\times10^{17}cm^{-3}$, $1\times10^{18}cm^{-3}$ and $2\times10^{18}cm^{-3}$. The substrate layer and the previously mentioned GaAs cap layer were highly doped to reduce the series resistance of the device. The device structure was implemented on a GaAs substrate with a two inch diameter. A portion of this wafer was processed into laser chips of two stripes widths, W= 20 and 50μm and three cavity lengths, l = 0.530, 0.720 and 0.956mm.

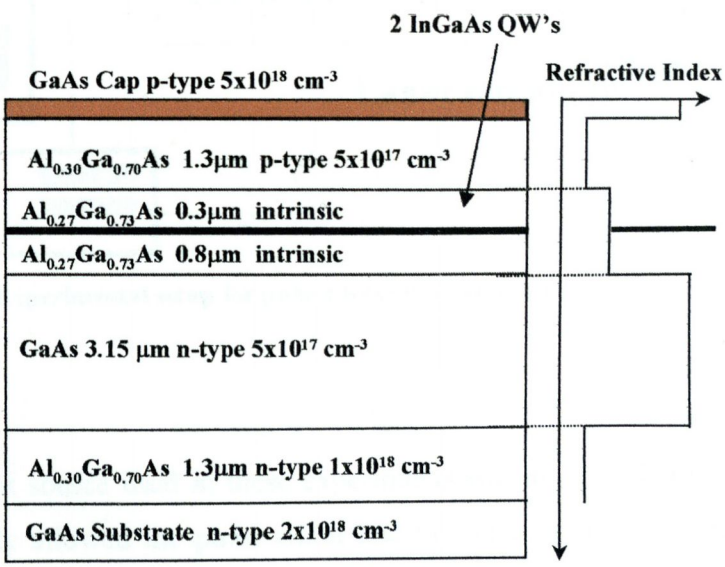

Figure 4-1 Epitaxial structure of asymmetric Lo-guide structure implemented in the transverse direction.

4.3 Experimental Setup.

Figure 4.2 is an illustration of the experimental setup that was used to make pulsed laser diode measurements. Of primary interest in this illustration is the laser mount. The base of the mount on which the laser chip sits, was made from oxygen free copper which was subsequently gold coated. A tapered phosphor bronze contact, again gold coated, could be raised or lowered to complete the circuit with pulse generator. The tip of the tapered contact was about 10μm in width, and thus of comparable size to the width of the laser stripe.

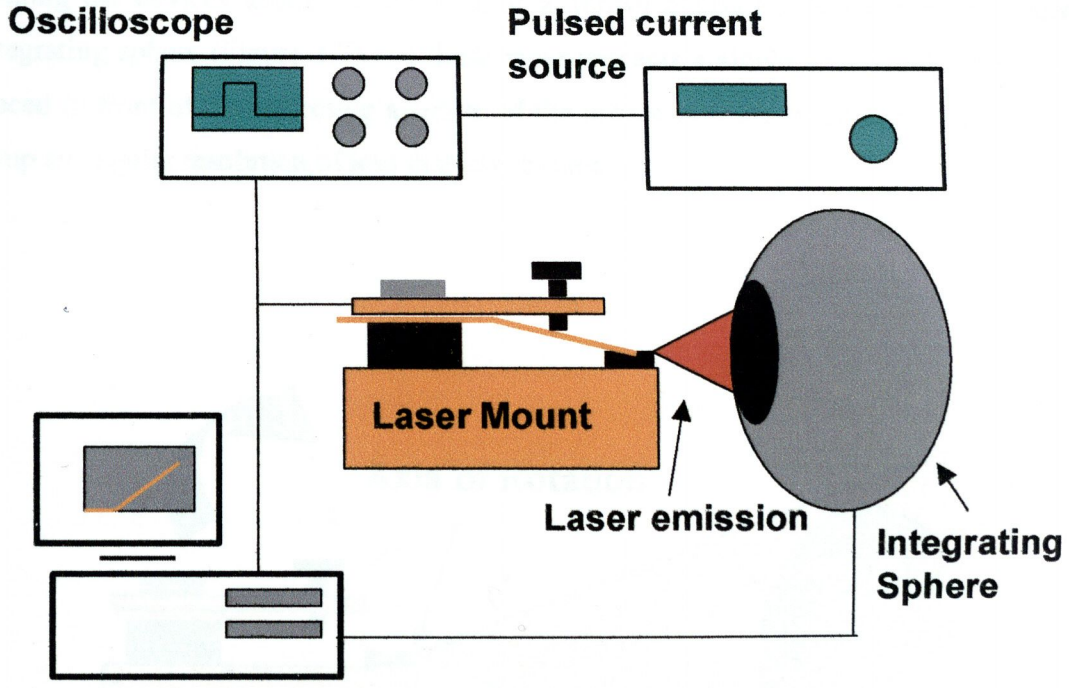

Figure 4-2 Experimental setup for pulsed laser measurements.

The pulsed current source used in these experiments was an ILX lightwave LDP-3840; this current supply allowed the pulse width and the duty cycle to be varied. In these experiments the laser was operated at a 1% duty cycle with a pulse duration of 0.5μs in

order to avoid device heating. The shape and amplitude of the current pulses being applied to the laser devices were monitored using a 20MHz oscilloscope. The output power from the laser diodes was measured using a Melles Griot optical power meter together with a silicon integrating sphere. The laser was mounted at the center of the collecting aperture of the integrating sphere ensuring that all the light was collected for an absolute power measurement. The entire setup was computer controlled via General Purpose Interface Bus (GPIB) connections, with the pulsed current source and the power meter. The wavelength spectrum of the device was measured using an HP70951A optical spectrum analyser. Near field measurements of the lasers emitting aperture were made using the experimental setup described previously in Section 3.4. Farfield emission profiles were also obtained for these devices. These measurements were made by rotating the devices about a fixed axis, at a known distance (10cm) from the silicon integrating sphere (Figure 4.3). In these measurements a single slit of width 1mm was placed in front of the collecting aperture of the sphere in order to give the experimental setup an angular resolution of less than one degree.

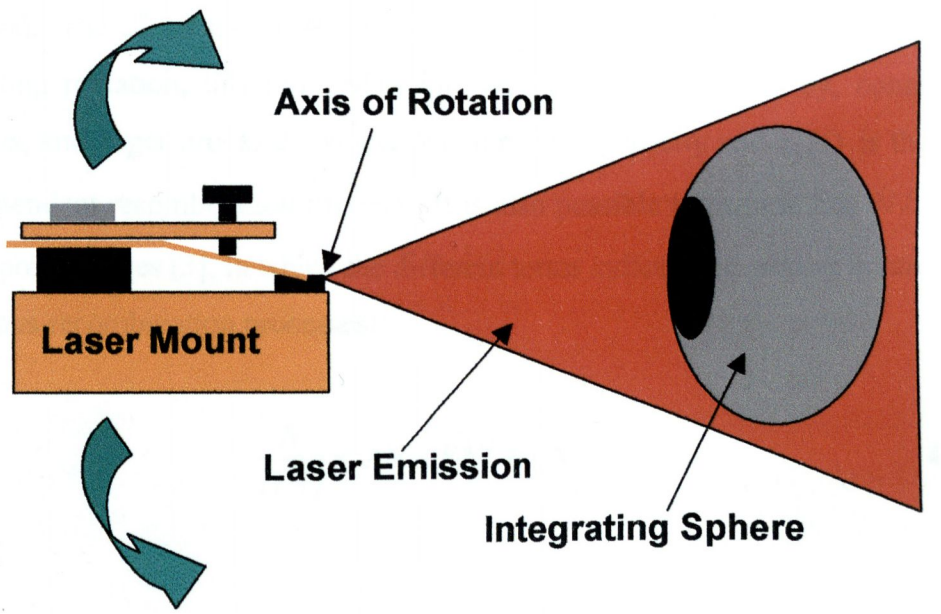

Figure 4-3 Farfield measurement setup.

4.4 Laser Diode Parameters.

This section is initially concerned with deriving some basic parameters, which are useful in quantifying laser diode behavior, from the standard laser diode rate equations [2]. On completion of this exercise it is then shown how these parameters can also be determined from experimental data. We start with a description of these rate equations:

$$\frac{dN}{dt} = \frac{\eta_i I}{qV} - \frac{N}{\tau(N)} - v_g g(N) N_p \qquad 4.1$$

$$\frac{dN_p}{dt} = \Gamma v_g g(N) N_p + \Gamma \beta_{sp} R_{sp} - \frac{N_p}{\tau_p} \qquad 4.2$$

Equations 4.1 and 4.2 are the coupled differential equations, which respectively describe the rate of change of the carrier and photon densities in these devices. In Equation 4.1 the 1st term $\eta_i I / qV$, describes the rate at which carriers are created in the active region due to a current *I,* flowing through the device. Here, *V,* is the volume of the active region, this is the region where recombining carriers contribute to useful gain and photon emission, q is the electronic charge. Finally, η_i, is the internal quantum efficiency, this is the fraction of the current flowing through the device that generates carriers in the active region. The 2nd term describes the rate at which carriers recombine in the absence of stimulating radiation, this term takes into account recombination by, nonradiative, spontaneous, and auger processes, where N is the carrier density and $\tau(N)$ is the carrier density dependent recombination lifetime. It is also possible to express this $N/\tau(N)$ in terms of a power series [3], in which the different terms indicate the relative contributions of the various recombination processes:

$$\frac{N}{\tau(N)} = AN + BN^2 + CN^3 \qquad 4.3$$

Here AN is the sum of the recombination rates from two different processes, defect recombination and surface recombination. Spontaneous electron-hole recombination is associated with the BN^2 term, while CN^3 parameterises the two body Auger recombination process. The 3rd term Equation 4.1 accounts for radiative recombination, which is stimulated by photons in the cavity. This term is the product of the group velocity of the light in the cavity, v_g, the level of gain in the laser cavity, $g(N)$, and N_p, the photon density in the active region. Equation 4.2 describes how the rate of change of the photon density in the active region changes with respect to time. The first term in this equation is identical to the 3rd term in Equation 4.1 apart from the inclusion of the confinement factor Γ. The 2nd term in Equation 4.2 accounts for the fraction of photons generated by spontaneous emission which couple into the lasing mode. It is the product of the confinement factor, a coupling co-efficient for the spontaneous emission β_{sp}, and the spontaneous electron hole recombination rate. This is the reciprocal of the number of modes in the bandwidth of the spontaneous emission. Finally the term N_p/τ_p accounts for absorption, scattering, and mirror losses associated with the cavity.

The solutions of Equation 4.1 and 4.2 show that the steady state gain in a laser diode operating above threshold must equal its threshold value g_{th}. Furthermore since the gain and the carrier density are directly related, the carrier density must also clamp at its threshold value N_{th}. Thus when a current greater than the threshold current I_{th} is flowing through the device, it is possible to rewrite Equations 4.1 and 4.2 as follows.

$$\frac{dN}{dt} = \eta_i \frac{(I - I_{th})}{qV} - v_g g_{th} N_p \qquad 4.4$$

$$N_p = \frac{\eta_i (I - I_{th})}{q v_g g_{th} V} \qquad 4.5$$

Equation 4.5 is obtained by setting $dN/dt = 0$. The next step in deriving an expression which relates the injected current and the output power from a device operating above threshold, is to write the energy stored in the cavity $\mathscr{E}_s$ in terms of the photon density.

$$\mathscr{E}_s = N_p h\nu V_p \qquad 4.6$$

The output power from the cavity, P_0, is now obtained by multiplying, $\mathscr{E}_s$, by the rate of energy loss cavity, $v_g\alpha_m$.

$$P_0 = v_g \alpha_m N_p h\nu N_p \qquad 4.7$$

Here α_m is the mirror loss of the cavity, which is defined in terms of the device cavity length, L, and the reflectivities of the facets r_1 and r_2.

$$\alpha_m = \frac{1}{L}\ln\frac{1}{r_1 r_2} = \frac{1}{L}\ln\frac{1}{R} \qquad 4.8$$

where $R = \sqrt{r_1 r_2}$. Equation 2.2 assumes a confinement factor of unity, i.e. that $\Gamma = V/V_p = 1$. In general this is not the case however, we therefore rewrite Equation 2.2 as follows.

$$\Gamma g_{th} = \alpha_i + \frac{1}{L}\ln\frac{1}{r_1 r_2} \qquad 4.9$$

Substituting from Equations 4.5 and 4.9 into Equation 4.7 yields

$$P_0 = \eta_i\left(\frac{\alpha_m}{\alpha_i + \alpha_m}\right)\frac{h\nu}{q}(I - I_{th}) \qquad 4.10$$

for $I > I_{th}$. Equation 4.10 expresses the output power from a device in terms of the injection current, as well as some of the basic laser diode parameters, such as η_i, α_i, and α_m. The differential quantum efficiency, η_d, is the ratio of the number of photons emitted by the laser to the number of electrons flowing through the device, it can be defined as follows.

$$\eta_d = \frac{\eta_i \alpha_m}{\alpha_i + \alpha_m} \qquad 4.11$$

The value of η_d for a particular device can also be obtained from a measured light – current characteristic, by use of the following expression.

$$\eta_d = \frac{q}{\hbar\omega}\frac{dP}{dI} \qquad I > I_{th} \qquad 4.12$$

In Equation 4.12, dP/dI is the slope efficiency of the device above threshold, in Watts/Amp. Previously it has been mentioned that the mirror losses can be calculated once the cavity length and the facet reflectivities are known, Equation 4.8. This leaves only two unknown in Equation 4.10, namely η_i, α_i. These parameters can be determined if the values of, η_d, and α_m are known for two or more different cavity length devices, which differ only in length. Substituting Equation 4.8 into Equation 4.11 for two lasers with cavity lengths L_1 and L_2, yields the following equations.

$$\eta_{d,1} = \frac{\eta_i \ln\left(\frac{1}{R}\right)}{L_1\alpha_i + \ln\left(\frac{1}{R}\right)} \qquad 4.13$$

$$\eta_{d,2} = \frac{\eta_i \ln\left(\frac{1}{R}\right)}{L_2\alpha_i + \ln\left(\frac{1}{R}\right)} \qquad 4.14$$

Solving for η_i, and α_i we find that

$$\alpha_i = \frac{\eta_{d,2} - \eta_{d,1}}{L_1\eta_{d,1} - L_2\eta_{d,2}} \ln\left(\frac{1}{R}\right) \qquad 4.15$$

$$\eta_i = \eta_{d,1}\eta_{d,2}\frac{L_1 - L_2}{L_1\eta_{d,1} - L_2\eta_{d,2}} \qquad 4.16$$

Although Equations 4.15 and 4.16 allow the parameters, α_i and η_i, to be calculated using the experimental data obtained from two appropriate devices, there will in practice be some error associated with each of these measurements. More accurate values for α_i and η_i can generally be determined by plotting the reciprocal of η_d versus cavity length, for a number of different cavity length devices. The resulting straight line graph is described by the following expression

$$\frac{1}{\eta_d} = \frac{\alpha_i}{\eta_i \ln\left(1/R\right)} L + \frac{1}{\eta_i} \qquad 4.17$$

It thus possible to workout, α_i, from the slope of such a plot and, η_i, from its intercept with the y-axis.

4.5 Device Characterization.

In this section the results of all the measurements on the asymmetric electrically pumped Lo-guide devices are presented. The measurements preformed can be divided into two categories. Fristly those that were undertaken to ensure that the devices were not displaying anomalous behavior, this primarily consisted of obtaining light current characteristics for different cavity lengths and stripe widths. Secondly those carried out to characterize the nearfield and farfield emission patterns from the devices.

4.5.1 Electrical Measurements.

In this section the electrical characteristics of the sample devices introduced in Section 4.2 are investigated. Experimental values are obtained for the various parameters that were discussed in the previous section, threshold current, slope efficiency, etc. Initially

referring to the laser emission versus electrical current characteristic in Figure 4.4, which was obtained for a 50μm stripe device, with a 956μm cavity length. This graph shows the peak pulse power versus the laser drive current, which was varied between zero and three amps (more than 16× the value of the threshold current). From the data in Figure 4.4, the slope efficiency of this device was calculated to be 0.59W/A, while a maximum peak pulse power of 1.61Watts was observed at an operating current of 2.9 Amps. The values for the peak pulse power in this graph were obtained by scaling the collected power reading, by the duty cycle of the electrical pulses applied to the laser (factor of 100). Also as these devices were uncoated the collected power was multiplied by a further factor of two, to give the stated peak pulse power values.

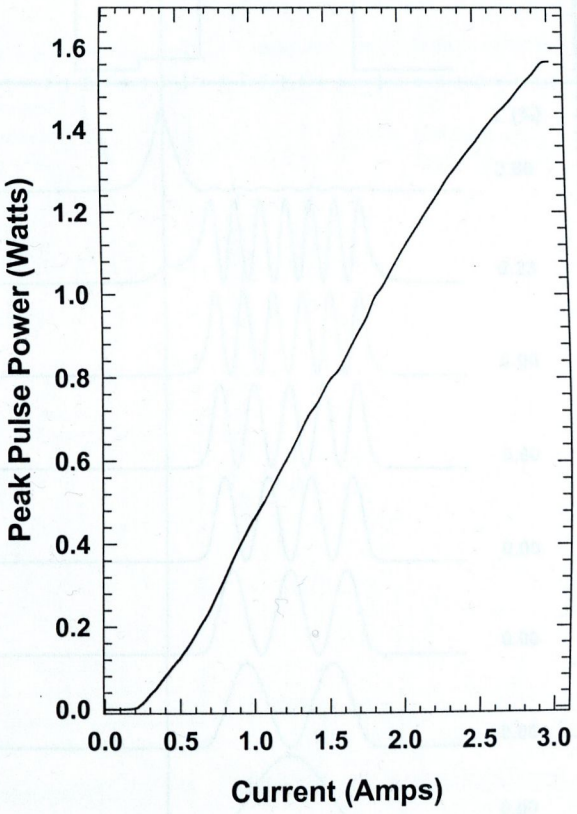

Figure 4-4 Light current characteristic for a 50μm stripe device with a cavity length of 956μm.

The threshold current for this laser was 225 mA corresponding to a threshold current density of $\approx 470 A/cm^2$. The means that the threshold current density per quantum well is $\approx 235 A/cm^2$. Considering that a portion of the highest order mode is predicted to propagate in a moderately doped region, this value is quite reasonable compared with reported literature values [4] [5]. This indicates that the lasing mode has a considerable overlap with the active region of the device. Figure 4.5 shows the intensity distributions and confinement factors for each the guided modes in the structure.

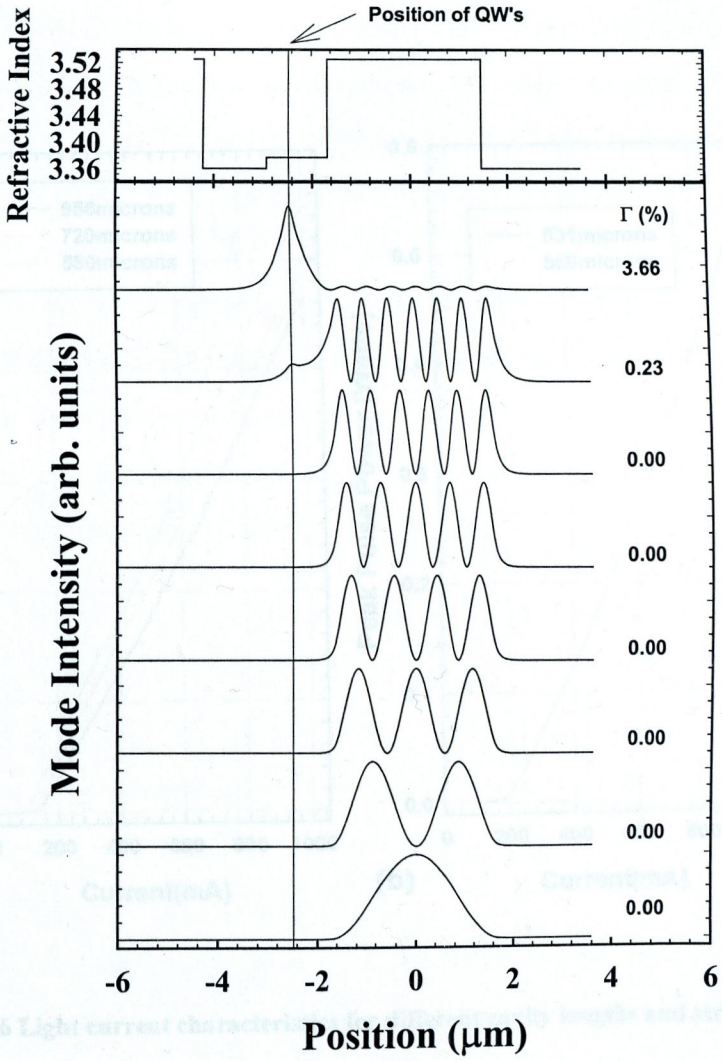

Figure 4-5 Mode structure of electrically pumped asymmetric Lo-guide structure

It can be seen from Figure 4.5 that the highest order mode of this structure has a confinement factor (calculated to be 3.66%), which is more than order of magnitude greater than other modes of the structure. Referring back to Equation 4.9 it is clear that this mode will have a much lower lasing threshold than the other modes. Thus the low threshold current density value is an indication that the structure is lasing in its highest order mode.

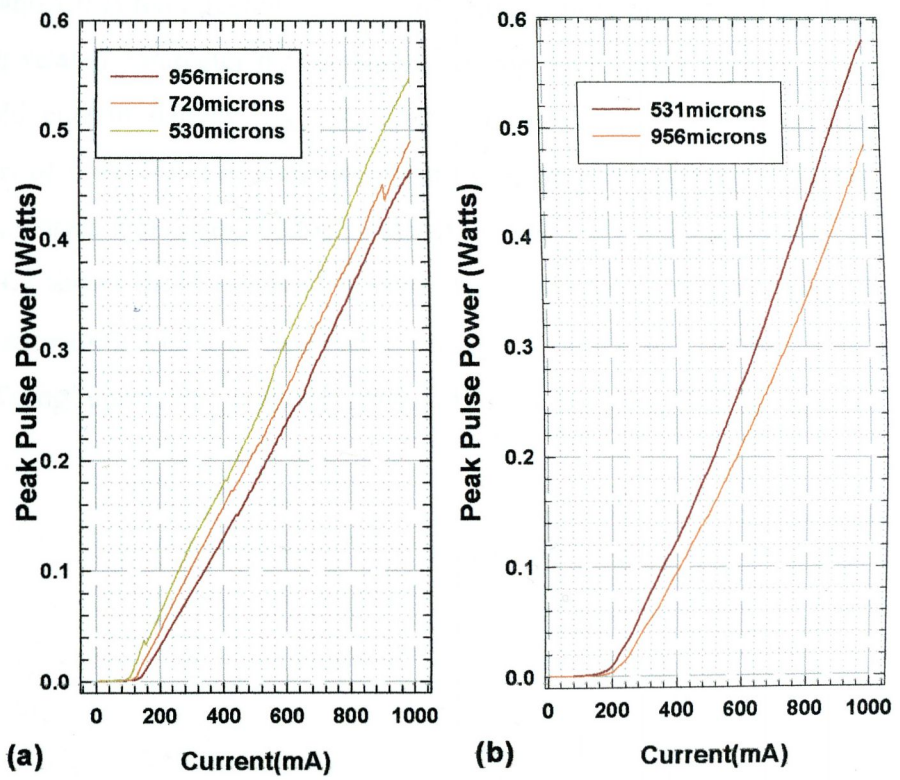

Figure 4-6 Light current characteristics for different cavity lengths and stripe widths.

As explained in Section 4.4 in order to experimentally obtain values for parameters such as η_i, α_i, it is necessary to measure light – current characteristics for two or more devices with different cavity lengths. Figures 4.6 (a) and (b) are plots of the peak pulse power the versus drive current for different cavity length devices, which have stripe widths of 20 and 50μm respectively. These measurements were preformed to show that the devices which incorporate the novel waveguide structure do not exhibit any unexpected behavior. As expected the slope efficiencies (Table 4.1) of these devices decreased with increasing cavity length. The reason for this is as follows, longer cavity length devices have greater internal loses, but smaller mirror loses per unit length. Thus the value of the $(\alpha_m / \alpha_i + \alpha_m)$ term in Equation 4.9 is reduced, this in turn reduces the slope efficiency and differential quantum efficiency. By taking the second derivative of these curves, values for the threshold currents of these devices were also obtained (Table 4.1). These values show that the threshold current increases with both cavity length and stripe width. Another related parameter that is equally as important as the threshold current, I_{th}, is the threshold current density, J_{th}. As expected it was found that the threshold current densities of these devices decreased with increasing cavity length. Further analysis of how, J_{th}, varies with stripe width yields an insight into carrier spreading in these devices. Figure 4.7 shows these values of J_{th} plotted against inverse cavity length. In this plot it is current spreading which is responsible for higher values of J_{th} in the 20μm stripe devices. In [6], Tsang reports on increased values of J_{th}, in narrow stripe laser diodes.

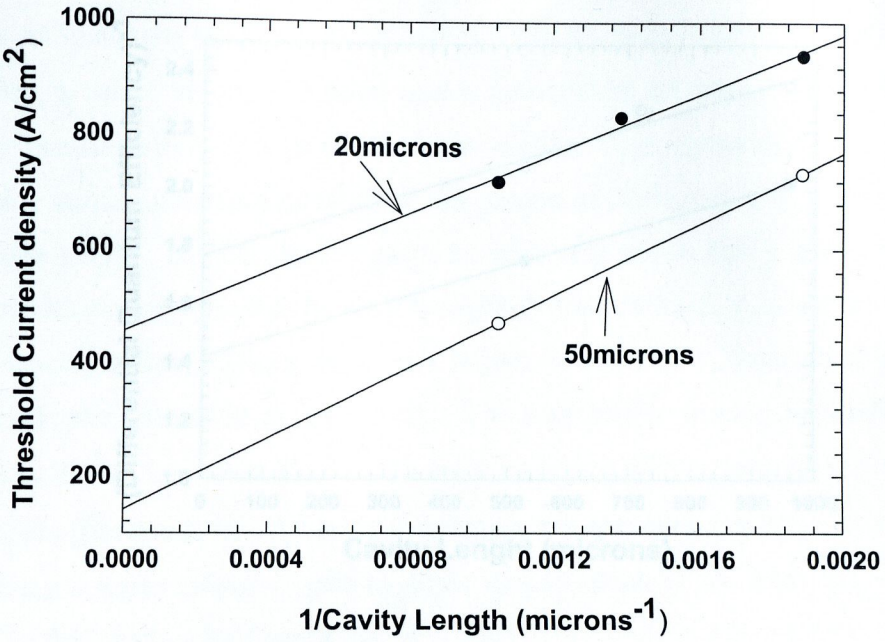

Figure 4-7 Threshold current density plotted against the inverse cavity for20μm and 50μm stripe width devices with different cavity lengths

Referring back to Section 4.4, it was stated that in order to calculate the internal optical losses and internal quantum efficiency of a particular laser structure, it is necessary to know the differential quantum efficiencies of two or more structures, which differ only in cavity length. Plotting the reciprocal of the differential quantum efficiency of each device against cavity length reveals two straight lines. The slopes of these lines show the internal loses for the 20μm and 50μm stripe devices to be 8.3cm^{-1} and 9.8cm^{-1} respectively. While the points at which these lines intersect the y-axis show the internal quantum efficiencies for the 20μm and 50μm stripe devices to be 0.57 and 0.70 respectively. The lower value the for the internal quantum efficiency in the 20μm stripe devices is due to current spreading in these devices. This result is consistent with the higher values of threshold current density observed in these devices.

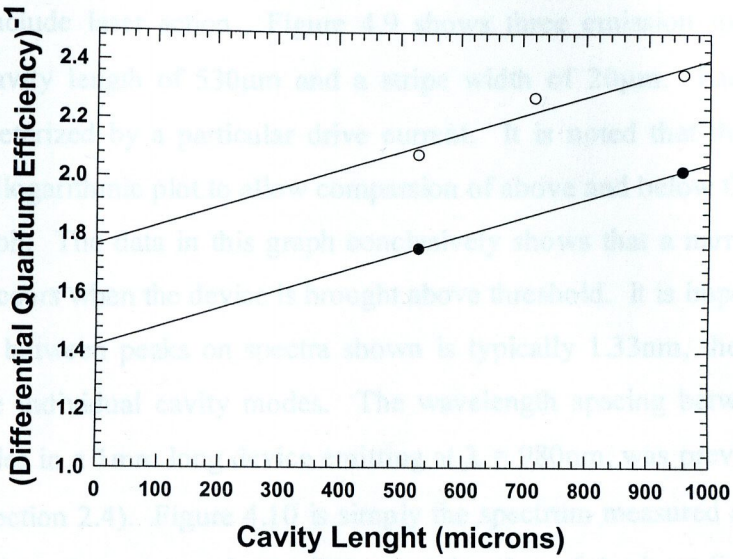

Figure 4-8 Reciprocal of the differential efficiency plotted against cavity length for 20μm and 50μm stripe width devices with different cavity lengths

Laser diode Parameters					
Stripe Width W (μm)	20	20	20	50	50
Cavity Length L (μm)	956	720	530	956	530
Threshold Current I_{th} (mA)	137	120	100	225	195
Threshold Current Density J_{th} (A/cm^2)	719	833	941	470	734
Slope Efficiency (W/A)	0.54	0.56	0.61	0.63	0.72
Differential Quantum Efficiency (η_d)	0.42	0.44	0.48	0.57	0.49
Internal Quantum Efficiency (η_i)	0.57	0.57	0.57	0.70	0.70
Internal Losses α_i (cm^{-1})	8.30	8.30	8.30	9.83	9.83
Mirror Losses α_m (cm^{-1})	23.2	30.8	41.8	23.2	41.8

Table 4- 1 Measured laser diode parameters

4.5.2 Spectral Characterization.

In Section 3.5.2 it was stated that narrowing of the optical spectrum was one the criteria necessary to conclude laser action. Figure 4.9 shows three emission spectra from a device with a cavity length of 530μm and a stripe width of 20μm. Each individual spectra is parameterized by a particular drive current. It is noted that the spectra are plotted on a semilogarithmic plot to allow comparsion of above and below threshold data on the same graph. The data in this graph conclusively shows that a narrowing of the laser linewidth occurs when the device is brought above threshold. It is important to note that the spacing between peaks on spectra shown is typically 1.33nm, these peaks are therefore not the individual cavity modes. The wavelength spacing between adjacent longitudinal modes in a 1mm long device emitting at λ = 980nm, was previously shown to be 0.13nm (Section 2.4). Figure 4.10 is simply the spectrum measured at I=2×I_{th}, re-plotted using a linear intensity scale to allow an estimation of the laser linewidth to be made. The full width at half maximum (FWHM) of the wavelength spectrum at this bias current was 0.6nm.

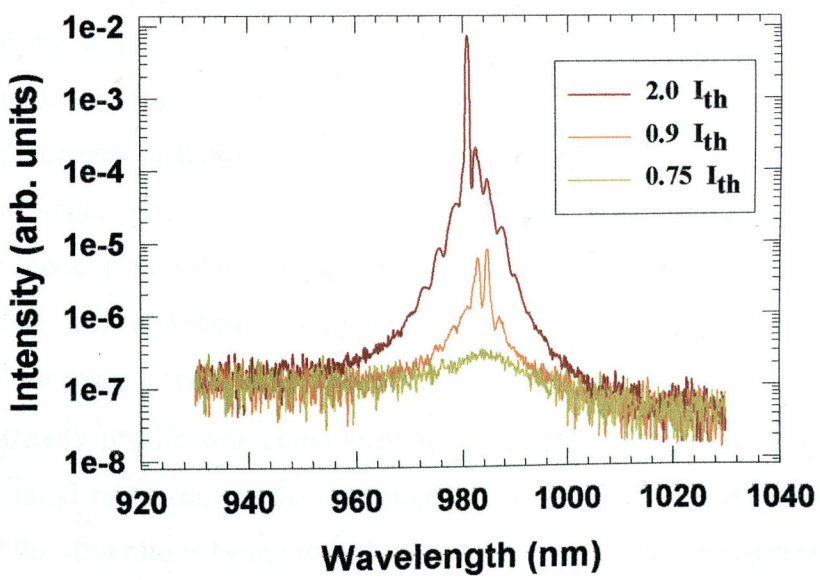

Figure 4-9 Semi logarithmic plot of the wavelength spectrum as wavelength parameterised by drive current.

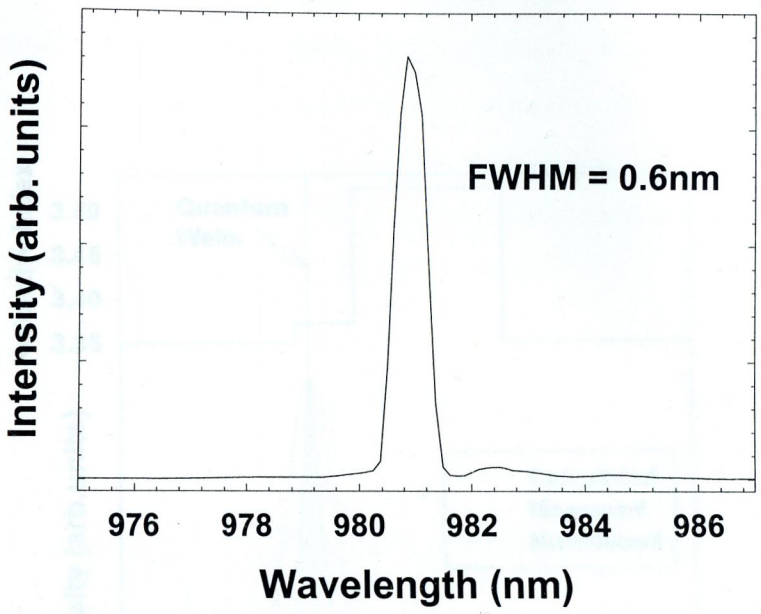

Figure 4-10 Linear plot of wavelength spectrum at twice threshold.

4.5.3 Nearfield Measurements.

The results of the measurements presented so far have clearly demonstrated lasing action in these Lo-guide structures. Further as in the case of the optically pumped structures the low threshold currents of these devices, indicates that these structures are lasing in their highest order mode. This is inferred because the confinement factor (3.66%) of the highest order mode is an order of magnitude greater than confinement factor of the other modes. Figure 4.11 confirms this hypothesis by demonstrating excellent agreement between the measured (red) and calculated (black) intensity profiles. Again the calculated intensity profile was convoluted with a 1 μm Gaussian (green) to take into account the spatial resolution of the measurement setup. From these measurements we conclude that the structure is lasing in its highest order mode in the transverse direction.

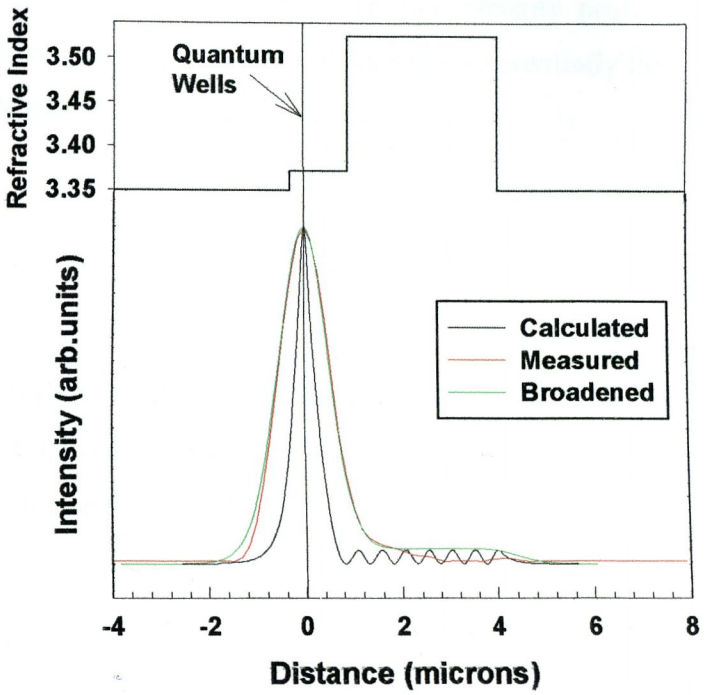

Figure 4-11 Calculated (black) Measured (red) and Broadened (Green) transverse intensity profiles of the electrically pumped asymmetric Lo-guide structure

4.5.4 Farfield Measurements.

It was previously mentioned that waveguiding structures are commonly employed in laser diodes to control the spatial distribution of light in these devices. The electric field profiles in these devices are assumed to be uniform along the entire length of the cavity, so long as the cross section of the waveguiding structure remains constant. However as the light is emitted from the laser waveguide the effects of diffraction modify the emission pattern. At distances greater than, d^2/λ, away from the facet [7], the diffracted

optical field is commonly referred to as the *farfield* emission pattern, where, d, is the width of the emission aperture. Unlike nearfield profiles, farfield distributions are usually plotted in terms of the angular deviation of the emission pattern from the normal to the facet. As the dimensions of the emission aperture are generally different in the transverse and lateral directions the farfield distributions in these direction are also different. Since in most applications it is desirable to capture as much of the output laser light as possible, it is useful to be able to predict intensity profile of the beam as it extends beyond the output facet. The farfield pattern is essentially the Fourier integral of the electric field distribution propagating in the laser waveguide.

$$E_x(\theta) = \int_{-\infty}^{\infty} E_x(y,0)\exp(i\theta y)dy \qquad 4.16$$

However in order to allow a more straightforward comparison with experiment, it is more useful to relate the transverse nearfield electric field profile, $E_x(y,0)$, with the normalized farfield intensity distribution [8], $I(\theta)/I(0)$.

$$\frac{I(\theta)}{I(0)} = \frac{\cos^2\theta\left|\int_{-\infty}^{\infty} E_x(y,0)\exp(i\sin\theta k_0 y)dy\right|^2}{\left|\int_{-\infty}^{\infty} E_x(y,0)dy\right|^2} \qquad 4.17$$

Since it is the farfield intensity distribution that is measured experimentally. In the previous section the nearfield transverse intensity profile of electrically pumped asymmetric Lo-guide was compared with the calculated intensity profile of the structure's highest order mode. Here the measured and calculated farfield distributions from devices operating above threshold are compared. The device used in these measurements was a 20μm stripe device with cavity length of 956μm. Figure 4.12 shows the measured farfield distribution in the transverse direction (orange trace), and the expected farfield distribution from the structure's highest order mode (dark red trace).

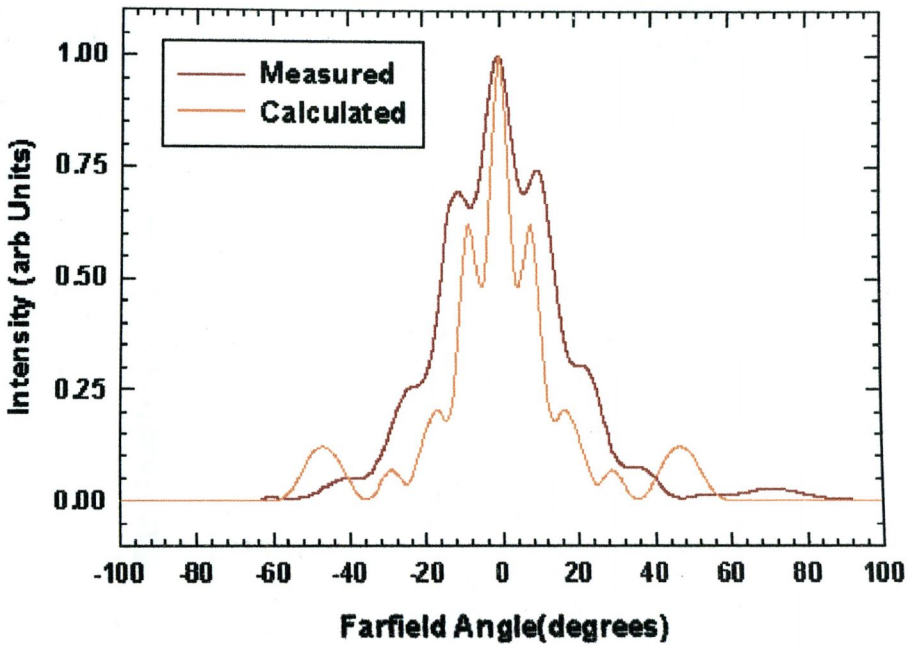

Figure 4-12 Measured (dark-red) and calculated (orange) farfield intensity distributions of the electrically pumped asymmetric Lo-guide.

This plot shows the measure and calculated farfield intensity distributions have the same general features. Although the calculated farfield distribution is significantly narrower than the measured profile, this farfield pattern eliminates any doubt about which mode is lasing. Another characteristic which is desirable in a high power laser device is beam stability. Any changes in the farfield distribution pattern with increasing output power, makes the devices unsuitable for coupling into optical fibres. To investigate the beam stability of these devices the farfield pattern was plotted for different bias currents. Figure 4.13 shows farfield intensity distribution remains stable at bias currents up to 1Amp

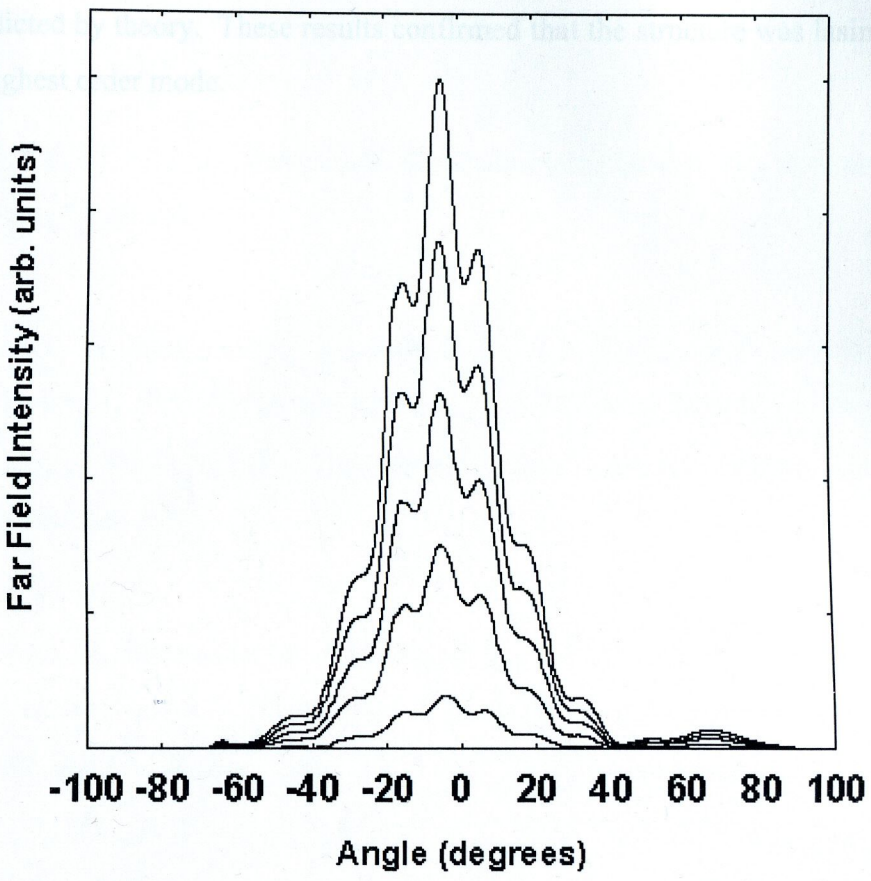

Figure 4-13 Transverse farfield intensity distributions at bias currents of 200mA, 400mA, 600mA, 800mA and 1000mA.

4.6 Summary.

This Chapter has been concerned with the electrical and optical characterisation of an electrically pumped Lo-guide laser diode device under pusedo-CW conditions. Extensive measurements were made of the emitted power versus electrical current for two stripe

widths and three different cavity lengths. From these results values for the internal quantum efficiency, η_i, and the internal losses, α_i, for these structures were determined. Wavelength spectra were measured as a function of bias current to ensure that they were consistent with laser emission. The main function of the measurements mentioned thus far was to demonstrate that these devices didn't exhibit any anomalous behavior. Once this was done the nearfield and farfield emission patterns were measured and compared with what was predicted by theory. These results confirmed that the structure was lasing exclusively in its highest order mode.

4.7 References.

1 R.G. waters, D.S. Hill, and S.L. Yellen. Efficiency enhancement in quantum well lasers via tailoring doping profiles. *Appl. Phys. Lett.,* vol: 52, pp 2017-2018, 1988.

2 L. A. Coldren and S. W. Corzine. *Diode lasers and photonic integrated circuits.* Microwave and optical engineering. Wiley, 1995 Chapter 2

3 G.P. Agrawal and N.K. Dutta. *Long Wavelength Semiconductors Lasers*. Van Nostrand Reinhold Company Inc. Chapter 6.

4 D. Botez, L.J. Mawst, A. Bhattacharya, J. Lopez, J. Li, T.F. Kuech, V.P. Iakovlev, G.I. suruceanu, A. Caliman, A.V. Syrbu and J.Morris. 6W CW front facet power from short cavity (0.5), 100μm stripe Al-free 0.98μm emitting diode lasers. *Electron. Lett.* 33(24) 2037-2039, November 1997.

5 D. Botez, L.J. Mawst, A. Bhattacharya, J. Lopez, J. Li, T.F. Kuech, V.P. Iakovlev, G.I. suruceanu, A. Caliman and A.V. Syrbu. 66% CW wallplug efficiency from Al-free 0.98μm emitting diode lasers. *Electron. Lett.* 32(21) 2012-2013, November 1997.

6 W.T. Tsang. The effects of lateral current spreading, carrier out-diffusion, and optical mode losses on the threshold current density of GaAs/AlGaAs stripe geometry DH lasers. *J. Appl. Phys*., 49(3), March 1978.

7 L. A. Coldren and S. W. Corzine. *Diode lasers and photonic integrated circuits.* Microwave and optical engineering. Wiley, 1995. Appendix 3

8 H.C. Casey, Jr. and M.B. Panish. Heterostructure Lasers Part A. Fundamental Principles. Academic Press 1978. Section 2.7

Chapter 5

Numerical Simulation of a Lo-Guide type Ridge Waveguide Structure.

5.1 Introduction.

Having proved the novel waveguide concept in the transverse direction, the Lo-guide design concept was now implemented in the transverse and in the lateral direction as was originally envisaged. The main focus of this chapter is the design of such structures by performing numerical stimulations. A computer program (Appendix 3) was written to perform this task. The primary aim of this work was to demonstrate that by using an appropriate pumping scheme, it is possible to selectivity excite the highest order mode of such a structure. The rationale behind the use of such a device is to provide coherent single spatial mode emission across broad aperture. Other structures which achieve coherent emission across a broad aperture are ARROW structures and MOPA's (Section 2.11.3). It will be shown that by implementing the symmetric Lo-guide concept in the lateral direction, in the from of a ridge structure, and partially restricting the injection current to flowing through the low effective index region, that it is possible to selectively excite the highest order mode of this structure.

In this section we will outline the difficulties, which make realizing waveguide structures in the lateral direction far more challenging than in the transverse direction. The main problem faced in fabricating ridge waveguides structures is that the processing techniques used are not as accurate as the initial MOCVD or MBE growth processes. Particularly challenging is controlling the height of the ridge waveguide structures as this involves the use of etch stops and selective etches. Also changes in effective index profile due to the carrier injection must be taken into account in the lateral direction, as the effective index steps in this direction are much smaller than in the transverse direction. In order to aid in the design of traditional and novel ridge

waveguide laser diodes a dedicated computer program was written to simulate behavior of such devices. This program which incorporated lateral diffraction and carrier diffusion, allowed the waveguiding properties of both gain guided and index guided devices to be investigated. Figure 5.1 shows schematics of the basic device geometries that where modeled. The strong waveguiding effect associated with transverse GRaded INdex Separate Confinement Heterostructure GRINSCH, effectively allows the stimulation of these devices to be reduced to a two dimensional geometry. This means that any parameters relating to this direction need only be calculated once, and are not required to be constantly updated. The two most important parameters in this respect are the transverse confinement factor, Γ_y, and the effective index, n_{eff}, these quantities are both calculated using the procedure described in Sections 3.2.2 and 3.2.3.

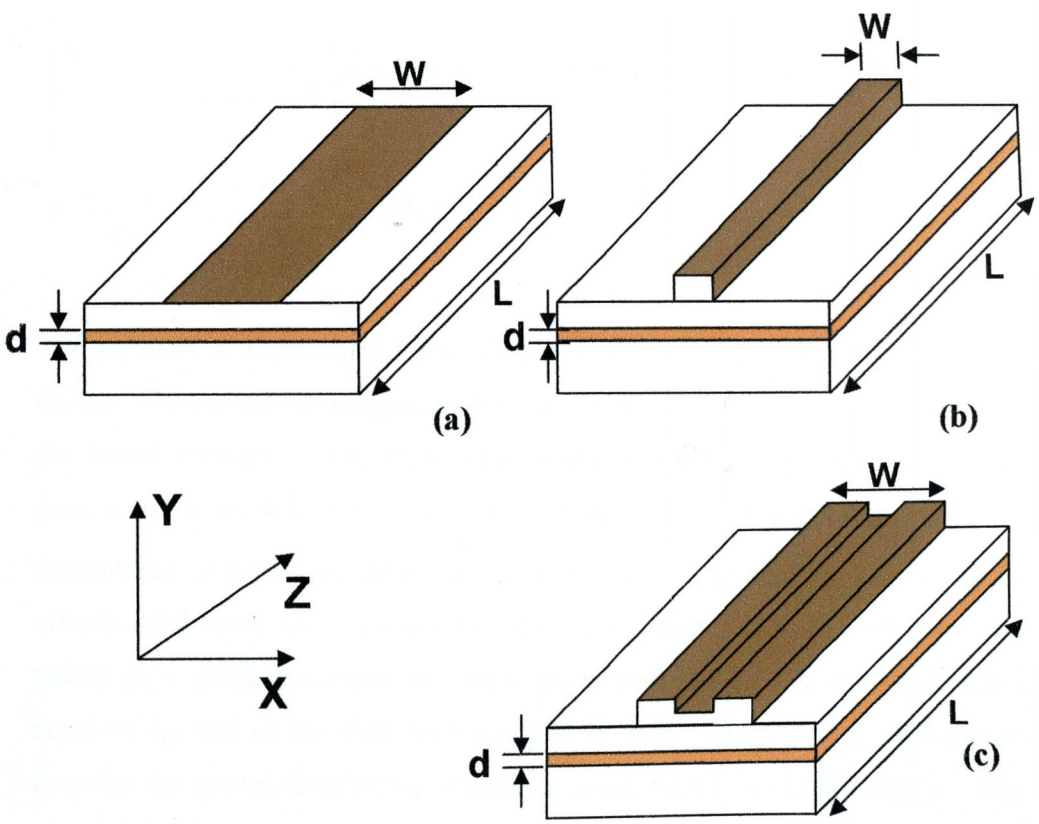

Figure 5-1Illustration of planar stripe device (a) ridge waveguide laser (b) and Lo-guide ridge waveguide laser (c).

In the computer model the optical field within the laser is represented by a forward propagating electric field, u_+, and a backward propagating field, u_-, these fields are amplified or attenuated depending on whether the cavity is above or below threshold. Electron-hole pairs are constantly injected by a current density, *J(x,z)*, through a rectangular stripe of width, *W*. The model can also be adapted to allow for lateral current spreading in layers other than the active region. The carrier distribution that reaches the active region is modified to account for non-radative and stimulated electron-hole recombination, as well as the effects of diffusion within the active region. As the model uses a finite difference method to calculate the lateral carrier distribution, contributions from spontaneous emission to the lasing mode cannot be accounted for. Consequently this model can only predict above-threshold steady state operation and must be seeded with an initial electric field distribution.

The model outlined above can be summarised by the following coupled partial differential equations [1]. Figure 5.4 shows a flowchart which summaries the method of solution.

$$\frac{\partial u_\pm}{\partial z} = \frac{i}{2n_{av}k_0}\frac{\partial^2 u_\pm}{\partial x^2} + \left(\frac{\Gamma}{2}\left[g(N(x,z)) + i2k_0\Delta n(N(x,z))\right] - \alpha_i\right)u_\pm + \left(\frac{ik_0\left[n^2(x) - n_{av}^2\right]}{2n_{av}}\right)u_\pm \qquad 5.1$$

$$D\frac{\partial^2 N(x,z)}{\partial x^2} = -\frac{J(x,z)}{qd} + \frac{N(x,z)}{\tau} + \frac{\Gamma g(N(x,z))}{\hbar\omega}(|u_+|^2 + |u_-|^2) \qquad 5.2$$

The solution of Equation 5.1 reveals the behavior of the optical fields in the laser cavity. The second term in this equation accounts for diffraction of the optical field in the lateral direction. The third term embodies a number of processes within the device, the internal losses, α_i, the carrier dependent material gain, *g(N(x,z))*, and the dependence of refractive index on carrier density. The final term accounts for the effective refractive index variation in the lateral direction. In the simplest case of a purely gain guided structure, the background refractive index, n_{av}, is chosen to be equal to n_{eff} and so the final term equal to is zero. The solutions of Equation 5.2 describe the spatial distribution of carriers *N(x,z)* within the active region. The first term in this equation considers lateral diffusion in the active region, this process is characterized by a diffusion constant, *D*. The second term accounts for the injection

of carriers in to the device, here, $J(x,z)$, is the injected current density, q is the magnitude of the electronic charge, and, d is the thickness of the active region. The third term accounts for non-radative recombination, this process is characterized by a time constant, τ. Finally the last term in Equation 5.2 describes phenomena of stimulated emission and gain saturation in the laser. Before moving on to considering the methods of solution to Equations 5.1 and 5.2, it is worth have a closer look at some of the parameters in these equations.

5.2 Material Parameters.

In order to solve these equations the variation of both the gain and the real part of the refractive index with carrier density must be specified. Full calculations of these functions require solution of the semiconductor Maxwell-Bloch equations and are generally computationally intensive. Therefore phenomenological expressions for the gain and refractive index variation with carrier density are used in this work. A linear variation of gain with carrier density was assumed, i.e. that differential gain, (dg/dN), is constant. In this approach the optical gain as function of carrier density was given by,

$$g(N) = \frac{dg}{dN}(N - N_0) \qquad 5.3$$

where N_0 is the transparency carrier density of the device. The differential gain together with the linewidth enhancement factor, is also used in calculating the variation of the real part of the refractive index with carrier density. The linewidth enhancement (or broadening) factor, R, [2] is defined as follows

$$R = -\frac{d[\mathrm{Re}\{\chi(N)\}]/dN}{d[\mathrm{Im}\{\chi(N)\}]/dN} \qquad 5.4$$

This parameter describes the coupling between carrier-induced variations of the real and imaginary parts of the complex susceptibility. The sign in Equation 5.4 is chosen so that R is positive at semiconductor laser wavelengths. In most practical cases both

the carrier induced contribution to both the refractive and imaginary part of the permittivity are much smaller than the refractive index in the absence of carriers, in this case Equation 5.4 is equivalent to Equation 5.5 [3],

$$R = -2k_0 \frac{dn/dN}{dg/dN} \qquad 5.5$$

In the model the change in the real part of the refractive index as a function carrier density is therefore given by,

$$\Delta n(N(x,z)) = -\left(\frac{dg}{dN}\right)\frac{R}{2k_0}N(x,z) \qquad 5.6$$

5.3 The Finite Difference Beam Propagation Model.

The beam propagation model (BPM) [4] is a particular approach for approximating the wave equation for monochromatic waves, and solving the resulting equations numerically. In this method the electric field is propagated along a rectilinear grid, as shown in Figure 5.2. The efficiency and flexibility of this technique have made it the most widely used in the field of integrated optics. It is therefore the method of choice for solving Eqautions 5.1 and 5.2. In the scalar paraxial BPM, the effects of polariasation are neglected and the direction of propagation is restricted to a narrow range of angles around the axis of the waveguide. Starting from the scalar form of Helmholtz equation:

$$\frac{\partial^2\phi}{\partial x^2}+\frac{\partial^2\phi}{\partial y^2}+\frac{\partial^2\phi}{\partial z^2}+k_0{}^2n^2(x,y,z)\phi = 0 \qquad 5.7$$

where the scalar electric field has been written in the form $E(x,y,z,t) = \phi(x,y,z)e^{-i\omega t}$ The refractive index distribution $n(x,y,z)$ completely defines, the geometry of the problem. In the case of a laser diode this term includes both the real and the imaginary parts of the refractive index. Apart from the scalar approximation Equation 5.7 is completely exact. In guided wave problems the most rapid variation in the field

ϕ is phase variation to propagation along the guiding axis, assuming this axis is in the z direction these rapid variations can be factor out, by writting.

$$\phi(x,y,z) = u(x,y,z)e^{i\beta z} \qquad 5.8$$

Where u is the so-called slowly varying field and β is the reference propagation constant, which is chosen to represent the average phase variation of the field. The reference propagation constant can be expressed in terms of a reference refractive index, n_{av}:

$$\beta = k_0 n_{av} \qquad 5.9$$

Substituting Equation 5.8 into the Helmholtz equation yields the following:

$$\frac{\partial^2 u}{\partial z^2} + 2i\beta\frac{\partial u}{\partial z} + \frac{\partial^2 u}{\partial x^2} + \frac{\partial^2 u}{\partial y^2} + \left(k^2 n^2(x,y,z) - \beta^2\right)u = 0 \qquad 5.10$$

Further if the variation of u with z is sufficiently slow then the first term in Equation 5.10 maybe neglected. The omission of this term allows the Equation 5.10 to be rewritten in the following way

$$\frac{\partial u}{\partial z} = \frac{i}{2\beta}\left(\frac{\partial^2 u}{\partial x^2} + \frac{\partial^2 u}{\partial y^2} + \left(k^2 n^2(x,y,z) - \beta^2\right)u\right). \qquad 5.11$$

With this assumption made the problem reduces to what is known as the paraxial approximation. It is important to realize that this simplification has not come without a price, as paraxial approximation is limited to considering fields that propagate primarily along the z-axis. One further consequence is that it also places restrictions on the index gradients in the longitudinal directions. One way around this problem involves the use of Pade approximant operators [5] [6], however this approach is not employed here. Equation 5.11 is the basic equation for the beam propagation in three

dimensions, in two dimensional problems the, $\partial^2 u/\partial y^2$, term vanishes as there is no dependency on y.

$$\frac{\partial u}{\partial z} = \frac{\iota}{2\beta}\left(\frac{\partial^2 u}{\partial x^2} + \left(k_0{}^2 n^2(x,y,z) - \beta^2\right)u\right) \qquad 5.12$$

Given an input field $u(x,z = 0)$, Equation 5.12 describes its evolution along the positive sense of the z-axis. In early BPM's a split step Fourier method [7] was used to propagate the field however later work [8] showed a finite difference (FD) method was superior for most problems in integrated optics. The FD-BPM as it is sometimes referred to, uses the well known Crank-Nicholson [9] scheme to propagate the electric field along a rectilinear grid. In order to develop a FD method for solving Equation 5.12 we generalize that equation as follows

$$\frac{\partial u}{\partial z} = A(x,z)\frac{\partial^2 u}{\partial x^2} + B(x,z)u\,. \qquad 5.13$$

In a laser diode the parameters A and B are represented by the following expressions

$$A = i/2\beta \qquad 5.14$$

$$B = \frac{\Gamma}{2}[g(N(x,z) + i2k_0\Delta n(N(x,z))] + \frac{i\left(k_0^2 n^2 - \beta^2\right)}{2\beta} - \alpha_i\,. \qquad 5.15$$

Using these expressions for A and B, Equation 5.13 is now equivalent to Equation 5.1. The notation, $u_s^r = u(x_s, z_r)$ is used to describe the field at each point on the grid, where $x_s = s\Delta x$ and $z_r = r\Delta z$. Figure 5.2 shows a section of the grid, which the field propagates along.

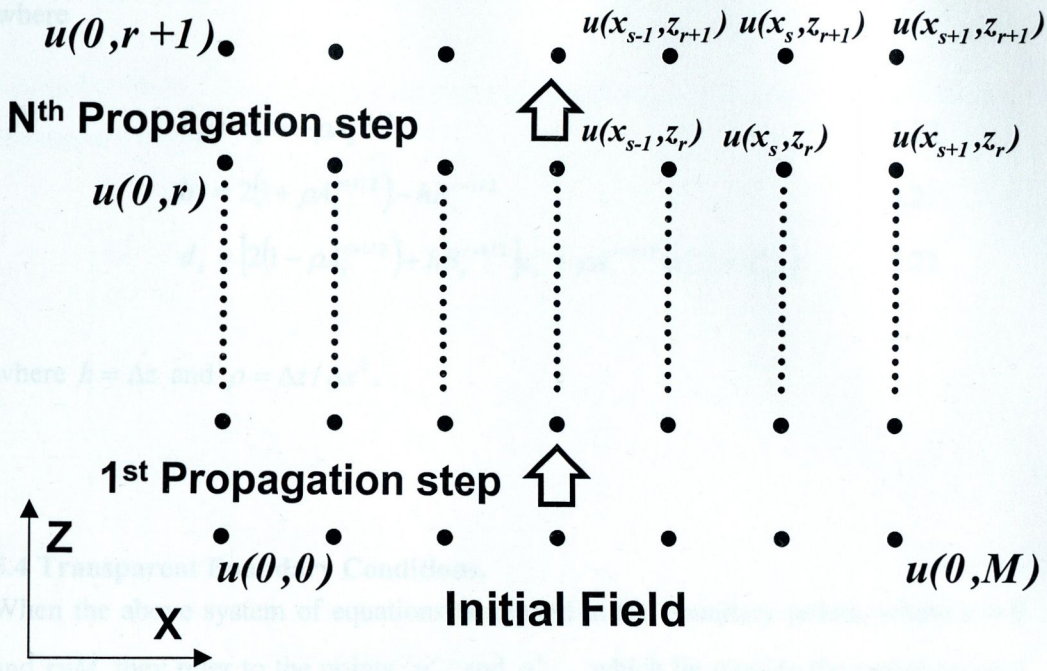

Figure 5-2 Propagation step along a two dimensional grid.

To discretize Equation 5.13, a Crank-Nicholson finite difference scheme is followed, this involves rewriting each term as shown.

$$\frac{\partial u}{\partial z} \rightarrow \frac{u_s^{r+1} - u_s^r}{\Delta z} \qquad 5.16$$

$$A\frac{\partial^2 u}{\partial x^2} \rightarrow \frac{1}{2}\left\{\frac{u_{s-1}^r - 2u_s^r + u_{s-1}^r}{\Delta x^2} + \frac{u_{s-1}^{r+1} - 2u_s^{r+1} + u_{s+1}^{r+1}}{\Delta x^2}\right\} A_s^{r+1/2} \qquad 5.17$$

$$Bu \rightarrow \frac{1}{2}\left\{u_s^r + u_s^{r+1}\right\} B_s^{r+1/2} \qquad 5.18$$

In this approach the parameters A and B are evaluated at the fictitious half step $(s,r+1/2)$, in practice though these values don't change much along the length of the cavity. If the expressions 5.16, 5.17 and 5.18 are inserted into Equation 5.13, the following system of equations is obtained,

$$a_s u_{s-1}^{r+1} + b_s u_s^{r+1} + c_s u_{s+1}^{r+1} = d_s \qquad s = 0, \rightarrow M \qquad 5.19$$

where

$$a_s = c_s = -\rho A_s^{r+1/2} \qquad 5.20$$

$$b_s = 2\left(1 + \rho A_s^{r+1/2}\right) - hB_s^{r+1/2} \qquad 5.21$$

$$d_s = \left[2\left(1 - \rho A_s^{r+1/2}\right) + hB_s^{r+1/2}\right] u_s^r + \rho A_s^{r+1/2}\left(u_{s-1}^r + u_{s+1}^r\right) \qquad 5.22$$

where $h = \Delta z$ and $\rho = \Delta z / \Delta x^2$.

5.4 Transparent Boundary Conditions.

When the above system of equations is applied at the boundary points, where $s = 0$ and $s=M$, they refer to the points, u_{-1}^r and u_{M+1}^r, which lie outside the computational domain. To obtain appropriate values for the field at these points and we must apply boundary conditions to the problem. Choosing the right type of boundary conditions is essential, since a poor choice will lead to artificial reflections at the computational boundary. One type of boundary condition commonly used in BPM problems is the so-called transparent boundary conditions (TBC)[10] [11]. Consider the boundary at $x = 0$, and propagation step from $z = r\Delta z$ to $z = (r+1)\Delta z$. At this boundary the quantity $k_{x,l}$ can be determined from the equation,

$$\exp\left(ik_{x,l}\Delta x\right) = \frac{u_0^r}{u_1^r}, \qquad 5.23$$

which relates the field at the boundary and the adjacent interior point. A value for $k_{x,r}$ is obtained in a similar fashion on the right hand side of the grid. It is assumed that the values of $k_{x,l}$ and $k_{x,r}$ are constant near computational boundaries. Therefore using $k_{x,l}$ and $k_{x,r}$, the field at the fictitious exterior points u_{-1}^{r+1} and u_{M+1}^{r+1} can be written in terms of the field at the boundary points u_0^{r+1} and u_M^{r+1}, as follows:

$$u_{-1}^{r+1} = u_0^{r+1}\exp\left(ik_{x,l}\Delta x\right) \quad 5.24$$

$$u_{M+1}^{r+1} = u_M^{r+1}\exp\left(ik_{x,r}\Delta x\right). \quad 5.25$$

Using Equation 5.24 and 5.25, the System of Equations 5.19 can now be rewritten in tridiagonal from,

$$\begin{bmatrix} b_0^* & c_0 & \cdots & & & \\ a_1 & b_1 & c_1 & \cdots & & \\ & & & \cdots & & \\ & & & \cdots & a_{M-1} & b_{M-1} & c_{M-1} \\ & & & \cdots & & a_M & b_M^* \end{bmatrix} \cdot \begin{bmatrix} u_0^{r+1} \\ u_1^{r+1} \\ \cdots \\ u_{M-1}^{r+1} \\ u_M^{r+1} \end{bmatrix} = \begin{bmatrix} d_0 \\ d_1 \\ \cdots \\ d_{M-1} \\ d_M \end{bmatrix} \quad 5.26$$

Where

$$b_0^* = a_0\exp\left(ik_{x,l}\Delta x\right) + b_0 \quad 5.27$$

$$b_M^* = c_M\exp\left(ik_{x,r}\Delta x\right) + b_M \quad 5.28$$

Each propagation step involves solving the above system of equations. The computational efficiency of the BPM is due to the fact that the above system of equations is written in tridiagonal format, since such systems can be solved in *O(M)* operations [12]. The mathematical representation of the optical field in the laser cavity is now almost complete, to complete this picture reflections which occur at laser facets must be accounted for.

5.5 Facet Reflectivity Boundary Conditions.

Equations 5.29 and 5.30 describe the reflections which occur at, $z = 0$, and, $z = L$, in the laser model. The reflection coefficients, r_1, and, r_2, determine the amount of light which is reflected back into the cavity at each interface. They also therefore determine the amount of light, which escapes from the cavity at each interface. Figure 5.3 illustrates the reflections that the forward and backward propagating beams

experience at the laser facets. A typical longitudinal intensity profile for a device with uncoated facets is also shown

$$u_+(x, z=0) = -\sqrt{r_1}u_-(x, z=0) \qquad 5.29$$

$$u_-(x, z=L) = -\sqrt{r_2}u_+(x, z=L) \qquad 5.30$$

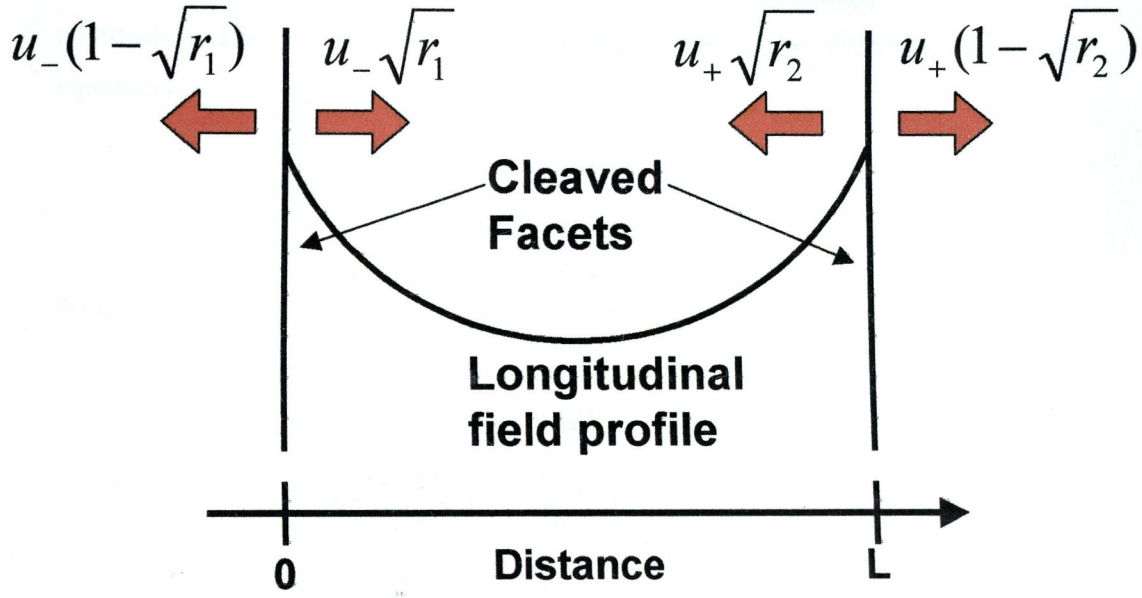

Figure 5-3 Illustration of the electric field distribution in a laser with uncoated facets.

5.6 Electronic Carrier Diffusion Equation.

The distribution of carriers in a laser diode can be accounted for by solving the diffusion Equation 5.31 [1],

$$D\nabla^2 N(\mathbf{r}) = -\frac{J(\mathbf{r})}{qd} + \frac{N(\mathbf{r})}{\tau} + \frac{g(N(\mathbf{r}))}{\hbar\omega}|\mathbf{E}(\mathbf{r})|^2 \qquad 5.31$$

This is a more general form of Equation 5.2, in that here we dealing with a distribution of carriers in three dimensions. Equation 5.31 can be made equivalent to Equation 5.2 by making the following assumptions. The first of these is that the

carrier density is uniform over the thickness of the active region. This is quite reasonable since its dimension is small (~ 0.008μm) compared to the diffusion length, This assumption allows the y-dependence of the current and carrier density to be neglected. The second assumption is that longitudinal spatial hole-burning is washed out due to carrier diffusion. Thirdly it is assumed that axial variations of the carrier density occur over length scales much longer than the diffusion length and so the second derivative of N with respect to z may also be neglected. Finally the confinement factor, Γ, accounts for the fact that the optical field extends beyond the active region. Equation 5.2 can also be solved numerically using a finite difference approach. The discretization of Equation 5.2 yields the following system of equations.

$$aN_{i-1} + bN_i + cN_{i+1} = d_i \qquad i = 1, \rightarrow M-1 \qquad 5.32$$

Where

$$a = c = D/\Delta x^2 \qquad 5.33$$

$$b = -\left(\frac{2D}{\Delta x^2} + \frac{1}{\tau} + \frac{\Gamma g_{diff}}{\hbar\omega}(|u_+|^2 + |u_-|^2)\right) \qquad 5.34$$

$$d = -\left(\frac{J_i}{qd} + \frac{\Gamma g_{diff} N_0}{\hbar\omega}(|u_+|^2 + |u_-|^2)\right) \qquad 5.35$$

In the Equation Set 5.32 the differential operator $\partial^2 N(x,y)/\partial x^2$ in Equation 5.2 has been replaced by,

$$\frac{N_{i-1} - 2N_i + N_{i+1}}{\Delta x^2} \qquad 5.36$$

Again when the above system of equations is applied at the boundary points, $i = 0$ and i=M, they refer to the quantities, N_{-1} and N_{M+1}, which lie outside the computational domain. To obtain appropriate values for the field at these points and we must apply boundary conditions to the problem. Considering that Equation 5.2 is of the form

$$D\frac{\partial^2 N}{\partial x^2} + AN = B \qquad 5.37$$

it is assumed that as

$$x \to \pm\infty, \quad N \to \exp\left(-\sqrt{A/D}\, x\right). \qquad 5.38$$

This means the appropriate boundary conditions can be written as follows

$$N_{-1} = N_0 \exp\left(-\sqrt{\frac{A_0}{D}}\Delta x\right) \qquad 5.39$$

$$N_{M+1} = N_M \exp\left(-\sqrt{\frac{A_0}{D}}\Delta x\right) \qquad 5.40$$

Using these conditions it is now possible to write the Equations Set 5.32 in tridiagonal form

$$\begin{bmatrix} b_0^* & c_0 & & \cdots & & & \\ a_1 & b_1 & c_1 & \cdots & & & \\ & & & \cdots & & & \\ & & & \cdots & a_{M-1} & b_{M-1} & c_{N-1} \\ & & & \cdots & & a_M & b_M^* \end{bmatrix} \cdot \begin{bmatrix} N_0 \\ N_1 \\ \cdots \\ N_{M-1} \\ N_M \end{bmatrix} = \begin{bmatrix} d_0 \\ d_1 \\ \cdots \\ d_{M-1} \\ d_M \end{bmatrix} \qquad 5.41$$

where

$$b_0^* = b_0 \exp\left(-\sqrt{\frac{A}{D}}\Delta x\right) + b_0 \qquad 5.42$$

$$b_M^* = b_M \exp\left(-\sqrt{\frac{A}{D}}\Delta x\right) + b_M \qquad 5.43$$

Since the two dimensional carrier diffusion equation can also be written in tridiagonal form, it to can also be solved in *O(N)* operations. This completes the mathematical framework necessary to simulate the characteristics of the devices discussed in Section 5.1

5.7 Normalization.

The previous subsections have detailed the methods of solution for Equations 5.1 and 5.2. However before carrying out a numerical solution, the variables in these equations were normalized to suit the natural dimensions of the problem. The normalization scheme used here is similar to that followed by Adachihara et al [13], in their investigation of spatiotemporal chaos in broad area lasers. In the following equations all normalized dimensionless variables are denoted by primes.

$$z' = \frac{z}{L} \qquad 5.44$$

$$x' = \frac{x}{W} \qquad 5.45$$

$$N' = \frac{N}{N_0} \qquad 5.46$$

$$\tau' = \frac{c}{n_{av}L}\tau \qquad 5.47$$

$$D'_{opt} = \frac{L}{2n_{av}k_0W^2} \qquad 5.48$$

$$\kappa' = \left(\frac{dg}{dN}\right)\frac{N_0 L}{2} \qquad 5.49$$

$$R' = 1 - 2iR \qquad 5.50$$

$$\alpha'_i = \alpha_i L \qquad 5.51$$

$$\Delta = \frac{ik_0L(n_{eff}(x) - n_{av}^2)}{2n_{av}} \qquad 5.52$$

$$D' = \frac{Dn_{av}L}{cW^2} \qquad 5.53$$

$$J' = \frac{Jn_{av}L}{cN_0qd} \qquad 5.54$$

$$(|u'_+|^2 + |u'_-|^2) = \left(\frac{dg}{dN}\right)\frac{n_{av}L}{c\hbar\omega}(|u_+|^2 + |u_-|^2) \qquad 5.55$$

These expressions allow Equations 5.1 and 5.2 to be re-written in dimensionless form, as follows.

$$\frac{\partial u'_\pm}{\partial z'} = iD'_{opt}\frac{\partial^2 u'_\pm}{\partial x'^2} + \left[\kappa\Gamma(R'N' - 1) - \alpha'_i + \Delta\right]u'_\pm \qquad 5.56$$

$$D'\frac{dN'}{dx'^2} = -J' + \frac{N'}{\tau'} + \Gamma(N' - 1)(|u_+|^2 + |u_-|^2) \qquad 5.57$$

Equations 5.56 and 5.57 can be solved using exactly the same procedure as that used for solving Equations 5.1 and 5.2. It was felt however, that outlining the solutions to Equation 5.1 and 5.2 would allow a more intuitive insight into the problem.

5.8 Overview of Solution.

Finally before moving on to results obtained using the model, it is worth looking at a simple flow chart (Figure 5.4) of the computer program, which was used to solve Equations 5.56 and 5.57.

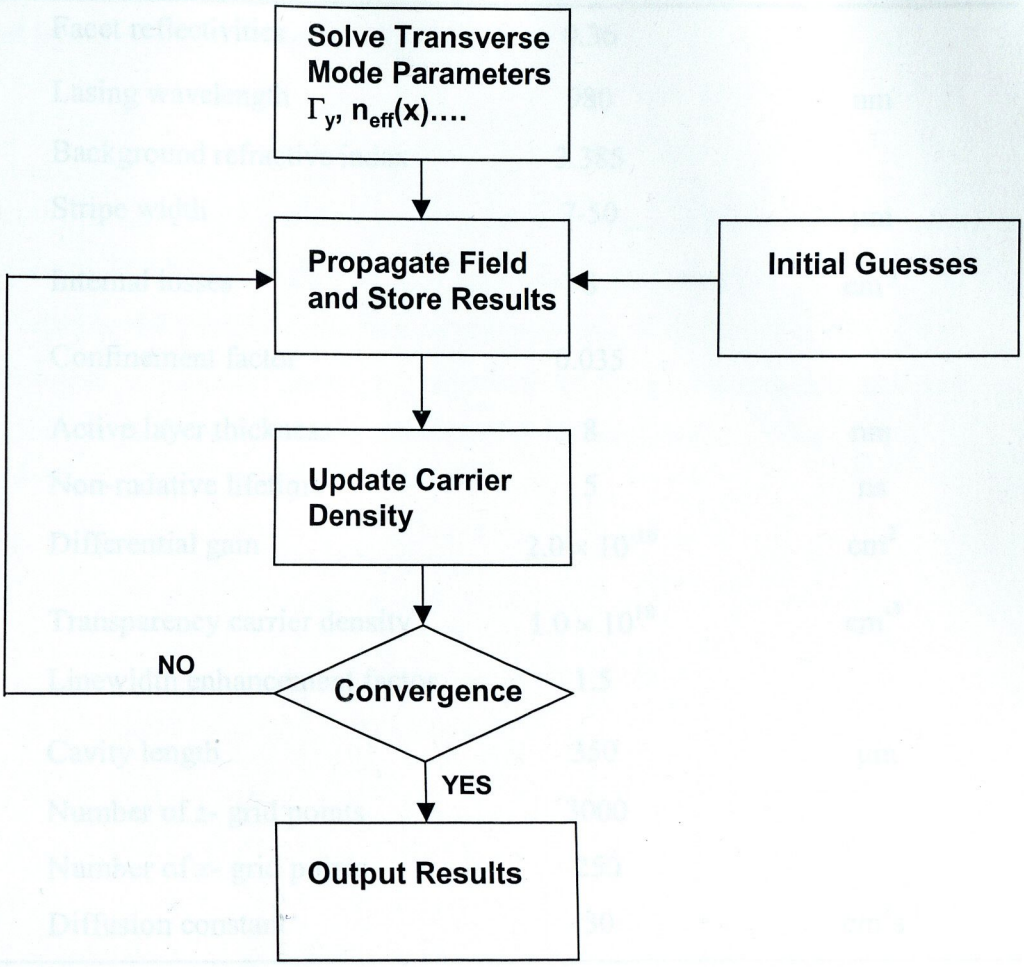

Figure 5-4 Flow chart showing the method of solution for Equations 5.1 and 5.2.

As stated previously all parameters relating to the transverse direction are calculated only once and are not updated during the program. Another prerequisite required before running the BPM proper is an initial field profile, in this case a Gaussian field distribution was used. The electric field distributions, u_+ and u_-, are then propagated back and forth along the cavity. Each time, u_+ and u_-, complete a trip form one end of the cavity to the other, the carrier density is updated. The results produced by the program are only accepted, if the power output from the device stabilizes within a fixed number of cavity passes.

Symbol	Description	Value	Unit
r_1, r_2	Facet reflectivities	0.36	
λ	Lasing wavelength	980	nm
n_{av}	Background refractive index	3.385	
W	Stripe width	7-50	μm
α_i	Internal losses	6	cm^{-1}
Γ	Confinement factor	0.035	
d	Active layer thickness	8	nm
τ	Non-radative lifetime	5	ns
dg / dN	Differential gain	2.0×10^{-16}	cm^2
N_0	Transparency carrier density	1.0×10^{18}	cm^{-3}
R	Linewidth enhancement factor	1.5	
L_z	Cavity length	350	μm
N_z	Number of *z*- grid points	3000	
N_x	Number of *x*- grid points	250	
D	Diffusion constant	30	cm^2s^{-1}

5.9 Results.

In this section we look at the lateral intensity profiles of both conventional and Lo-guide type laser structures, similar to those shown in Figure 5.1 which were generated using the model described above. In the case of the Lo-guide structure the field profiles obtained using two different current distributions, are compared with the lateral intensity profiles obtained using the waveguide effective index method discussed in Section 3.2.3.

5.9.1 Validating the BPM.

However before looking at simulations of laser diodes that incorporate the Lo-guide ridge waveguide structure, it is prudent to validate the model by using it to calculate characteristics of standard laser devices. To this end the light-current characteristic,

as well as the lateral and longitudinal, carrier and intensity profiles of a gain guided device were calculated. For consistency the values used here for parameters such as the internal losses and the linewidth enhancement factor would also be used in the devices incorporating the Lo-guide ridge design.

5.9.2 Analysis of a Standard Gain Guided Device.

The results presented in this section relate to a device with a stripe width of 6μm and cavity length of 350μm. In the case of a gain-guided structure the only parameters which relate to the transverse direction are the thickness of the active region, *d*, and the transverse confinement factor, Γ_y, the values of these quantities are 8nm and 3.55%. We begin by examining the calculated light-current characteristic.

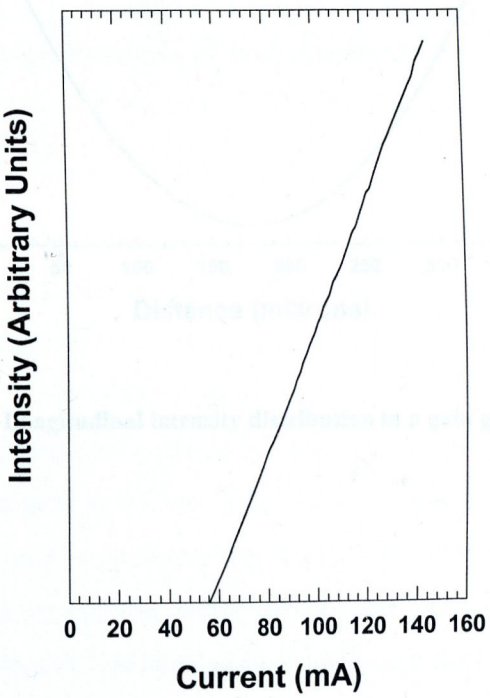

Figure 5-5 Calculated light current characteristic of a 350μm long gain guided device with a stripe width of 6μm.

Figure 5.5 shows the threshold current to be approximately 56mA. It is noted that there are no points on the graph below threshold, this is because the power output from the model never stabilizes when the device is below threshold. This is because if the device is below threshold, the propagating beam is continually attenuated. Therefore the percentage change in the beam power after each sweep of the cavity is always negative. Next the ability of the BPM to calculate the longitudinal carrier and intensity distributions is demonstrated. Figure 5.6 shows the characteristic shape of the optical intensity inside symmetric Fabry-Perot laser cavity

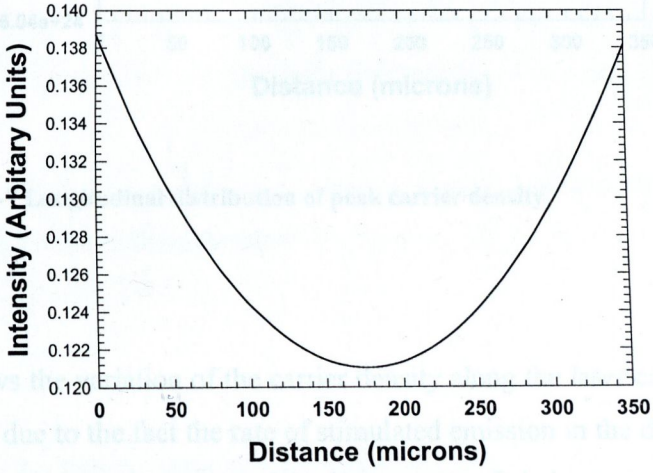

Figure 5-6 Longitudinal intensity distribution in a gain guided laser.

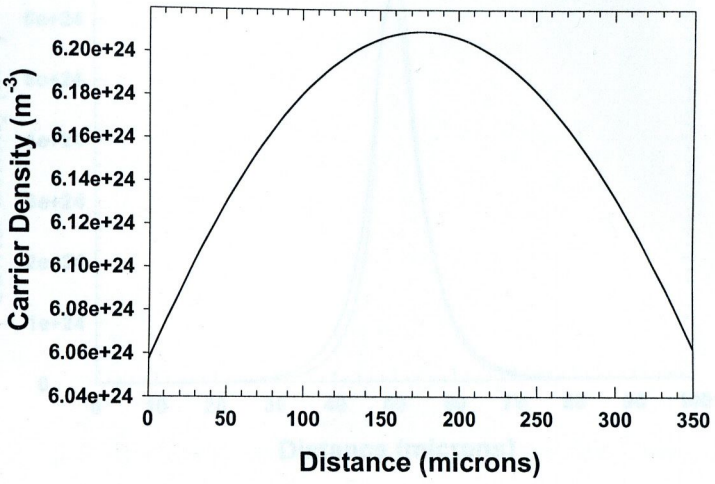

Figure 5-7 Longitudinal distribution of peak carrier density.

Figure 5.7 shows the variation of the carrier density along the laser cavity. The shape of this graph is due to the fact the rate of stimulated emission in the device raises with increasing distance from the center of the laser cavity. It is important to note that the plots in Figures 5.6 and 5.7 are only symmetrical because the facet reflectivity's, r_1 and r_2 are equal. In practice the reflectivies of a laser diodes facets be changed can by coating them with oxides such as SiO or SiN_3. Next we now move on to examining the lateral carrier distributions in the active region. Figure 5.8 shows the lateral carrier distributions in center of the device at 1.1× and 2.8× threshold. It can be inferred from this graph that the BPM reliably predicts that the carrier density clamps at its threshold value.

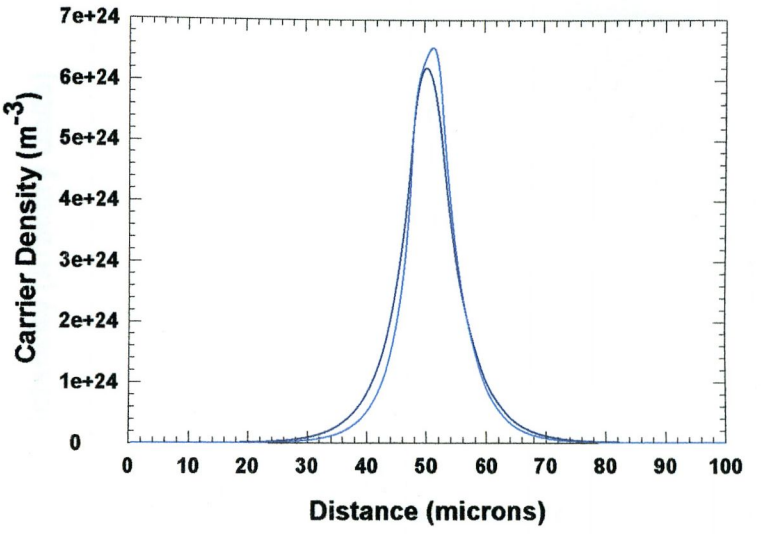

Figure 5-8 Lateral carrier density profile in a gain guided devices at 1.1 (purple) and 2.8 (blue) times threshold

Figure 5.9 shows the lateral intensity distributions at one of the laser facets, at the previously stated operating conditions. As in the case of the lateral carrier distributions, the intensity profile obtained at $1.1\times I_{th}$ is symmetric while the profile obtained at $2.8\times I_{th}$ asymmetric. This demonstrates the ability of BPM to simulate the effects of beam steering, which occurs at high operating currents. Beam steering effects beam stability, this in turn effects the usefulness of the for applications such as fibre coupling. Beam steering is typically caused by carrier induced changes in the refractive index. The intensity profiles in Figure 5.9 have been normalized to unity in order that they may be displayed on the same graph.

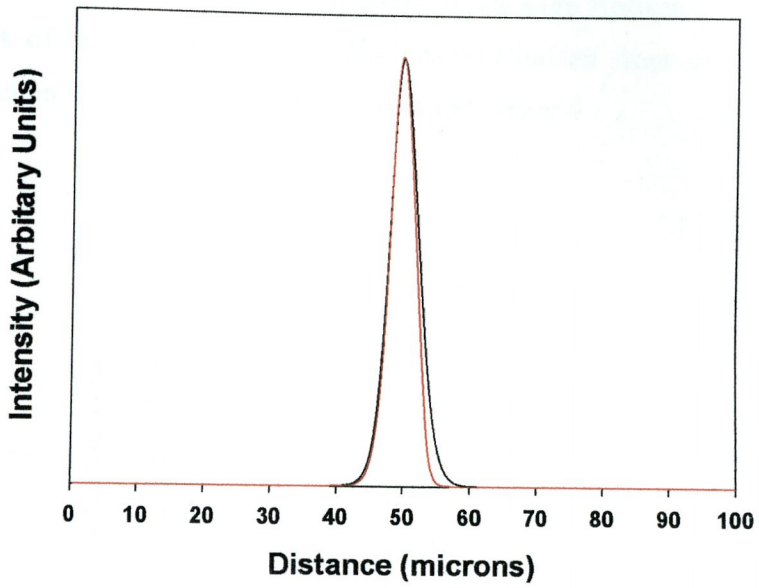

Figure 5-9 Lateral output intensity at 1.1 (black) and 2.8 (red) times threshold for a 6μm gain guided device.

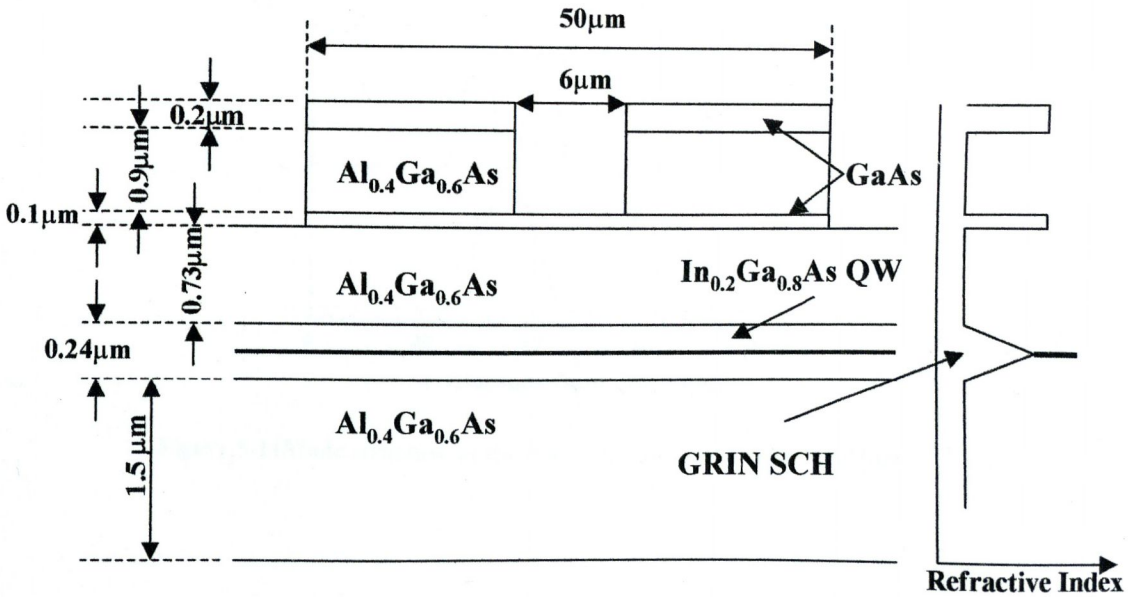

Figure 5-10 Schematic of the symmetric Lo-guide ridge waveguide structure.

5.10 Novel Device Simulations.

Having proved abilities of the BPM by using it to simulate the characteristics of a standard laser diode structure, it is now appropriate to use it to consider the lasing action in the novel Lo-Guide structures. Figure 5.10 shows the epitaxial structure and the dimensions of the ridge waveguide lasers, which were fabricated to investigate the properties of the Lo-guide mode. The results obtained from experimental work carried out on these devices will be presented in Chapter 6.

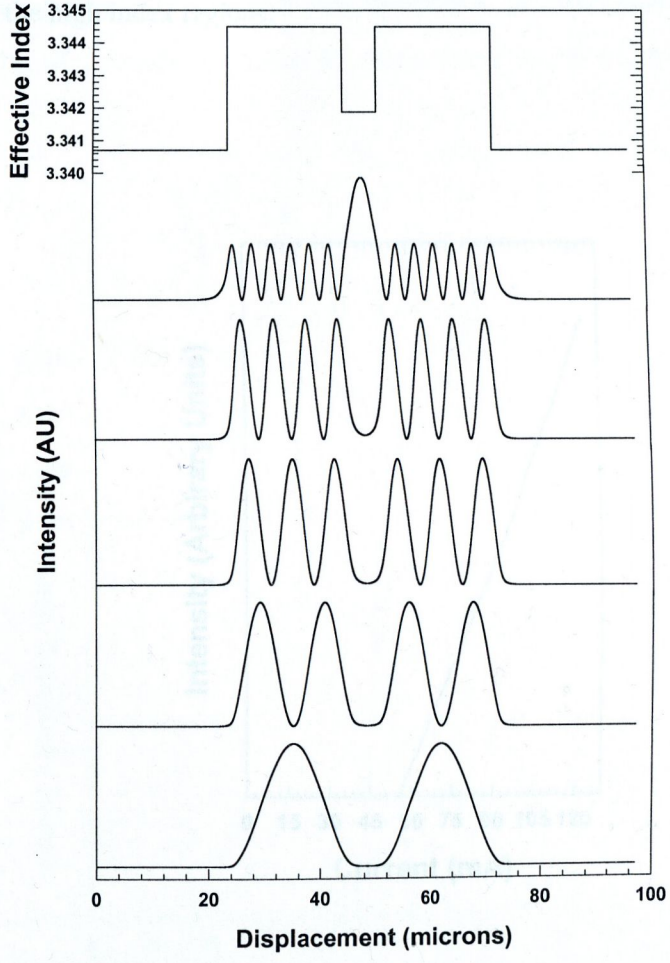

Figure 5-11Mode structure of the symmertic Lo-guide ridge structure.

The case of exclusively pumping the central low index of a 350μm cavity length device, with an epitaxial structure identical to shown in Figure 5.10 is considered first. The calculated light-current characteristic, which would be produced by this device is shown in Figure 5.12. The threshold current of the device is calculated to be approximately 56mA, it is again noted that there are no points on the graph that correspond to below threshold operation. The lateral nearfield intensity profiles were calculated at approximately 1.5mA intervals. However under the current pumping scheme almost no lasing emission is predicted to come from the high effective index regions, over the entire range of the calculated light-current characteristic. This point is illustrated in Figure 5.13, which shows the calculated lateral intensity profile obtained at operating currents of 1.1× and 2.8× threshold. In this figure both intensity profiles are normalized to unity in order to allow them to be compared with one another.

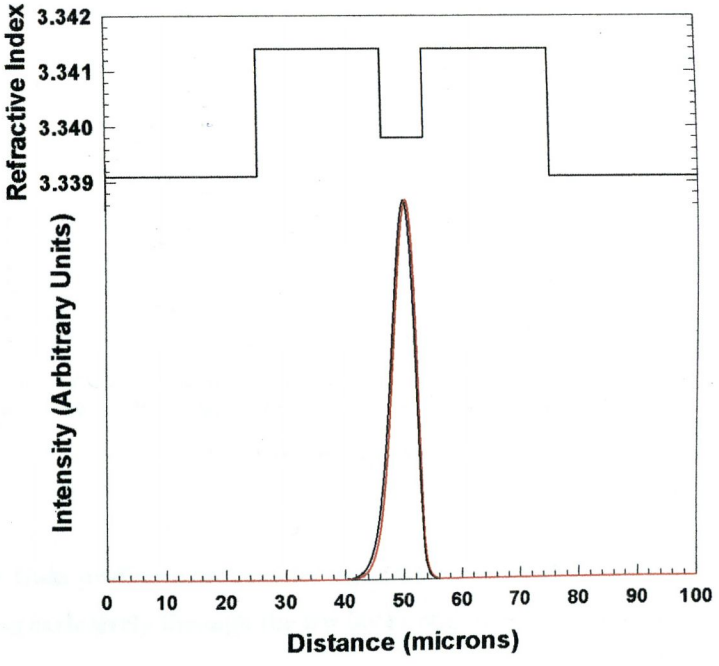

Figure 5-13 Output intensity distributions of a Lo-guide device at bias currents of 1.1(black) 2.8 (red) times threshold.

The reason why the BPM predicts no lasing emission from the high index regions under this pumping scheme, can be understood by considering the lateral gain profiles produced by injected carriers. Figure 5.14 shows the calculated gain profiles for the device, again operating at 1.1× and 2.8× threshold. It can be seen from this graph that the only region of this structure that is pumped above transparency, is a small section directly beneath the low index region. Further by comparison with the calculated nearfield intensity profiles (Figure 5.13), it can be seen that the light output is nearly exclusively from this region.

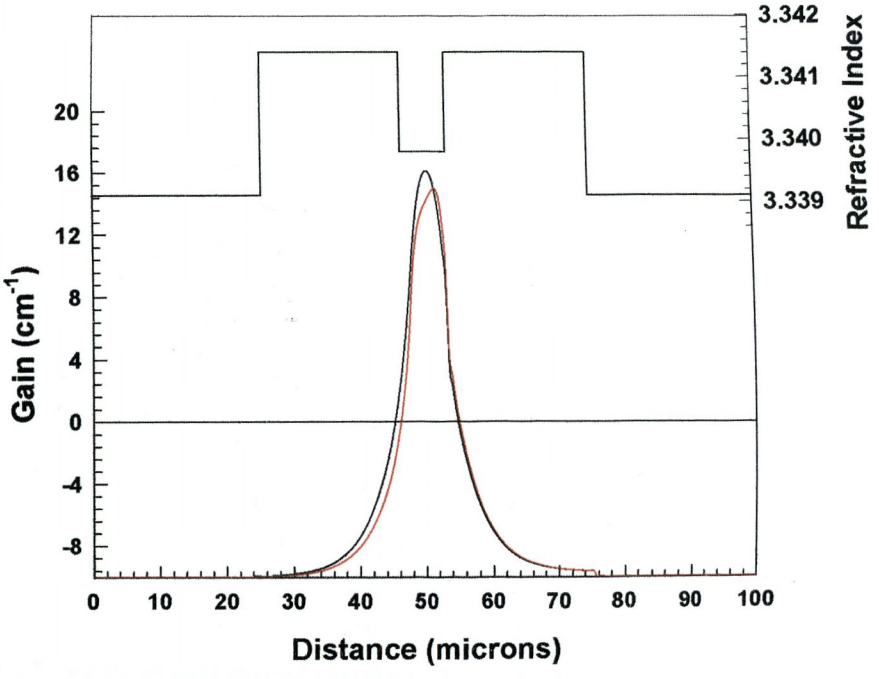

Figure 5-14 Gain profiles produced by injection currents of 1.1 (black) and 2.8(red) times flowing exclusively through the low index region of the structure.

At this point based on of calculations preformed, it was decided to employ an alternative pumping scheme. In this scheme the current density flowing through the high index region was set at one quarter of the value flowing through the low index

region. It is noted that this is not an attempt at optimizing overlap optical field and the active region. Figure 5.15 shows the calculated light-current characteristic obtained using this pumping scheme. It is immediately obvious from looking at this plot that the predicted threshold current of a device being operating under these conditions is much higher than before. This is because at threshold, the carriers being injected through the high index regions are not contributing to useful gain.

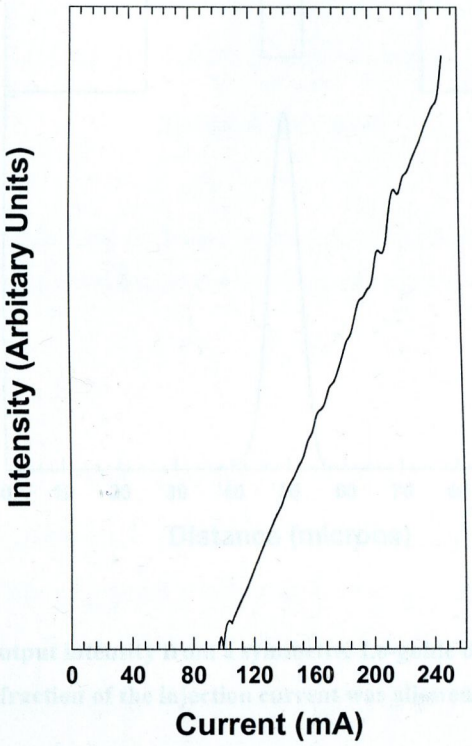

Figure 5-15 Calculated light current characteristic generated by allowing a fraction of the injection current to flow through the high index regions.

We now move on to the calculated lateral intensity produced by the BPM under the new pumping scheme. Figure 5.16 shows the predicted intensity profile from a device operating at 1.1× times threshold. This profile is very similar to what was calculated using the previous pumping scheme. The shape of lateral intensity profile

remains stable over the normalized current interval 1.0× to 1.35× threshold. As the injection current is increased further the BPM predicts some lasing emission from the high index regions, however the emission patterns in these regions change with bias current. The behavior described, characterizes the normalized current interval 1.35× to 1.90× threshold.

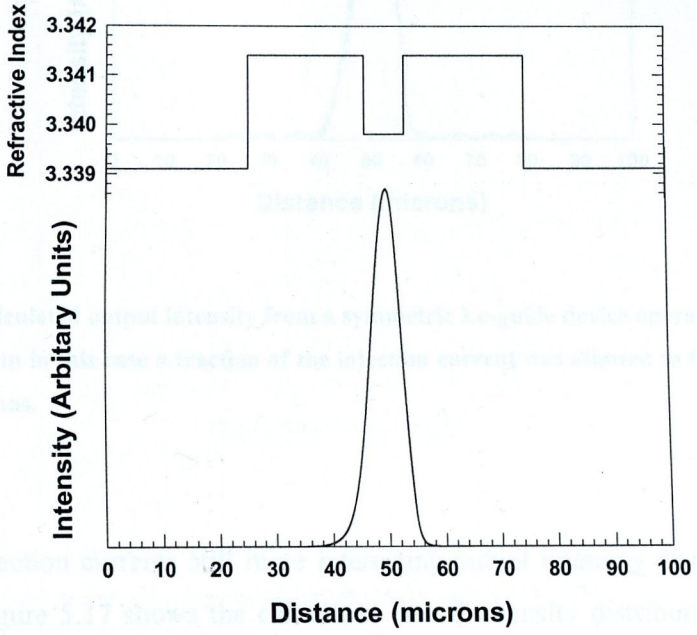

Figure 5-16 Calculated output intensity from a symmetric Lo-guide device operating at 1.1 times threshold. In this case a fraction of the injection current was allowed to flow through the high index regions.

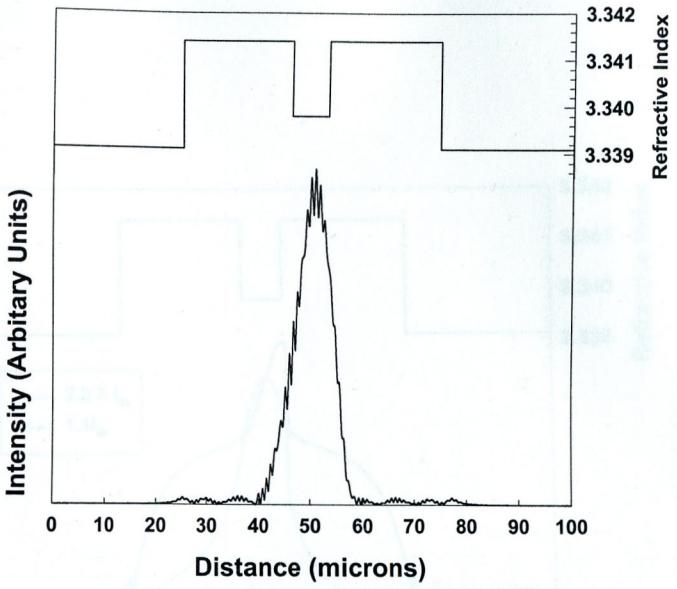

Figure 5-17 Calculated output intensity from a symmetric Lo-guide device operating at 2.2 times threshold. Again in this case a fraction of the injection current was allowed to flow through the high index regions.

At higher injection currents still more interesting output intensity distributions were obtained. Figure 5.17 shows the calculated lateral intensity distribution obtained at 2.2× threshold. This intensity profile was stable over the normalized current interval 1.9× to 2.3× threshold. The rapidly varying noise which is superimposed on trace is due numerical instability within the model rather than any physical effect. The evolution of the calculated intensity profile with injection current under this pumping scheme, can be understood by reference to Figure 5.18. This figure shows the calculated lateral gain profiles obtained at 1.1× and 2.2× threshold. Even under the current pumping configuration only a small section is pumped significantly above transparency at 1.1× I_{th}. Whereas at 2.2× I_{th} almost the entire Lo-Guide waveguide is pumped well above transparency, thus allowing the highest order mode of the structure to be successfully excited.

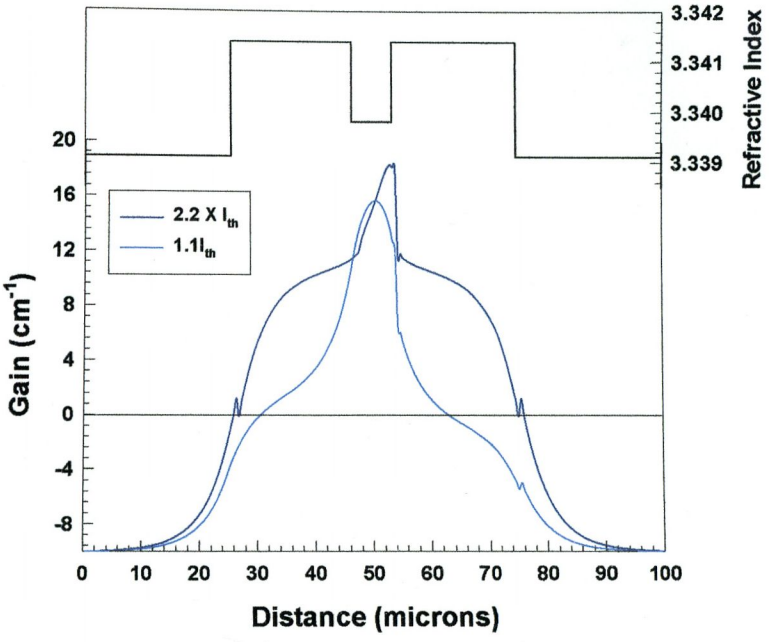

Figure 5-18Calculated lateral gain profiles for the symmetrical Lo-guide structure at 1.1(blue) and 2.2(purple) times threshold, generated by partially restricting the flow of current to the low index region

5.11 Summary.

In this chapter we have presented details of a laser model that was developed in the course of this work. The model, which is essentially a FD-BPM, allows the optical fields inside, gain guided and ridge waveguide lasers to be calculated. It allows for lateral and longitudinal variations of the carrier density as well as for coupling between these fields, which gives rise to instabilities such as filamentation. The model was used to calculate the lateral intensity profile of symmetric Lo-guide structure under different pumping schemes. Results obtained from the model demonstrated that mode dynamics of these structures is highly dependent on the pumping scheme used. However it was shown that it is possible to selectivity excite

the highest order mode of these structures. In the pumping scheme used to achieve this, set the current density flowing through the high index region at one quarter of the value flowing through the low index region.

5.12 References.

1 J. R. Marciante and G. P. Agrawal. Nonlinear Mechanisms of filamentation in broad-area semiconductors lasers. *IEEE J. Quantum Electron.,* 32(4):590-596, April 1996.

2 C.H. Henry. Theory of the linewidth of Semiconductor Lasers. *IEEE J. Quantum Electron.,* QE-18(2): 459-465, February 1982

3 M. Osinski, and J. Buus. Linewidth Broadened Factor in Semiconductor Lasers: An Overview. *IEEE J. Quantum Electron.,* QE-23(1): 9-465, February 29

4 R. Scarozzino, A. Gopinath, R. Pregla, and S. Helfert. Numerical techniques for modeling guided-wave photonic devices. IEEE Journal of Selected Topics in Quantum Electronics, 6(1):150-162, January/February 2000.

5 G. R. Hadley. Wide-angle beam propagation using Pade approximant operators. *Opt. Lett.*, 17(20): 1426-1428, October 1992.

6 G. R. Hadley. Multistep method for wide-angle beam propagation. *Opt. Lett.*, 17(24):1743-1745, December 1992.

7 M.D. Feit. And and J.A. Fleck. Light propagation in graded index optical fibers. *Appl. Opt.*, vol. 17, pp 3990-3998, 1978

8 R. Scarmozzino and R. M. Osgood, Jr. Comparison of finite-difference and Fourier-tranform solutions of the parabolic wave equation with emphasis on integrated-optics applications. Opt. Soc. Am. A, 8(5):724-731, May 1991.

9 Erwin Kreyseig. *Advanced engineering mathematics, Seventh edition.*, Wiley 1993. Section 20.6.

10 G.R. Hadley. Transparent boundary condition for beam propagation. Opt. Lett., 16(9):624-626, May 1991.

11 G.R. Hadley. Transparent boundary condition for the beam propagation method. *IEEE J. Quantum Electron.*, 28(1):363-370, January 1992.

12 W. H. Press, S.A. Teukolsky, W.T. Vettering and B.P. Flannery. *Numerical recipes in C*. pages 50-51, Cambridge Press.

13 H. Adachihara, O. Hess, E. Abraham, P. Ru, and J.V. Moloney. Spatiotemporal chaos in broad area semiconductor lasers. *J. Opt. Soc. Am. B.*, vol. 10, No. 4, pp 658-665, April 1993.

Chapter 6

Experimental Investigation of a Lo-Guide type Ridge Waveguide Structure.

6.1 Introduction.

Based on simulations preformed in Chapter 5, broad area ridge waveguide structures of the type shown in Figure 5.10 were fabricated. In this chapter a detailed analysis of the epitaxial structure in these devices is presented. This includes a presentation of the calculated intensity profiles and the effective indices of the transverse mode in different regions of the structure and details of the lateral modes structure of the device. As this is a first attempt at realizing such a structure in the lateral direction, many of the devices performance and emission characteristics are not optimized. Light–current characteristics and wavelength spectra were obtained for these devices. Standard and polarization resolved images of the nearfield emission patterns are presented, these measurements demonstrate that structure is lasing in its highest order mode. Also as predicted by the numerical simulations preformed in the previous chapter, it is shown that nearfield emission patterns are dependant on drive current.

6.2 Device Design: An Overview.

In this section, structural details of a Lo-guide type device, which was fabricated to confirm the results of the numerical simulations preformed in Chapter 5. Figure 6.1 illustrates the relative dimensions of one such device. It is noted that the top metal

contact and insulating oxide are not shown in this diagram. In this first attempt at realising a lateral Lo-guide device it was decided to electrically pump the entire ridge waveguide structure, this was in order to provide some gain in the high index regions, as suggested by the results of the numerical stimulations. To this end the entire top surface of the Lo-guide ridge was put in direct contact with the top metal electrode. It was felt that in this arrangement only a fraction of the total current would flow through the high index regions due to fact that conductivity of the metal contact is several orders of magnitude greater than that of the semiconductor material.

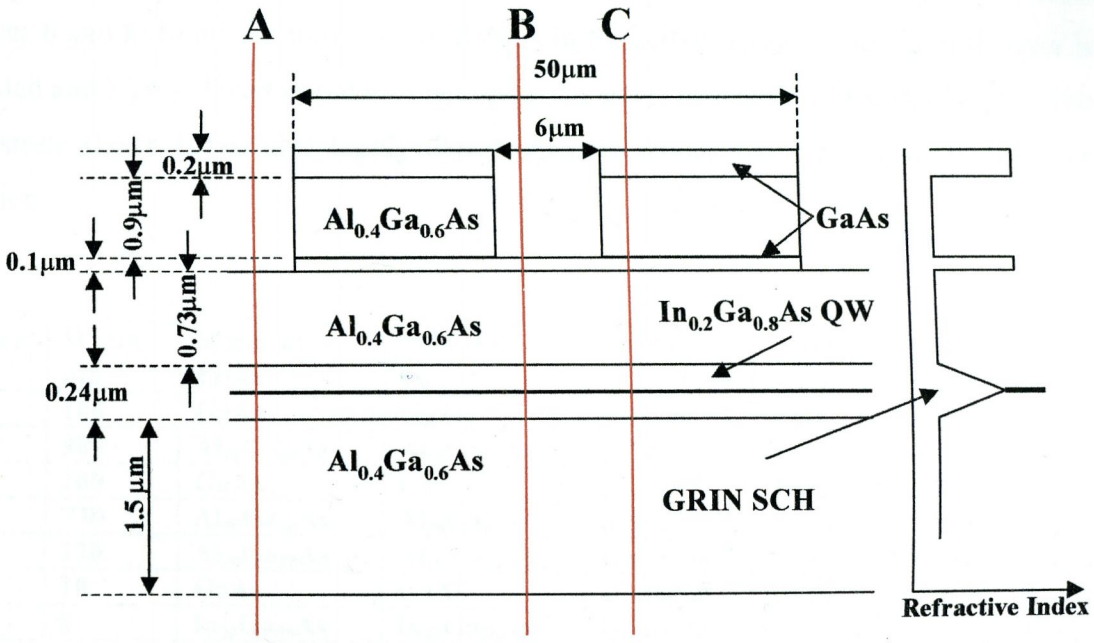

Figure 6-1 Illustration of the symmetric Lo-guide structure.

6.2.1 Epitaxial Design.

Table 6.1 shows, the thickness, aluminum mole fraction, refractive index and the doping concentrations of the individual epitaxial layers. The function of each layer shown will now be detailed. The first layer is generally referred to as the GaAs cap layer, the

function of this layer is to prevent oxidization of the under lying $Al_{0.40}Ga_{0.60}As$ layer. The second layer, which is 0.9μm thick defines the effective index step associated with high index regions of the structure. The third layer defines the effective index step associated with the structure central low index region. The interfaces between this and the layers above and below serve as etch stops for selective chemical etches. This layer was highly doped so as to provide an electrical contact with top metal contact. Layers 4 and 10 serve as cladding layers to the GRINSCH structure, these layers are moderately doped p-type and n-type respectively. This ensures the structure has a low series resistance while not causing too much free carrier absorption. The graded index layers 5 and 9 provide optical confinement in the transverse direction, these layers are undoped in order to minimize the internal losses of the device. Carrier confinement is provided by a single $In_{20}Ga_{80}As$ quantum well (layer 7). The use of GaAs for the quantum well barriers (layer 6 and 8) limits the formation of defects in the active region. The eleventh layer is graded and highly doped in order to minimize the series resistance of the device [1]. The substrate (layer 12) is also highly doped again to reduce the series resistance of the device.

Layer	Width nm	Material From	Material To	Doping	Index From	Index To	Comment
1	100	GaAs	GaAs	p-$1x10^{19}$	3.525	3.525	Cap Layer
2	900	$Al_{40}Ga_{60}As$	$Al_{40}Ga_{60}As$	p-$5x10^{17}$	3.304	3.304	
3	100	GaAs	GaAs	p-$1x10^{19}$	3.525	3.525	Etch Stop
4	730	$Al_{40}Ga_{60}As$	$Al_{40}Ga_{60}As$	p-$3x10^{17}$	3.304	3.304	Upper Clad
5	120	$Al_{40}Ga_{60}As$	$Al_{10}Ga_{90}As$	Undoped	3.304	3.471	Graded
6	10	GaAs	GaAs	Undoped	3.525	3.525	barrier
7	8	$In_{20}Ga_{80}As$	$In_{20}Ga_{80}As$	Undoped			QW
8	10	GaAs	GaAs	Undoped	3.525	3.525	barrier
9	120	$Al_{10}Ga_{95}As$	$Al_{40}Ga_{60}As$	Undoped	3.471	3.304	Graded
10	1500	$Al_{40}Ga_{60}As$	$Al_{40}Ga_{60}As$	n-$3x10^{17}$	3.304	3.304	Lower Clad
11	50	$Al_{40}Ga_{60}As$	GaAs	n-$2x10^{18}$	3.304	3.525	Graded
12	350000	GaAs	GaAs	n++	3.525	3.525	Substrate

Table 6-1 Layer structure of the lateral Lo-guide device

6.2.2 Waveguide Design.

The lateral modes supported by the Lo-guide ridge waveguide in Figure 6.1 will now be examined. Figure 6.2 show the effective profile produced by this ridge and the optical modes supported by it. This figure was shown in Section 5.10 but is repeated here for convenience. This figure shows that there is only one mode which has an intensity maximum in the low index region of the structure.

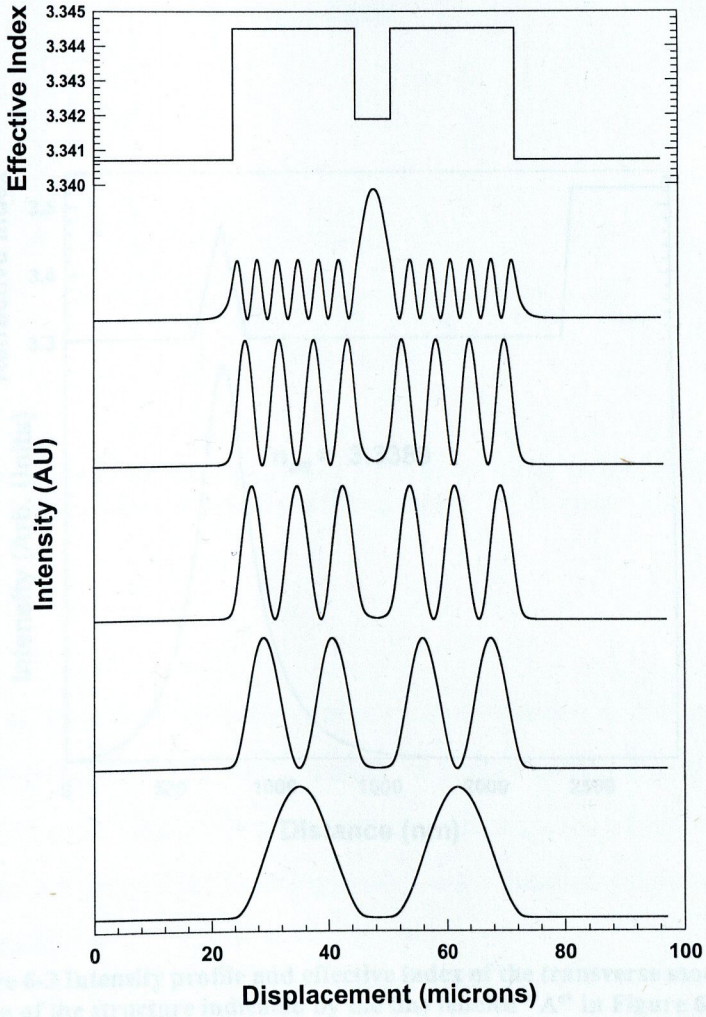

Figure 6-2 Effective index and mode structure of symmetric Lo-guide structure.

The details of how the effective index profile associated with Lo-guide ridge waveguide was calculated are now presented. In order to do this the effective index of the transverse mode in each part of the structure must be obtained. As the ridge structure is symmetrical this task can be achieved by calculating the effective index of this mode in just three places. The intensity distributions and effective indices of transverse mode in the regions indicated by the lines labeled A,B and C in Figure 6.1, are shown in Figures 6.3, 6.4 and 6.5 respectively.

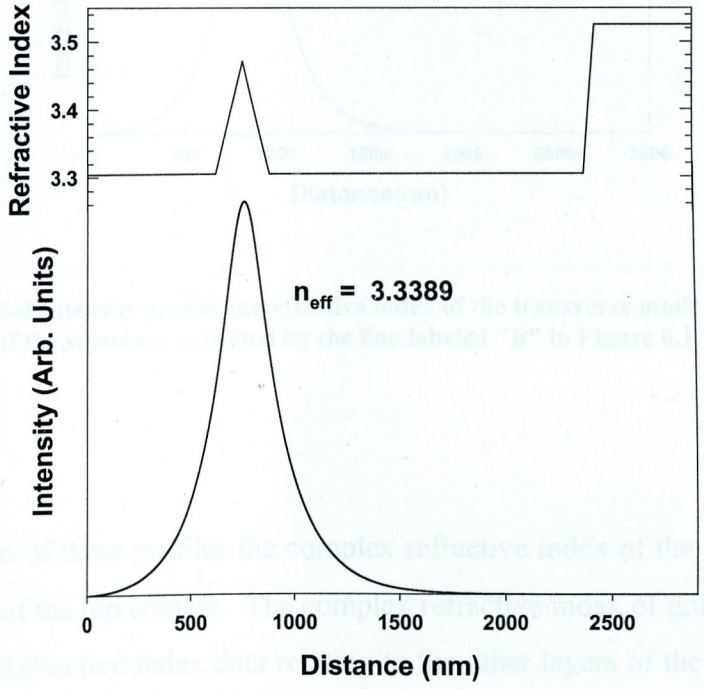

Figure 6-3 Intensity profile and effective index of the transverse mode in the region of the structure indicated by the line labeled "A" in Figure 6.1.

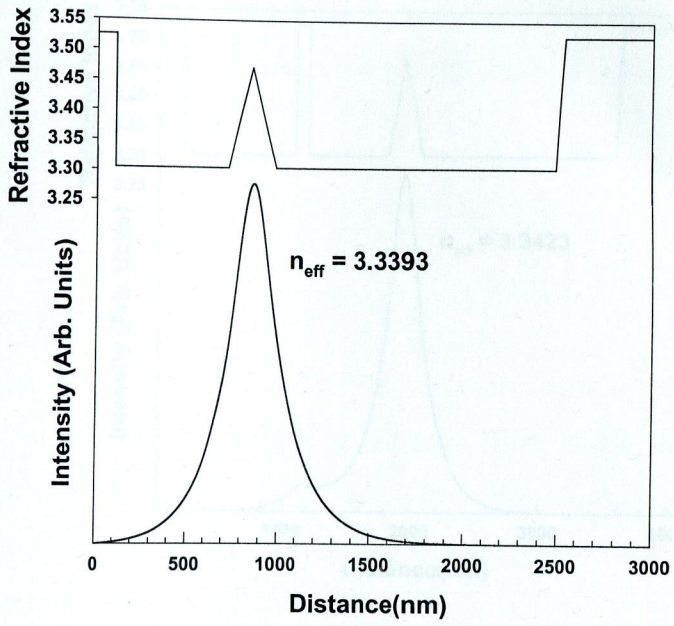

Figure 6-4 Intensity profile and effective index of the transverse mode in the region of the structure indicated by the line labeled "B" in Figure 6.1.

In the calculation of these profiles the complex refractive index of the gold was used for refractive index of the top contact. The complex refractive index of gold at $\lambda = 980$nm is 0.30 +7.5i [2]. Refractive index data relating to the other layers of the structure is given in Table 6.1. Effective index profile in Figure 6.2 was obtained using the values shown in Figures 6.3, 6.4 and 6.5.

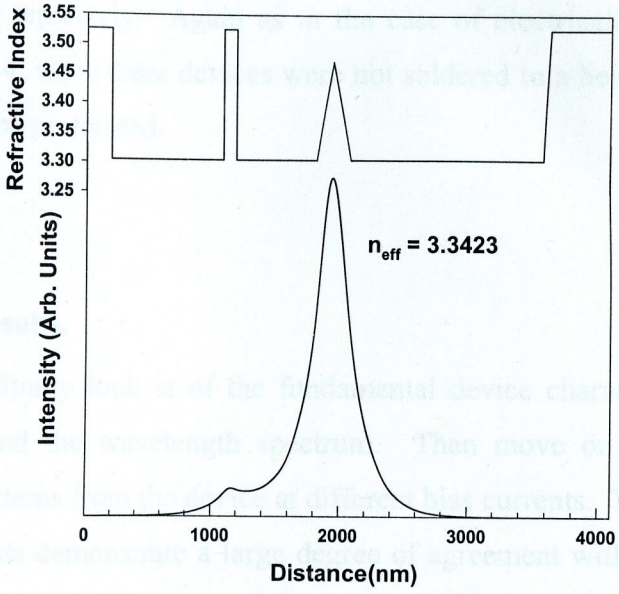

Figure 6-5Intensity profile and effective index of the transverse mode in the region of the structure indicated by the line labeled "C" in Figure 6.1.

6.2.3 Devices.

The epitaxial layer structure in Table 6.1 was grown by MOCVD on a 2 inch GaAs substrate. Part of this wafer had a number of Lo-guide ridge waveguide structures photo-lithographically upon it. This section of the wafer was cleaved into devices with cavity lengths of 625μm and 1000μm. In this chapter however we will focus only on the 625μm devices.

6.3 Experimental Setup.

The samples discussed above were investigated using the experimental setups described in Chapters 3 and 4. There was however one change in the nearfield measurement setup, the inclusion of a polariser allowed the spontaneous and stimulated emission from the device to be imaged separately. Again as in the case of electrically pumped devices discussed in Chapter 4, since these devices were not soldered to a heat sink, only pulsed measurements could be preformed.

6.4 Experimental Results.

As before we will initially look at of the fundamental device characteristics, such the light-current curve and the wavelength spectrum. Then move on to examining the nearfield emission patterns from the device at different bias currents. The results of these nearfield measurements demonstrate a large degree of agreement with the results of the simulations discussed in Chapter 5

6.4.1 Light-Current Characteristics.

In this section we present both standard and polarization resolved light current characteristics. Figure 6.6 shows the standard light current characteristic for a 625μm Lo-guide device. From this graph the threshold current of the device is estimated to be just under 40mA and its slope efficiency is 0.34W/A. Apart a number of small kinks the shape of the curve in this graph is as expected. Referring back to the analysis in Section 4.4, it was stated that in a laser diode the carrier density in the active region clamps at threshold [3]. This implies the amount of spontaneous emission from such device should also clamp at threshold, since the rate of spontaneous emission is proportional the carrier density squared. As explained in Section 2.9 stimulated emission from a laser diode will be predominately TE polarized. While spontaneous emission is to some degree unpolarised. On the bias of these arguments one would expect the measured power in a TM polarization resolved light-current curve to clamp at threshold. In these devices

however this is not observed to be case. Figure 6.7 shows the polarization resolved light current characteristic. The fact that the polarization resolved light current curve doesn't clamp at threshold, suggests that part of the structure is still below threshold.

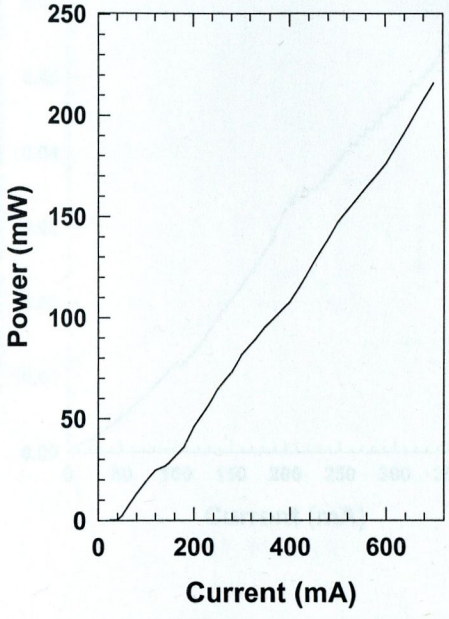

Figure 6-6 Standard light current characteristic for a Lo-guide ridge waveguide device.

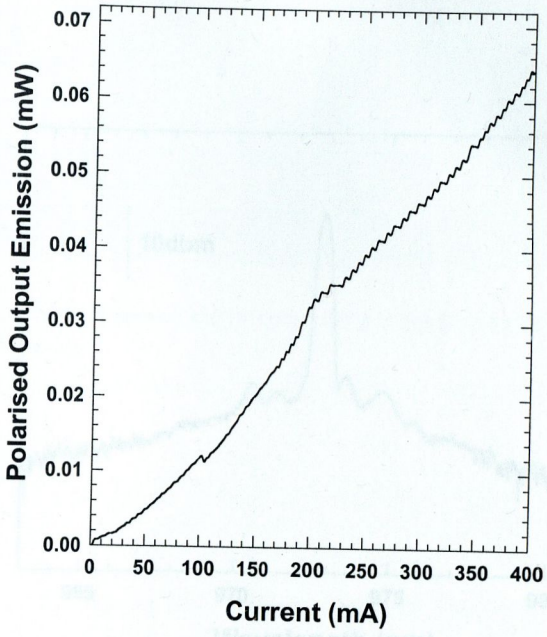

Figure 6-7 Polarisation resolved light current characteristic for a Lo-guide ridge waveguide device.

The results presented in this section will be examined more fully when the results of the nearfield measurement are detailed.

6.4.2 Spectral Characteristics.

Figure 6.8 shows the wavelength spectrum of the device at 80mA, twice the threshold current. It can be concluded from the narrow linewidth of this spectra (≈1nm), that the device is indeed lasing.

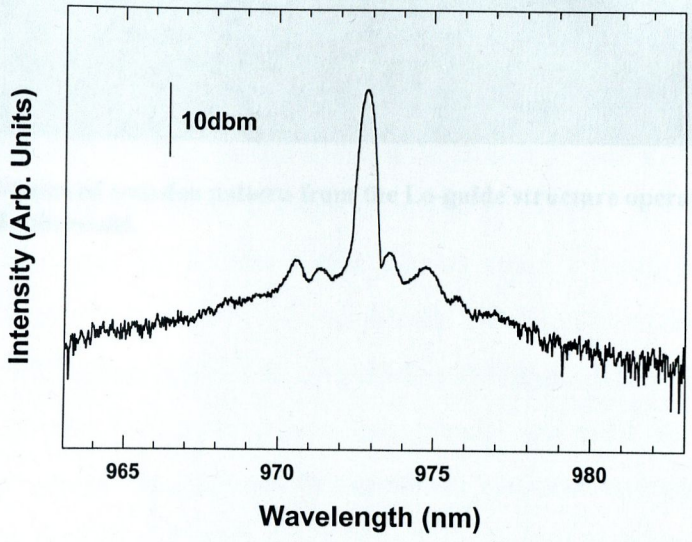

Figure 6-8 Wavelength spectrum at 80mA (or twice threshold).

6.4.3 Nearfield Measurements.

With sufficient evidence of lasing action in these structures now demonstrated, it is now time to examine their nearfield emission patterns. In this section both standard and polarization resolved nearfield images, obtained from a 625μm long Lo-guide device are examined. Initially we consider standard nearfield images obtained while the device is operating above threshold as these can be compared to the results the numerical simulations presented in Chapter 5. Figure 6.9 shows from the emission pattern from the Lo-guide device at a bias current of 60mA or roughly 1.5× threshold. This picture shows no evidence of the emission tailing off into the high effective index regions of the structure.

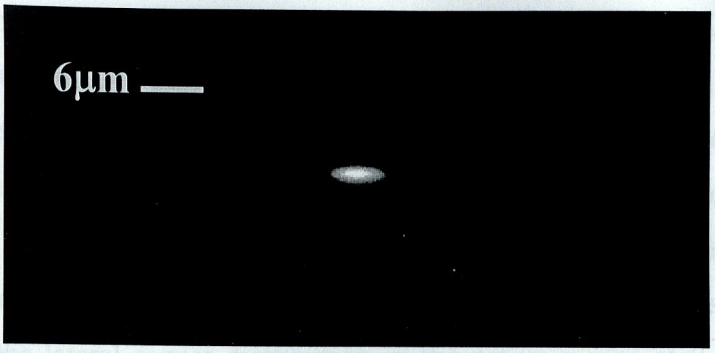

Figure 6-9 Measured emission pattern from the Lo-guide structure operating at 60mA or 1.5× threshold.

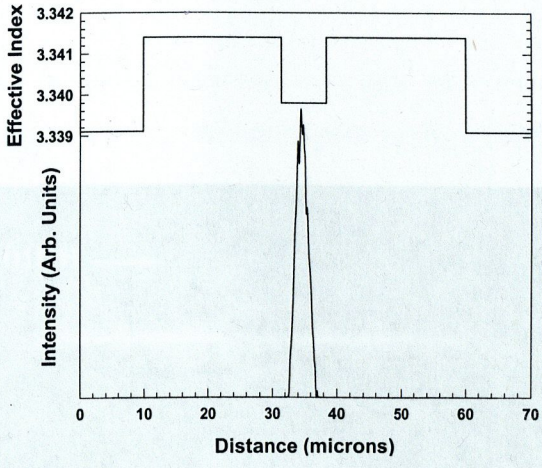

Figure 6-10 Lateral intensity profile obtained from Figure 6-9.

A look at the associated lateral intensity profile (Figure 6.9) quickly confirms this to be the case. At this point it is worth comparing intensity profile in Figure 6.9 with that shown in Figure 5.16. Both of these figures show the stimulated emission exclusively emanating from the central low index region. It is therefore suspected that the high index regions have not reached threshold yet, as predicted by the result of the numerical simulations (Section 5.10). This hypothesis is supported by the fact that measured power in the polarization resolved light current characteristic does not clamp at threshold. In an attempt to estimate the lateral carrier distribution in the active region at this operating current a polarization resolved image of the emission was measured. It was hoped that the resulting spontaneous emission pattern would help us attain a better understanding carrier spreading in this structure. Figure 6.11 shows the polarisation resolved emission pattern from the Lo-guide device, again with a operating at 60mA. The influence of the high index regions on the transverse mode can clearly be seen in this image. Unfortunately however because the spontaneous emission was predominately guided in the high effective index regions (Figure 6.12), Figure 6.11 doesn't give any insight into carrier spreading. Further because the FD BPM introduced in the Chapter 5 does not account for spontaneous emission, the polarization resolved emission cannot be predicted at present

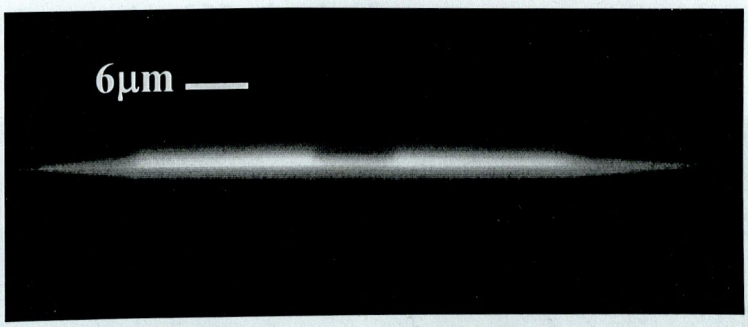

Figure 6-11 Polarisation resolved emission pattern from the Lo-guide structure operating at 60mA or 1.5× threshold.

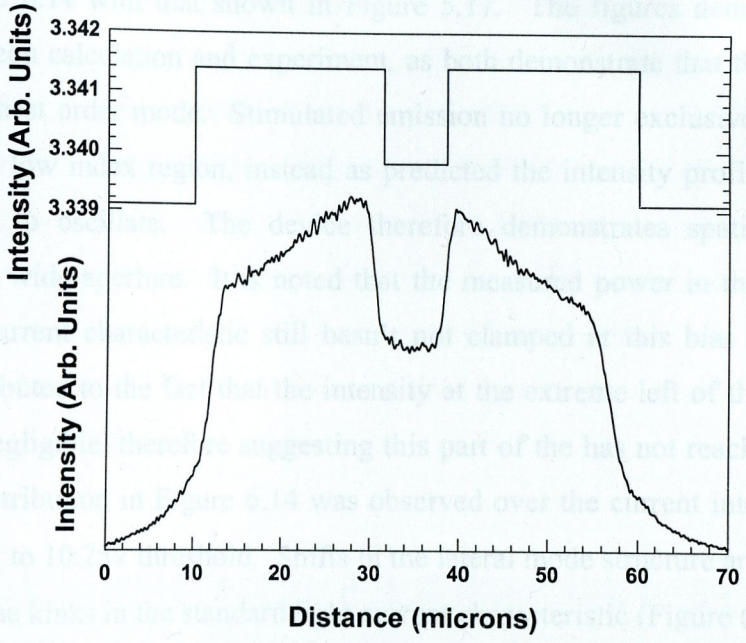

Figure 6-12 Lateral spontaneous emission intensity profile obtained from Figure 6-11.

At this point we move to considering the emission patterns obtained at higher bias currents. Figure 6.13 shows from the emission pattern from the Lo-guide device at a bias current of 250mA or roughly 6.25× threshold.

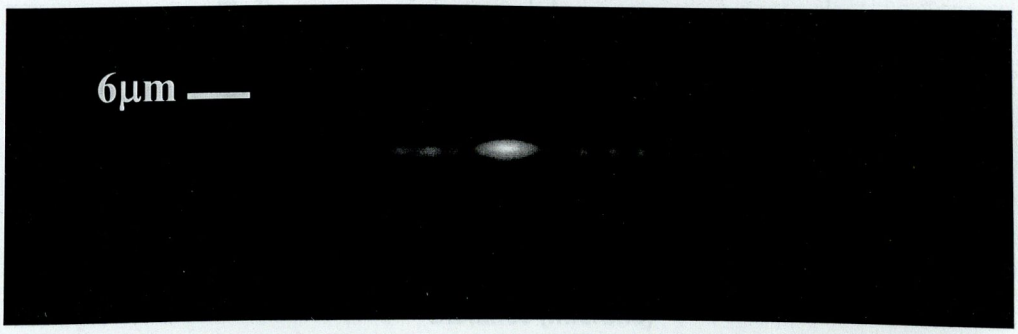

Figure 6-13 Measured emission pattern from the Lo-guide structure operating at 250mA or 6.25× threshold.

A careful examination of this image does indeed reveal structured emission in the high effective index regions of the structure. A look at the associated lateral intensity profile (Figure 6.14) confirms this to be the case. Again it is worth comparing the intensity profile in Figure 6.14 with that shown in Figure 5.17. The figures demonstrate good agreement between calculation and experiment, as both demonstrate that the structure is lasing in its highest order mode. Stimulated emission no longer exclusively emanating from the central low index region, instead as predicted the intensity profile in the high regions is seen to oscillate. The device therefore demonstrates spatially coherent emission from a wide aperture. It is noted that the measured power in the polarization resolved light current characteristic still hasn't not clamped at this bias current level. This can be attributed to the fact that the intensity at the extreme left of the structure in Figure 6.14 is negligible, therefore suggesting this part of the has not reached threshold. The intensity distribution in Figure 6.14 was observed over the current interval, 220mA to 410mA, or 5.5 to 10.25× threshold. Shifts in the lateral mode structure are most lightly responsible for the kinks in the standard light current characteristic (Figure 6.6).

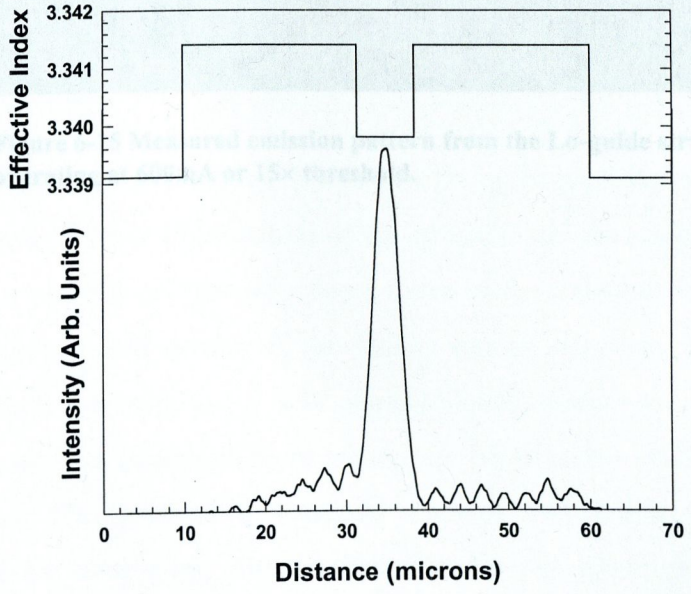

Figure 6-14 Lateral intensity profile obtained from Figure 6-13.

At higher current still the emission suffers from filamentary behavior. Filamentation [4] is caused by carrier induced changes in the effective index profile, which results in the anti-guiding of light. In broad area lasers this anti-guiding, the magnitude of which is controlled by the linewidth enhancement factor, causes the lateral mode to break up in to multiple filaments. This results in a spatial variation of the gain and refractive index in the lateral direction, this in turn leads to a situation in which the optical intensity maxima correspond to carrier density minima. This causes inefficient device operation, since an appreciable fraction of the population inversion being lost to spontaneous emission [5]. Figure 6.15 shows the emission pattern from the Lo-guide device at a bias current 600mA. At this bias current level the emission pattern has completely into optical filaments. While figure 6.16 shows the corresponding lateral intensity profile.

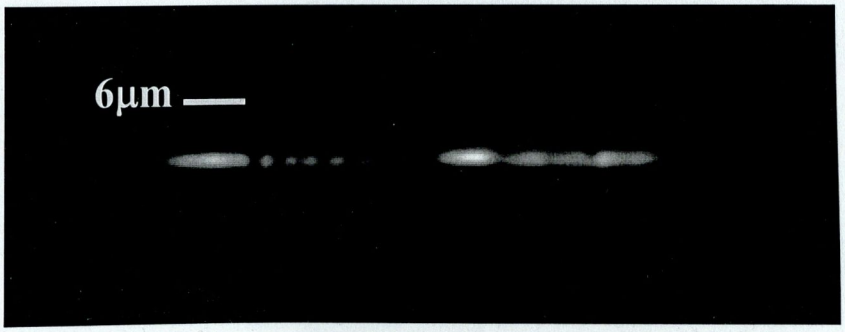

Figure 6-15 Measured emission pattern from the Lo-guide structure operating at 600mA or 15× threshold.

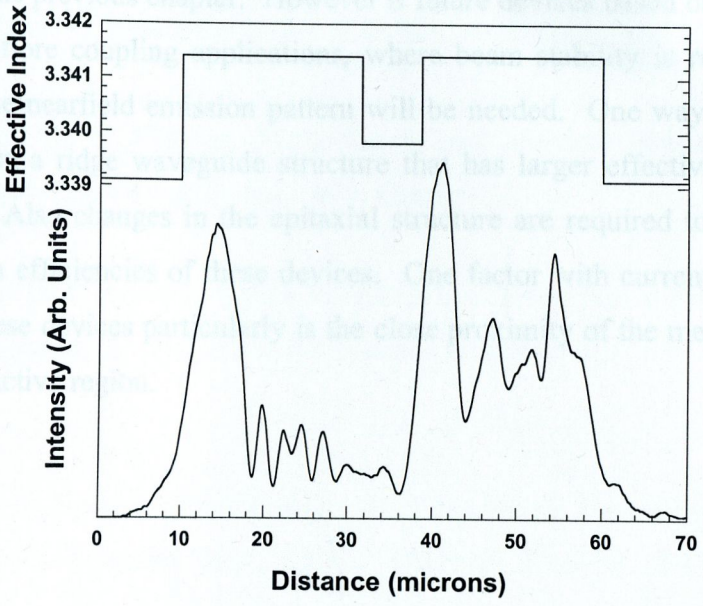

Figure 6-16 Measured lateral intensity profile at 600mA or 15× threshold, obtained from Figure 6-15.

6.5 Summary.

In this chapter we explored in detail the design of a Lo-guide type, ridge waveguide laser. This included a layer by layer examination of the epitaxial structure, a presentation of the calculated intensity profiles and the effective indices of the transverse mode in different regions of the structure and details of the lateral modes structure of the device. A measured wavelength spectrum and a light current characteristic were then presented in order to demonstrate that structures were lasing. A polarization resolved light current characteristics was also presented, strangely enough this graph showed that the spontaneous emission emanating from the device did not clamp at threshold. On reflection however, this result could have been expected based on the results of the

numerical stimulations preformed in Chapter 5. As in these stimulations the entire device didn't reach threshold all at once. Nearfield measurements confirmed this to be the case, showing that the emission pattern from this device to be highly dependent on the bias current applied. Overall the results presented here demonstrated good agreement with those generated in the previous chapter. However if future devices based on this concept are to be used for fibre coupling applications, where beam stability is required much tighter control of the nearfield emission pattern will be needed. One way of achieving this would be to use a ridge waveguide structure that has larger effective index steps associated with it. Also changes in the epitaxial structure are required to improve the differential quantum efficiencies of these devices. One factor with currently makes the internal losses in these devices particularly is the close proximity of the metal in the low index region to the active region.

6.6 References.

1 R.G. waters, D.S. Hill, and S.L. Yellen. Efficiency enhancement in quantum well lasers via tailoring doping profiles. *Appl. Phys. Lett.,* vol: 52, pp 2017-2018, 1988.

2 E.D. Palik. Handbook of Optical Constants of Solids. Academic Press 1998.

3 L. A. Coldren and S. W. Corzine. *Diode lasers and photonic integrated circuits.* Microwave and optical engineering. Wiley, 1995. Chapter 2.

4 J. R. Marciante and G. P. Agrawal. Spatio Temporal Characteristics of Filamentation in Broad Area Semiconductor Lasers. *IEEE J. Quantum Electron.,* 33(7): 1147-1179, July 1997

5 W. W. Chow and D. Depaite. Filamentation in conventional double heterosturctures and quantum well semiconductors lasers. *IEEE J. Quantum Electron.,* 24(7):1297-1301, July 1998.

Chapter 7

Conclusions.

7.1 Overview.

This thesis has been concerned with the numerical and experimental investigation of a novel waveguide concept for use in high power laser diode devices. Because of their efficiency, small size and reliability high power laser diodes are used for numerous tasks, such as the pumping of solid state lasers, second harmonic generation and the pumping of rare earth fibre amplifiers. In Chapter 2 the advantages and disadvantages of some existing high power laser diode devices were detailed.

A unique feature of the waveguiding concept investigated in this thesis is that the last mode before cut-off is predominantly confined to the low index region of the waveguide structure. As this is quite a counter intuitive result, structures based on this design concept, were for shorthand purposes dubbed Lo-guides. A number of variations on this concept were discussed in Section 2.10. As each of these structures is a multimode waveguide, a device incorporating any of these structures must be designed in such a way as to discriminate against the other modes of the structure. The initial goal of this work, was to achieve single mode spatially coherent emission from a broad area aperture structure. It was envisioned that this would be achieved using structures similar to those which were investigated numerically and experimentally in Chapters 5 and 6. As described in Section 2.11, spatially coherent from broad area structures can be efficiently coupled into optical fibres. Chapters 3 to 6 detailed the development of a prototype laser diode incorporating such a structure.

Chapter 3 detailed the numerical and experimental analysis, which was carried out on conventional waveguide designs and novel waveguides designs of the type discussed in Section 2.10. The waveguiding structures discussed in this Chapter were all fabricated in the transverse direction, as this allowed a more accurate implementation of the waveguide designs. A procedure for designing heterostructure and ridge wavegiude structures was presented this included a description of a numerical method for calculating the modal solutions of arbitrarily shaped waveguides. Epitaxial structures of the various devices grown were discussed, as were the experimental setups used to perform transmission and optical pumping measurements. The main result disclosed in Chapter 3 was the observation of an asymmetric Lo-guide structure lasing in one of its highest order modes. The structure in question had five $In_{0.20}Ga_{0.80}As$ QWs placed to coincide with the intensity maximum of the structures highest order mode. Due to energy band gap considerations and the availability of an appropriate wavelength laser, optical pumping of the symmetric Lo-guide structure wasn't possible. In Chapter 4 we moved on to considering a similar waveguide design, which had been incorporated in a laser diode.

Having demonstrated that it was possible to excite the last mode before cut-off in our novel waveguide by optically pumping, it was decided to incorporate a similar waveguide design in a laser diode device. This represented the first attempt to implement the Lo-guide concept in an electrically pumped device. Again due to energy band considerations and wavguiding issues, it was easier to implement the Lo-guide concept in the growth direction based on the asymmetric waveguide structure. This device is basically a separate confinement heterostructure in which the carriers are confined by the quantum wells and the light by the waveguide structure. The main difference between this and the optically pumped structure, is that the layers in this structure are doped so as to allow the device to be electrically pumped. The refractive index profile of this device was also slightly different from that of the optically pumped sample. This design modification was to ensure that there was only one mode that had an anti-node in the low refractive index region of the structure, as opposed to the optically pumped sample that had two. The resulting devices were characterized under pusedo-CW conditions. Extensive measurements were made of the emitted power versus electrical current for two stripe widths and three different cavity lengths. From these results values for the

internal quantum efficiency, η_i, and the internal losses, α_i, for these structures were determined. Wavelength spectra were measured as a function of bias current to ensure that they were consistent with laser emission. The main function of the measurements mentioned thus far was to demonstrate that these devices didn't exhibit any unepected behavior. Once this was done the nearfield and farfield emission patterns were measured and compared with what was predicted by theory. These results confirmed that the structure was lasing exclusively in its highest order mode.

In Chapter 5 we considered how to implement the Lo-guide design concept in the lateral direction as was originally envisaged. The main focus of this chapter is on the design of such structures by performing numerical stimulations. Extensive details of a computer program which was written to perform this task are presented, this computer model allowed for lateral and longitudinal variations of the carrier density as well as for coupling between these fields, which gives rise to instabilities such as filamentation. The approach taken was to try a number to different pumping schemes, in an attempt to selectivity excite the highest order mode of such a structure. It was found that by setting the current density injected through the index regions of the structure at a quarter of the injection level in the low index region, that it was possible to excite the structure highest order mode over the current interval 1.9× to 2.3× threshold. The results obtained from the model demonstrated that mode dynamics of these structures is highly dependent on the both pumping scheme used and the injected current level.

Based on simulations preformed in Chapter 5, broad area ridge waveguide structures of the type shown in Figure 5.10 were fabricated. Chapter 6 explores in detail the epitaxial design of these Lo-guide type, ridge waveguide lasers. This included a layer by layer examination of the epitaxial structure, and a presentation of the calculated intensity profiles and the effective indices of the transverse mode in different regions of the structure. Measured wavelength spectra and a light current characteristic revealed that the effect of laser action was being achieved. Polarisation resolved light current characteristics was also made, which strangely enough showed that the spontaneous emission emanating from the device did not clamp at threshold. On reflection however, this result could have been expected based on the results of the numerical stimulations preformed in Chapter 5. In these stimulations the entire device didn't reach threshold all

at once. Nearfield measurements confirmed this to be the case, showing that the emission pattern from this device to be highly dependent on the bias current applied. Overall the results presented here demonstrated good agreement with those generated in the previous chapter. However work remains to be done in order to prefect this design, also some of the other structures introduced in Section 2.9 have yet to be investigated.

7.2 Future Work.

If future devices based on the Lo-guide concept are to be used for fibre coupling applications, where beam stability is required much tighter control of the nearfield emission pattern will be needed. One way of achieving this would be to use a ridge waveguide structure that has larger effective index steps associated with it. Also future structures optimizing the farfield pattern must be a priority. Changes in the epitaxial structure are required to improve the differential quantum efficiencies of these devices. One way of doing this would be to use a LOC structure instead of the current heterostructure design. Another factor which currently makes the internal losses in these devices particularly is the close proximity of the metal in the low index region to the active region. It might be possible improve this situation by using a Zn diffused superlattice to provide the necessary optical and carrier confinement. In conclusion working prototype structures based on the Lo-guide concept being demonstrated, however much work remains to be done in order to perfect the operation of these devices.

Appendix 1: TE and TM modes.

The nature of TE and TM modes can best be seen by reverting to the Cartesian components of Maxwell's equations, in particular Equations for 2.57 and 2.58. Initially we consider Equation 2.57

$$\begin{vmatrix} \hat{\mathbf{x}} & \hat{\mathbf{y}} & \hat{\mathbf{z}} \\ \partial/\partial x & \partial/\partial y & \partial/\partial z \\ E_x & E_y & E_z \end{vmatrix} = -\frac{\partial \mathbf{B}}{\partial t} \qquad \text{A1.1}$$

$$\left(\frac{\partial E_z}{\partial y} - \frac{\partial E_y}{\partial z}\right)\hat{\mathbf{x}} + \left(\frac{\partial E_x}{\partial z} - \frac{\partial E_z}{\partial x}\right)\hat{\mathbf{y}} + \left(\frac{\partial E_y}{\partial x} - \frac{\partial E_x}{\partial y}\right)\hat{\mathbf{z}} = -\frac{\partial B_x}{\partial t}\hat{\mathbf{x}} - \frac{\partial B_y}{\partial t}\hat{\mathbf{y}} - \frac{\partial B_z}{\partial t}\hat{\mathbf{z}} \qquad \text{A1.2}$$

Equating the x,y,z-components on each side of Equation A1.2 yields

$$\frac{\partial E_z}{\partial y} - \frac{\partial E_y}{\partial z} = \mu_r \mu_0 \frac{\partial H_x}{\partial t} = i\mu_r \mu_0 \omega H_x \qquad \text{A1.3}$$

$$\frac{\partial E_x}{\partial z} - \frac{\partial E_z}{\partial x} = \mu_r \mu_0 \frac{\partial H_y}{\partial t} = i\mu_r \mu_0 \omega H_y \qquad \text{A1.4}$$

$$\frac{\partial E_y}{\partial x} - \frac{\partial E_x}{\partial y} = -\mu_r \mu_0 \frac{\partial H_z}{\partial t} = i\mu_r \mu_0 \omega H_z \qquad \text{A1.5}$$

Now by expanding Equation 2.58 in a similiar way

$$\begin{vmatrix} \hat{\mathbf{x}} & \hat{\mathbf{y}} & \hat{\mathbf{z}} \\ \partial/\partial x & \partial/\partial y & \partial/\partial z \\ H_x & H_y & H_z \end{vmatrix} = \frac{\partial \mathbf{D}}{\partial t} \qquad \text{A1.6}$$

$$\left(\frac{\partial H_z}{\partial y} - \frac{\partial H_y}{\partial z}\right)\hat{\mathbf{x}} + \left(\frac{\partial H_x}{\partial z} - \frac{\partial H_z}{\partial x}\right)\hat{\mathbf{y}} + \left(\frac{\partial H_y}{\partial x} - \frac{\partial H_x}{\partial y}\right)\hat{\mathbf{z}} = \frac{\partial D_x}{\partial t}\hat{\mathbf{x}} + \frac{\partial D_y}{\partial t}\hat{\mathbf{y}} + \frac{\partial D_z}{\partial t}\hat{\mathbf{z}} \qquad \text{A1.7}$$

Equating the x,y,z-components an each side of Equation A1.7, yields the following set of equations.

$$\frac{\partial H_z}{\partial y} - \frac{\partial H_y}{\partial z} = -\varepsilon_r \varepsilon_0 \frac{\partial E_x}{\partial t} = -i\varepsilon_r \varepsilon_0 \omega E_x \qquad \text{A1.8}$$

$$\frac{\partial H_x}{\partial z} - \frac{\partial H_z}{\partial x} = -\varepsilon_r \varepsilon_0 \frac{\partial E_y}{\partial t} = -i\varepsilon_r \varepsilon_0 \omega E_y \qquad \text{A.19}$$

$$\frac{\partial H_y}{\partial x} - \frac{\partial H_x}{\partial y} = -\varepsilon_r \varepsilon_0 \frac{\partial E_z}{\partial t} = -i\varepsilon_r \varepsilon_0 \omega E_z \qquad \text{A1.10}$$

Rearranging Equations A1.3 to A1.5 and A1.8 to A1.10 we obtain

$$H_x = \frac{1}{i\mu_r \mu_0 \omega}\left(\frac{\partial E_z}{\partial y} - \frac{\partial E_y}{\partial z}\right) \qquad \text{A1.11}$$

$$H_y = \frac{1}{i\mu_r \mu_0 \omega}\left(\frac{\partial E_x}{\partial z} - \frac{\partial E_z}{\partial x}\right) \qquad \text{A1.12}$$

$$H_z = \frac{1}{i\mu_r \mu_0 \omega}\left(\frac{\partial E_y}{\partial x} - \frac{\partial E_x}{\partial y}\right) \qquad \text{A1.13}$$

$$E_x = \frac{-1}{i\varepsilon_r \varepsilon_0 \omega}\left(\frac{\partial H_z}{\partial y} - \frac{\partial H_y}{\partial z}\right) \qquad \text{A1.14}$$

$$E_y = \frac{-1}{i\varepsilon_r \varepsilon_0 \omega}\left(\frac{\partial H_x}{\partial z} - \frac{\partial H_z}{\partial x}\right) \qquad \text{A1.15}$$

$$E_z = \frac{-1}{i\varepsilon_r \varepsilon_0 \omega}\left(\frac{\partial H_y}{\partial x} - \frac{\partial H_x}{\partial y}\right) \qquad \text{A1.16}$$

Since the slab waveguide in Figure 2.15 is uniform in the x direction, $\partial/\partial x$ can in this case be set to zero. Equations A1.11 to A1.16 can therefore be re-written as follows

$$H_x = \frac{1}{i\mu_r \mu_0 \omega}\left(\frac{\partial E_z}{\partial y} - \frac{\partial E_y}{\partial z}\right) = \frac{1}{i\mu_r \mu_0 \omega}\frac{\partial E_z}{\partial y} - \frac{\beta}{\mu_r \mu_0 \omega} E_y \qquad \text{A1.17}$$

$$H_y = \frac{1}{i\mu_r\mu_0\omega}\frac{\partial E_x}{\partial z} = \frac{\beta}{\mu_r\mu_0\omega}E_x \qquad \text{A1.18}$$

$$H_z = \frac{-1}{i\mu_r\mu_0\omega}\frac{\partial E_y}{\partial x} \qquad \text{A1.19}$$

$$E_x = \frac{-1}{i\varepsilon_r\varepsilon_0\omega}\left(\frac{\partial H_z}{\partial y} - \frac{\partial H_y}{\partial z}\right) = \frac{-1}{i\varepsilon_r\varepsilon_0\omega}\frac{\partial H_z}{\partial y} + \frac{\beta}{\varepsilon_r\varepsilon_0\omega}H_y \qquad \text{A1.20}$$

$$E_y = \frac{-1}{i\varepsilon_r\varepsilon_0\omega}\frac{\partial H_x}{\partial z} = -\frac{\beta}{\varepsilon_r\varepsilon_0\omega}H_x \qquad \text{A1.21}$$

$$E_z = \frac{1}{i\varepsilon_r\varepsilon_0\omega}\frac{\partial H_x}{\partial y} \qquad \text{A1.22}$$

These six equations form two independent sets. Equations A1.18, A1.19 and A1.20, contain only the field components E_x, H_y and H_z, while the Equations A1.18, A1.21 and A1.22 contain only the field components H_x, E_y and E_z. In the first set E_z is always equal to zero. The solutions of this first set of equations are known as TE (transverse electric) modes. In the second set H_z is always equal to zero, the solutions of this set of equations are known as TM (transverse magnetic) modes. Inserting H_y and H_z from Equations A1.18 and A1.19 into Equation A1.20, yields the following wave equation for E_x.

$$\frac{d^2E_x}{dx^2} + (n^2(y)k^2 - \beta^2)E_x = 0 \qquad \text{A1.23}$$

Similarly inserting E_y and E_z from Equations A1.21 and A1.22 into Equation A1.17, yields the wave equation for H_y.

$$\frac{d^2H_x}{dx^2} + (n^2(y)k^2 - \beta^2)H_x = 0 \qquad \text{A1.24}$$

The solutions to Equations A1.23 and A1.24 are of the form

$$\psi = \psi_0(x)\exp\{-i(\omega t - \beta z)\} \qquad \text{A1.25}$$

The complete solution set for TE modes can therefore be written as follows

$$E_x = E_0(y)\exp\{-i(\omega t - \beta z)\} \quad \text{A1.26}$$

$$H_y = \frac{\beta}{\mu_r \mu_0 \omega} E_x \quad \text{A1.27}$$

$$H_z = \frac{-1}{i\mu_r \mu_0 \omega}\frac{\partial E_y}{\partial x} \quad \text{A1.28}$$

While the complete solution set for TM modes can therefore written

$$H_x = H_0(y)\exp\{-i(\omega t - \beta z)\} \quad \text{A1.29}$$

$$E_y = -\frac{\beta}{\varepsilon_r \varepsilon_0 \omega} H_x \quad \text{A1.30}$$

$$E_z = \frac{1}{i\varepsilon_r \varepsilon_0 \omega}\frac{\partial H_x}{\partial y} \quad \text{A1.31}$$

Appendix 2: The effective index method.

Obtaining the lateral and transverse field profiles associated with a particular spatial mode is two-dimensional problem, which typically involves extensive numerical modeling. For many applications, however it is sufficient to solve two simpler one-dimensional problems.

For the reasons mentioned early in Section 2.9, semiconductor lasers generally lase in TE modes. We therefore restrict our selves here, to considering the spatial distributions associated of TE modes. In TE modes the electric field $E_x(x,y,z,t)$ is polarized in the lateral direction. This field which is a superposition of lateral and transverse modes, can be expressed in the form,

$$E_x(x,y,z,t) = E(x)F(x,y)\exp i(\beta z - \omega t) \qquad \text{A2.1}$$

which satisfies the scalar wave equation.

$$\frac{\partial^2 E_x}{\partial x^2} + \frac{\partial^2 E_x}{\partial y^2} + \frac{\partial^2 E_x}{\partial z^2} + k_0{}^2 n^2(x,y,z)E_x = 0 \qquad \text{A2.2}$$

where $\beta = k_0\eta_{eff}$ is the complex modal propagation constant and η_{eff} is the complex modal effective index. $E(x)$ and $F(x,y)$ are the lateral and transverse mode profiles. It is noted that $F(x,y)$ is a slowly varying function of the lateral coordinate x. At a particular value of x, the transverse mode $F(x,y)$ and its effective index $n_{eff}(x)$ are eigensolutions of the transverse waveguide. The lateral mode $E(x)$ and its propagation constant β are eigensolutions of the complex index profile subsequently constructed from $n_{eff}(x)$ [X]. This technique is known as the effective index method and is valid when the lateral refractive index and electric field variations are much slower than the transverse ones.

Substituting Equation A2.1 into A2.2 yields the following partial differential equation.

$$E\frac{d^2F}{dy^2}+\frac{d^2(EF)}{dx^2}+k_0^2n^2(x,y)EF-\beta^2EF=0 \qquad \text{A.2.3}$$

If $F(x,y)$ is a slowly varying function with respect to x, then the derivatives of $F(x,y)$ with respect to x can be neglected. Thus $F(x,y)$ is proposed to be an eigensolution of

$$\frac{d^2F(x,y)}{dy^2}+k_0^2(n(x,y)-n_{eff}^2(x))F(x,y)=0 \qquad \text{A2.4}$$

and $E(x)$ is proposed to be an eigensolution of

$$\frac{d^2E(x)}{dx^2}+k_0^2(n_{eff}^2(x)-\eta^2)E(x)=0 \qquad \text{A2.5}$$

The term $k_0^2n_{eff}^2(x)$ therefore acts as a mathemathical separation constant which allows Equation A2.3 to be decoupled into Equations A2.4 and A2.5

Appendix 3: Source Code for the Beam Propagation Model.

```
#include <stdio.h>
#include <iostream.h>
#include <fstream.h>
#include <math.h>                    //changed stripe width, gain exp 1 to 0.5 and loses 1000 to 10
#include <stdlib.h>
#include <complex.h>
#include <stddef.h>

#define NR_END 1
#define FREE_ARG char*

/*Dimensions and refractive indcies of the structure*/
#define width_m 100e-6                                   /*Width of computional domain
metres*/
#define length_m 0.00035          /*Length of cavity in metres*/
#define Nclad  3.339178           /*Index of cladding layer*/
#define Nave   3.339178   //3.49                                   /*Background
Index same as cladding layer*/
#define Nside  3.341416
//#define Ndep   3.339278
#define Ncore     3.339873        /*Index of core region*/

/*Physical Constants*/
#define pi 3.141592654
#define hplanck 6.626075e-34          /*Plancks Constant*/
#define Clight_m 3.0e8                                   /*speed of light in vacume
m/s */
#define epsilon 8.8e-12                                  /*permitivity of free space C/(N^-1*m^-2)
*/
#define Qe  1.602e-19                                    /*magnitude of electronic charge
Coulombs */


/*Number of grid points*/
#define NumZ 3000
#define NumX 250

/*Device parameters */
#define reflectr 0.35                                    //reflectivity of right facet
#define reflectl 0.35                                    //reflectivity of left facet
#define lambda_m 9.8e-7                                  // Wavelength of light in metres
#define Tau 5.0e-9                                             //Non radative
recombination lifetime seconds
#define Again_m 2.0e-20                                  // Differential gain m^2
#define Nzero_m 1.0e24                                   // Transperancy carrier density per
m^3
#define alpha_m  1000.00                                 // losses per metre
```

```
#define Rline 1.5                                   //Linewidth enhancement
factor
//#define Jinit_m 11.00e6                           // Initial current density  A/m^2
//#define Df_m 10.0e-4                              //diffusion co-efficient m^2/s   or
10cm^2/s
#define Df_m 40.0e-4                                //diffusion co-efficient
m^2/s   or 33cm^2/s
#define GaussFWHM_m 6e-6                            // FWHM of initial field
#define Ezero 0.15                                  //Magnitude of the electric
field
//#define Gamma 0.0366                              //Confinement factor
#define d_m 20e-9                                   //Width of the
active region in metres
//#define B 1.4e10-4                                //Spontaneous emission co-efficient in
m^3/s


/* This equation will solve beam propagation in a waveguide as opposed to
        a laser, so some of the parameters above are not necessary and will not
        be used */

void nrerror(char error_text[]);
complex *cvector(long nl, long nh);
double *dvector(long nl, long nh);
void ctridag(complex a[NumX], complex b[NumX], complex c[NumX], complex d[NumX], complex
E_new[NumX]);
void dtridag(double aa[NumX], double bb[NumX], double cc[NumX], double dd[NumX], double
N[NumX]);
double **dmatrix(long nrl, long nrh, long ncl, long nch);
complex **cmatrix(long nrl, long nrh, long ncl, long nch);
void cfree_vector(complex *v, long nl, long nh);
void dfree_vector(double *v, long nl, long nh);
void cfree_matrix(complex **m, long nrl, long nrh, long ncl, long nch);
void dfree_matrix(double **m, long nrl, long nrh, long ncl, long nch);
void file(char out_text[], double Currentden, char filename[128]);



template < class T >
void savetofile(int size, char filename[128], T array[])
{
        long int j;
  ofstream fout(filename);
  if(imag(array[0]) == 0.0){
        for (j=0;j<=size;j++){
        if(j==0) cout << filename << endl;
                fout << array[j] << endl; //<< real(Corr[j]) << imag(Corr[j]) << endl;
        }
  }
  else{
        for (j=0;j<=size;j++){
                fout << abs(array[j]) << endl; //<< real(Corr[j]) << imag(Corr[j]) << endl;
        }
  }
```

```
        fout.close();
}
void main(void){
        /*This section of the program will determine all the values that will go
        into the initial tridagonal matrix*/
        char gaussfile[80], filename[128];
  double *rgain, *igain, *rb, *ib, Currentden;
        double deltaX, deltaZ, deltaX_p, deltaZ_p, ko, tmp, *bbb;
        double sigma, FWHM_p, Dp_p, x_p_sq;
  double *backward_facet, *foward_facet;
        complex *a, *b, *c, *d, *b_init, *E_init, *E_old, *E_new, *Corr, **E_field, **E_field_b;
  complex *a_b, *b_b, *c_b, *d_b, *E_old_b, *E_new_b;
  double *aa, *bb, *cc, *dd, *N, *N_b, aacc, *inten, *inten_f, *inten_b, **N_matrix;
  E_field = cmatrix(0, (NumX-1), 0, NumZ);      // # of rows, # of colums;
  E_field_b = cmatrix(0, (NumX-1), 0, NumZ);    // # of rows, # of colums;
  N_matrix = dmatrix(0, (NumX-1), 0, (NumZ-1));     // # of rows, # of colums;
  inten = dvector(0, (NumX-1));
  bbb = dvector(0,(NumX-1));
  aa = dvector(0,(NumX-1));
        bb = dvector(0,(NumX-1));
        cc = dvector(0,(NumX-1));
        dd = dvector(0,(NumX-1));
        N = dvector(0,(NumX-1));
  N_b = dvector(0,(NumX-1));
        a = cvector(0,(NumX-1));
        b = cvector(0,(NumX-1));
  b_init = cvector(0,(NumX-1));
        c = cvector(0,(NumX-1));
        d = cvector(0,(NumX-1));
  E_init = cvector(0,(NumX-1));
        E_old = cvector(0,(NumX-1));
        E_new = cvector(0,(NumX-1));
  a_b = cvector(0,(NumX-1));
        b_b = cvector(0,(NumX-1));
        c_b = cvector(0,(NumX-1));
        d_b = cvector(0,(NumX-1));
  E_old_b = cvector(0,(NumX-1));
        E_new_b = cvector(0,(NumX-1));
  backward_facet = dvector(0,(NumX-1));
  foward_facet = dvector(0,(NumX-1));

  Corr = cvector(0,(NumZ-1));     // Might have to change the dimension of this

        complex iota(0.0,1.0), ac, Kxl, Kxr, Kxl_b, Kxr_b;
  cout << "iota" << iota << endl;
  complex E_old_minus1, E_old_NumX, E_old_b_minus1, E_old_b_NumX, denum;
        complex *delta, *delta_init;
        delta = cvector(0,(NumX-1));
  delta_init = cvector(0,(NumX-1));
  double *Gamma;
  Gamma = dvector(0,(NumX-1));
```

```
//Output Power stuff
complex *E_new_tmp, *output_field_f, *output_field_b, *E_new_b_tmp;
double convert, output_power_p, output_power, output_power_p_old, perch, hbar_omega,
surface_element;
double perchold;
double *output_intensity, *Energy_density, Energy_den;
double *Energy_density_f, *Energy_density_b, *Carrier_density;
output_field_f = cvector(0,(NumX-1));
        output_field_b = cvector(0,(NumX-1));
        output_intensity = dvector(0,(NumX-1));
E_new_b_tmp = cvector(0,(NumX-1));
E_new_tmp = cvector(0,(NumX-1));
Energy_density = dvector(0, NumZ);
Energy_density_f = dvector(0, NumZ);
Energy_density_b = dvector(0, NumZ);
Carrier_density = dvector(0, NumZ);
inten_f = dvector(0, (NumX-1));
inten_b = dvector(0, (NumX-1));

        long int i, j, k, p, u, s, t;
int size;
k=1;

// **********Addtional parameters to turn waveguide into a laser**************
double kappa_p, alpha_p, df_p, tau_p, *j_p, J, J_p, JtoJ_p, I;
int J_int;
j_p = dvector(0,(NumX-1));
complex Rline_p, *gain, *gain_b;
Rline_p = 1.0 -3*iota;
cout << "Rline\t" << Rline_p << endl;
gain = cvector(0,(NumX-1));
gain_b = cvector(0,(NumX-1));
rgain = dvector(0,(NumX-1));
igain = dvector(0,(NumX-1));
rb = dvector(0,(NumX-1));
ib = dvector(0,(NumX-1));


alpha_p = alpha_m*length_m;
cout << "alpha\t" << alpha_p << endl;
kappa_p = (Again_m*Nzero_m*length_m)/2;
cout << "kappa_p\t" << kappa_p << endl;
tau_p =  (Tau*Clight_m)/(Nave*length_m);
df_p = (Df_m*Nave*length_m)/(Clight_m*width_m*width_m);

//************************** end of additional laser terms ************************


        deltaZ  = length_m/NumZ;    /*Units um*/
cout << "deltaZ:\t" << deltaZ << endl;
        deltaZ_p = deltaZ/length_m;  /*Dimensionless*/
        deltaX  = width_m/NumX;          /*Units um*/
        deltaX_p = deltaX/width_m;       /*Dimensionless*/
```

```
        cout << "deltaZ_p is equal to:\t" << deltaZ_p << endl;
        cout << "deltaX_p is equal to:\t" << deltaX_p << endl;


  //****************** SET UP REFRACTIVE INDEX PROFILE
**************************************
        ko = 2*pi/lambda_m;     //ko in reciprocal nanometers
        denum = 2*Nave;
        for(i=0;i<=NumX-1;i++){   /*This loop sets up the refractive index profile  */
                if(i<=61 || i>=188){    // 1um core; 2.5um cladding regions
                        /*This is -1 times the delta symbol that appeared in the trueblue report
                        since in the waveguide case -delta is equal to Br+1/2,s   */
                        delta_init[i] = (iota*ko*length_m*(pow(Nclad,2)- pow(Nave,2)))/denum;
    Gamma[i] = 0.02;
    }
                else if ( (i<=62 && i >=118) || (i>=133 && i<=187) ){
                        delta_init[i] = (iota*ko*length_m*(pow(Nside,2)- pow(Nave,2)))/denum;
    Gamma[i] = 0.0159;
    }
    /*else if ( (i<=91 && i >=90) || (i>=107 && i<=108) ){
                        delta[i] = (iota*ko*length_m*(pow(Ndep,2)- pow(Nave,2)))/denum;
    Gamma[i] = 0.02;
    }    */
    else{
      delta_init[i] = (iota*ko*length_m*(pow(Ncore,2)- pow(Nave,2)))/denum;
      Gamma[i] = 0.02;
    }
        }
        cout << "delta[150] is:\t" << delta[150] << endl;

//*************************************************************************************
******

  //Converts Intensity from dimensionless units to W/m^2
  hbar_omega = hplanck*(Clight_m/lambda_m);
  cout << hbar_omega << endl;
  convert = (Clight_m*hbar_omega)/(Again_m*Nave*length_m);
  cout << "convert to non-d to W/m^2\t" << convert << endl;

   //*****************************Set up Stripe
Geometery*****************************************
  J = 25.50e6;
  Currentden = J/10000;
  cout << Currentden;
  JtoJ_p = (Nave*length_m)/(Clight_m*Nzero*d_m*Qe);
  J_p = J*JtoJ_p;
  //J_p =(J*Nave*length_m)/(Clight_m*Nzero*d_m*Qe);
  cout << "J\t" << J << endl;
  // setup stripe geometery
  for(i=0;i<=NumX-1;i++){   /*This loop sets up the refractive index profile  */
        if(i<= 116 || i>= 134)
     j_p[i] = 0.0;
   else
                        j_p[i] = J_p;
  }
```

```
//*************************************************************************************
******


  /*******************************Diffraction term*****************************/
        Dp_p = length_m/(2*ko*Nave*pow(width_m,2));

        cout << "Dp_p is:\t" << Dp_p << endl;


        //***************************** a's and c's foward, backward & diffusion
**********************
  aacc = df_p/(deltaX_p*deltaX_p);
        ac = (-1*Dp_p*deltaZ_p*iota)/(pow(deltaX_p,2));

        for(i=0;i<=NumX-1;i++){
        c[i] = ac;
                a[i] = ac;
    c_b[i] = ac;
    a_b[i] = ac;
                cc[i] = aacc;
                aa[i] = aacc;
        }
        cout << "a & c compenents are:\t" << ac << endl;

//*************************************************************************************
*******


  for(i=0;i<=NumX-1;i++){
        // forward
        b_init[i] =  2 - (2*ac) - (deltaZ_p*delta[i]);   /* forward c[0] equals -pA*/
  }


        /*Make initial field*/
        /*The initial field is a gaussian*/
        cout << "File Name for the initial field:\t";
        cin >> gaussfile;
        ofstream fout(gaussfile);
        FWHM_p = GaussFWHM_m/width_m;
        sigma = log(2)/pow((FWHM_p/2),2);
        //cout << "sigma:\t" << sigma << endl;
        for(i=0;i<=NumX-1;i++){
                x_p_sq = pow(deltaX_p*abs(i-((NumX/2)+4)),2);     //offset from center to ensure
asymmetery
                E_init[i] = Ezero*exp(-sigma*x_p_sq) +  iota*0.0;
        fout << abs(E_init[i]) << "\n";  // Outputs the initial field to file
    //Corr[0] = Corr[0] + E_init[i]*E_init[i]*deltaX_p;    // correlation function integration
        }
        fout.close();

        /*for(i=0;i<=NumX-1;i++){
                E_old[i] = E_init[i];  //set init field equal to E_old forward
```

```
    E_old_b[i] = E_init[i];  //set init field equal to E_old backward
    E_field[i][0] = E_init[i];
    E_field_b[i][NumZ] = E_init[i];
          }  */

  for(i=0;i<=NumX;i++){
          N[i] = 0.0;
  }


//*************************************************************************************
******
  //*****************************      START OF BEAM PROPAGATION
**********************************
//*************************************************************************************
********
  for(J_int=0;J_int<=100;J_int++){
                cout << "J_int = \t" << J_int << endl;
          for(j=1;j<=(NumZ*100);j++){

          if(j==1) k = 1;


          /*if(j<NumZ){
                  for(i=0;i<=NumX-1;i++){
                                  Corr[j] = Corr[j] + E_init[i]*E_new[i]*deltaX_p;  // Correlation
function integration
          }
          }  */

       if(j==1){
         for(i=0;i<=NumX-1;i++){
                  delta[i] = delta_init[i];
         }
       }
          /*else if(j==NumZ+1){
                  for(i=0;i<=NumX-1;i++){
                  delta[i] = (0.0,0.0);
          }
          } */


       if(j==1){
          for(i=0;i<=NumX-1;i++){
                  E_old[i] = E_init[i];
          E_old_b[i] = E_init[i];
           E_field[i][0] = E_init[i];
                          E_field_b[i][NumZ] = E_init[i];
          }
       }else{
          for(i=0;i<=NumX-1;i++){
                  E_old[i] = E_new[i];
          E_old_b[i] = E_new_b[i];
          }
       }
```

```
t = (j-1) - (NumZ*(k-1));        // t Will keep track of the position of the wavefront

if(j<=NumZ){
        for(i=0;i<=(NumX-1);i++){
                gain[i]  = (0.0,0.0);
 gain_b[i] = (0.0,0.0);
 }
 }else{
        for(i=0;i<=(NumX-1);i++){
 //if(i>= && i<=137){
 N[i] = N_matrix[i][t];
                gain[i]  = ((kappa_p*Gamma[i])*((Rline_p*N[i])-1.0) - alpha_p); //(
(kappa_p*Gamma[i])*((Rline_p*N[i])-1)) - alpha_p;
 N_b[i] = N_matrix[i][NumZ-t];
                gain_b[i]  = ((kappa_p*Gamma[i])*((Rline_p*N_b[i])-1.0) - alpha_p); //(
(kappa_p*Gamma[i])*((Rline_p*N[i])-1)) - alpha_p;
 rgain[i] = real(gain[i]);
 igain[i] = imag(gain[i]);
 /*}       else{
 gain[i]  = (0.0,0.0);
                gain_b[i] = (0.0,0.0);
                                                }*/
 }
 }



 if(j==1){
 for(i=0;i<=NumX-1;i++){
 b[i] = b_init[i];
 b_b[i] = b_init[i];
 }
 }else{
        for(i=0;i<=NumX-1;i++){
        // forward
                                b[i] =  2 - (2*ac) - (deltaZ_p*(gain[i] + delta[i]));    // forward
c[0] equals -pA
 // backward
        b_b[i] = 2 - (2*ac) - (deltaZ_p*(gain_b[i] + delta[i]));    //backward propagating
 }
 }



                for(i=1;i<=NumX-2;i++){    // calculates from d[1] to d[NumX-2]
 // forward
        d[i] =  ( 2 + (2*ac) + (deltaZ_p*(gain[i] + delta[i])) )*E_old[i] + ((-1)*ac*(E_old[i-
1]+E_old[i+1]));
 //backward
 d_b[i] =  ( 2 + (2*ac) + (deltaZ_p*(gain_b[i] + delta[i]))  )*E_old_b[i] + ((-1)*ac*(E_old_b[i-
1]+E_old_b[i+1]));
                }
```

```
                    /*The value for Kx used for the boundary conditions
                    this value will have to be updated each time the beam
                    is propagated by one step*/

                    Kxr = log(E_old[NumX-1]/E_old[NumX-2])/(deltaX_p*iota);
        if(real(Kxr) <= 0.0){
                Kxr = 0.0 + imag(Kxr)*iota;
        }
        Kxr_b = log(E_old_b[NumX-1]/E_old_b[NumX-2])/(deltaX_p*iota);          //(-
1)*iota*log(E_old_b[NumX-1]/E_old_b[NumX-2])/deltaX_p;
        if(real(Kxr_b) <= 0.0){
                Kxr_b = 0.0 + imag(Kxr_b)*iota;
        }
                    Kxl = log(E_old[0]/E_old[1])/(deltaX_p*iota);
        if(real(Kxl) <= 0.0){
                Kxl = 0.0 + imag(Kxl)*iota;
        }
        Kxl_b = log(E_old_b[0]/E_old_b[1])/(deltaX_p*iota);                    //
        (-1)*iota*log(E_old_b[0]/E_old_b[1])/deltaX_p;
        if(real(Kxl_b) <= 0.0){
                Kxl_b = 0.0 + imag(Kxl_b)*iota;
        }
                    /*Boundary Conditions b[0] and b[NumX-1]*/
        //b[0] = b[1];
        //cout << "b[0] =" << b[0] << endl;
        //b[NumX-1] = b[NumX-2];
                    b[0] =  b[0] + (ac*exp(iota*Kxl*deltaX_p));
        b_b[0] =  b_b[0] + (ac*exp(iota*Kxl_b*deltaX_p));

                    b[NumX-1] = b[NumX-1] + (c[0]*exp(iota*Kxr*deltaX_p));
        b_b[NumX-1] = b_b[NumX-1] + (c_b[0]*exp(iota*Kxr_b*deltaX_p));
        //cout << "b[NumX-1] is\t" << b[NumX-1] << endl;

        //Boundary Conditions d[0] and d[NumX-1]
                    E_old_minus1 = E_old[0]*exp(iota*Kxl*deltaX_p);
        E_old_b_minus1 = E_old_b[0]*exp(iota*Kxl_b*deltaX_p);
                    //cout << "E_old[minus1] is\t" << E_old_minus1 << endl;


                    d[0] =  ( 2 + (2*ac) + (deltaZ_p*(gain[0] + delta[0])) )*E_old[0] + ((-
1)*ac*(E_old[1]+E_old_minus1));
        d_b[0] =  ( 2 + (2*ac) + (deltaZ_p*(gain_b[0] + delta[0]))  )*E_old_b[0] + ((-
1)*ac*(E_old_b[1]+E_old_b_minus1)); //?????????? a[0] vs c[0]
                    //cout << "d[0] is\t" << d[0] << endl;

                    E_old_NumX = E_old[NumX-1]*exp(iota*Kxr*deltaX_p);
        E_old_b_NumX = E_old_b[NumX-1]*exp(iota*Kxr_b*deltaX_p);
                    d[NumX-1] =  ( 2 + (2*ac) + (deltaZ_p*(gain[NumX-1] + delta[NumX-1]))
)*E_old[NumX-1] + ((-1)*ac*(E_old[NumX-2]+E_old_NumX));
        d_b[NumX-1] =  ( 2 + (2*ac) + (deltaZ_p*(gain_b[NumX-1] + delta[NumX-1]))
)*E_old_b[NumX-1] + ((-1)*ac*(E_old_b[NumX-2]+E_old_b_NumX));
```

```
                ctridag( a, b, c, d, E_new);
    ctridag(a_b, b_b, c_b, d_b, E_new_b);


//s = t+1;
s = j - (NumZ*(k-1));
    //cout << "s is equal to\t" << s << endl;
    u = (NumZ*k) - j;
    //cout << "u is equal to\t" << u << endl;


    for(i=0;i<=NumX-1;i++){
                E_field[i][s] = E_new[i];
                E_field_b[i][u] = E_new_b[i];
    }

    if( (j/NumZ) == k){
                cout << k << endl;
                    k++;

  for(i=0;i<=NumX-1;i++){
    foward_facet[i] =  norm(E_field[i][3000]) + norm(E_field_b[i][3000]);
    backward_facet[i] =  norm(E_field[i][0]) + norm(E_field_b[i][0]);
  }

  if(k>=15 && fabs(perch)<=2.0 && fabs(perchold)<=2.0){
    size = 2998;
    file("Ed_f", Currentden, filename);
    savetofile(size, filename, Energy_density_f);
    file("Ed_b", Currentden, filename);
    savetofile(size, filename, Energy_density_b);
    file("Ed", Currentden, filename);
    savetofile(size, filename, Energy_density);
    file("CarrZ", Currentden, filename);
    savetofile(size, filename, Carrier_density);
                size = 249;

    file("foward_facet", Currentden, filename);
                savetofile(size, filename, foward_facet);
    file("backward_facet", Currentden, filename);
                savetofile(size, filename, backward_facet);

                file("E_field", Currentden, filename);
                savetofile(size, filename, E_new);
                file("E_field_b", Currentden, filename);
                savetofile(size, filename, E_new_b);
    file("gain", Currentden, filename);
    savetofile(size, filename, rgain);
                file("index", Currentden, filename);
                savetofile(size, filename, igain);
    file("carr", Currentden, filename);
                savetofile(size, filename, N);
    ofstream LIcurve("/john/data/ig/fred_tb/LIcurve.dat" , ios::app);
```

```
        LIcurve << J << "\t" << output_power << "\t" << perch << "\t" << I << "\t" << output_power <<
"\t" << perch << "\n";
        LIcurve.close();
        break;
                }

                for(p=0;p<=(NumZ);p++){
                        for(i=0;i<=NumX-1;i++){
                // The next line is the intensity at p*deltaX from front facet
          inten_f[i] = norm(E_field[i][p]);
          inten_b[i] = norm(E_field_b[i][p]);
                inten[i] =  norm(E_field[i][p]) + norm(E_field_b[i][p]);

                if(k>=59 && (p<=(NumZ-1))){
                        if(i==0){
                        Energy_density_f[p] = 0.0;
                Energy_density_b[p] = 0.0;
                Energy_density[p] = 0.0;
                }
                Energy_density_f[p] = Energy_density_f[p] + (inten_f[i]*deltaX_p);
                Energy_density_b[p] = Energy_density_b[p] + (inten_b[i]*deltaX_p);
                        Energy_density[p] = Energy_density[p] + (inten[i]*deltaX_p);
                }

                /*if( k>=60 && i==(NumX-1) && p==NumZ && perch<=0.001){
                        size = 1998;
                file("Ed_f", Currentden, filename);
                savetofile(size, filename, Energy_density_f);
                file("Ed_b", Currentden, filename);
                savetofile(size, filename, Energy_density_b);
                file("Ed", Currentden, filename);
                savetofile(size, filename, Energy_density);
                }   */


                                bb[i] =  (2*aacc) + (1/tau_p) + (Gamma[i]*inten[i]);    // main diagonal

                bb[i] = -bb[i];



                if(i==0){
                        tmp = ( (1/tau_p) + Gamma[0]*inten[0])/df_p;
                                tmp = bb[0] + cc[0]*exp(-1*sqrt(tmp)*deltaX_p);
                        bb[0] = tmp;
                }

                if(i == NumX-1){
                        tmp = ( (1/tau_p) + Gamma[NumX-1]*inten[NumX-1])/df_p;
                                                tmp =  bb[NumX-1] + cc[0]*exp(-
1*sqrt(tmp)*deltaX_p);
                        bb[NumX-1] = tmp;
                }
                        dd[i] = -1*(j_p[i] + Gamma[i]*inten[i]);
                }
```

```
                dtridag( aa, bb, cc, dd, N);
                for(i=0;i<=NumX-1;i++){
                                                N_matrix[i][p] = N[i];


                if(k>=59 && (p<=(NumZ-1))){
                        if(i==0){
                Carrier_density[p] = 0.0;
                }
                        Carrier_density[p] = Carrier_density[p] + (N[i]);
                                                }
                        }
        }    //End of p loop

        //cfree_matrix(E_field, 0, (NumX-1), 0, NumZ);
        //cfree_matrix(E_field_b, 0, (NumX-1), 0, NumZ);
        //E_field = cmatrix(0, (NumX-1), 0, NumZ);      // # of rows, # of colums;
                        //E_field_b = cmatrix(0, (NumX-1), 0, NumZ);    // # of rows, # of colums;

        //if(k==99) savetofilex("E_new foward Before the facet is:", E_new);


        for(i=0;i<=NumX-1;i++){
                E_new_tmp[i] = -1*sqrt(reflectr)*E_new_b[i];
        E_new_b_tmp[i] = -1*sqrt(reflectr)*E_new[i];

        //Output power

        if(i==0){
                output_power_p = 0.0;
          surface_element = deltaX*(d_m/Gamma[125]);
        }
        output_field_f[i] = E_new[i] + E_new_b_tmp[i];   //Might need to be plus in this line and the
next;
        output_field_b[i] = E_new_b[i] + E_new_tmp[i];
        output_intensity[i]  =  norm(output_field_f[i]) + norm(output_field_b[i]);
        output_power_p = output_power_p + output_intensity[i]*surface_element;        //Non-
dimensional power
        if(i==(NumX-1)){
                output_power = output_power_p*convert;   // Watts
          I = J*length_m*8e-6*1000;   // Current in mA
        }

        E_new[i] = E_new_tmp[i];
        E_new_b[i] = E_new_b_tmp[i];
        E_field[i][0] = E_new[i];
        E_field_b[i][NumZ] = E_new_b[i];
        }

        if(k>=3){
        if(k >= 4) perchold = perch;
                perch = ((output_power_p - output_power_p_old)/(output_power_p_old))*100;
        cout << "percentage change\t" <<  perch << endl;
        }
```

```
        output_power_p_old = output_power_p;

        } // End of IF STATMENT *****Mirror Boundary Conditions******

        } // End of j FOR loop;

        //savetofilez("The Corrrelation function:", Corr);

        J = J + 0.50e6;    // Current is increased
    cout << J << endl;
    J_p = J*JtoJ_p;
    Currentden = J/10000;
    for(i=0;i<=NumX-1;i++){  /*This loop sets up the refractive index profile  */
                if(i<= 61 || i>= 187){
        j_p[i] = 0.0;
      }
      else if ((i >=62 && i <=118) || (i >=132 && i <=188)) {
        j_p[i] = J_p/2;
      }
      else {
        j_p[i] = J_p;
      }
        }
  }
cin >> filename;

}  // End of main

//*****************************************************************************

complex *cvector(long nl, long nh)
{
        complex *v;
        v=(complex *)malloc((size_t) ((nh-nl+1+NR_END)*sizeof(complex)));
        if (!v) nrerror ("allocation failure in vector()");
        return v-nl+NR_END;
}

//*****************************************************************************


double *dvector(long nl, long nh)
{
        double *v;
        v=(double *)malloc((size_t) ((nh-nl+1+NR_END)*sizeof(double)));
        if (!v) nrerror ("allocation failure in vector()");
        return v-nl+NR_END;
}


//*****************************************************************************
```

```
void nrerror(char error_text[])
{
        fprintf(stderr,"Numerical Recipes run time error\n");
        fprintf(stderr, "%s\n",error_text);
        fprintf(stderr,"now exiting to system\n");
        exit(1);
}

//*************************************************************************

void ctridag(complex a[NumX], complex b[NumX], complex c[NumX], complex d[NumX], complex
E_new[NumX])
{

        /* the function tridag is used to solve tridiagonal systems of linear equations */
        /* In this case E_new[0:n] is the unknown vector and a[], b[], c[], and d[] are the */
        /* input vectors
        /* in this routine a0 and cn are not used */


complex bet, *gam;
long int j;

gam = cvector(0,(NumX-1));

if (b[0] == 0) nrerror("Error 1 in tridag");

        E_new[0]=d[0]/(bet=b[0]);
        //printf("r[0] = %f\n; bet = %f\n; u[0] = %f\n;", r[0], bet, u[0]);
        for (j=1; j<=NumX-1; j++) {
                gam[j]=c[j-1]/bet;
                bet = b[j]-a[j]*gam[j];
                 if (bet == 0.0) nrerror("Error 2 in tridag");
                E_new[j]=(d[j]-a[j]*E_new[j-1])/bet;
        }

        for (j=(NumX-2); j>=0; j--){
                E_new[j] -= gam[j+1]*E_new[j+1];
        }
  cfree_vector(gam,0,(NumX-1));
}  /*End of Tridag*/

//*************************************************************************************
********


void dtridag(double aa[NumX], double bb[NumX], double cc[NumX], double dd[NumX], double
N[NumX])
{

        /* the function tridag is used to solve tridiagonal systems of linear equations */
        /* In this case E_new[0:NumX-1] is the unknown vector and a[], b[], c[], and d[] are the */
        /* input vectors
        /* in this routine a0 and cn are not used */
```

```
double bet, *gam;
long int j;

gam = dvector(0,(NumX-1));

if (bb[0] == 0) nrerror("Error 1 in tridag");

        N[0]=dd[0]/(bet=bb[0]);

        for (j=1; j<=NumX-1; j++) {
                gam[j]=cc[j-1]/bet;
                bet = bb[j]-aa[j]*gam[j];
   if (bet == 0.0) nrerror("Error 2 in tridag");
                N[j]=(dd[j]-aa[j]*N[j-1])/bet;
        }

        for (j=(NumX-2); j>=0; j--){
                N[j] -= gam[j+1]*N[j+1];
        }
  dfree_vector(gam,0,(NumX-1));
} /*End of dTridag*/


//*****************************************************************************

complex **cmatrix(long nrl, long nrh, long ncl, long nch)
// allocates space for a complex
{
        long i, nrow=nrh-nrl+1, ncol=nch-ncl+1;
        complex **m;

        // allocates pointers to rows
        m=(complex **) malloc((size_t)((nrow+NR_END)*sizeof(complex*)));
  if (!m) nrerror("allocation faiure 1 in matrix()");
  m += NR_END;
  m -= nrl;

  // allocate rows and set pointers to them
  m[nrl]=(complex *) malloc((size_t)((nrow*ncol+NR_END)*sizeof(complex)));
  if (!m[nrl]) nrerror("allocation faiure 2 in matrix()");
  m[nrl] += NR_END;
  m[nrl] -= ncl;

  for(i=nrl+1;i<=nrh;i++) m[i]=m[i-1]+ncol;

  // return pointers to array of pointers to rows
  return m;

} // end of cmatrix

//*****************************************************************************

double **dmatrix(long nrl, long nrh, long ncl, long nch)
```

```
// allocates space for a complex
{

        long i, nrow=nrh-nrl+1, ncol=nch-ncl+1;
        double **m;

        // allocates pointers to rows
        m=(double **) malloc((size_t)((nrow+NR_END)*sizeof(double*)));
  if (!m) nrerror("allocation faiure 1 in matrix()");
  m += NR_END;
  m -= nrl;

  // allocate rows and set pointers to them
  m[nrl]=(double *) malloc((size_t)((nrow*ncol+NR_END)*sizeof(double)));
  if (!m[nrl]) nrerror("allocation faiure 2 in matrix()");
  m[nrl] += NR_END;
  m[nrl] -= ncl;

  for(i=nrl+1;i<=nrh;i++) m[i]=m[i-1]+ncol;

  // return pointers to array of pointers to rows
  return m;

} // end of dmatrix

//*****************************************************************************


void dfree_vector(double *v, long nl, long nh)
// frees up a double vector
{
        free ((FREE_ARG) (v+nl-NR_END));
}

//*****************************************************************************
*************

void cfree_vector(complex *v, long nl, long nh)
// frees up a double vector
{
        free ((FREE_ARG) (v+nl-NR_END));
}

//*****************************************************************************
***************

void cfree_matrix(complex **m, long nrl, long nrh, long ncl, long nch)

{
        free((FREE_ARG) (m[nrl]+ncl-NR_END));
  free((FREE_ARG) (m+nrl-NR_END));
}

//*****************************************************************************
*********************
```

```
void dfree_matrix(double **m, long nrl, long nrh, long ncl, long nch)

{
        free((FREE_ARG) (m[nrl]+ncl-NR_END));
  free((FREE_ARG) (m+nrl-NR_END));
}

//*************************************************************************************
*****************

void file(char out_text[], double Currentden, char filename[128])
{

  char stripe[128] = "/john/data/ig/full_stripe_R2N16um/";
        char filetype[128] = ".dat";

  char current[128] = "";
        if(Currentden < 1000.0) sprintf(current, "%3.0f", Currentden);
  if(Currentden >= 1000.0) sprintf(current, "%4.0f", Currentden);
  strcat(stripe, out_text);


  strcat(stripe, current);
  strcat(stripe, filetype);
  strcpy(filename, stripe);
  //cout << filename << endl;
}
```